Bulk Time-Dependent Properties of Fault Damage Zones

By

Mayukh Talukdar

A dissertation submitted in partial fulfillment of
the requirements for the degree of

Doctor of Philosophy
(Geological Engineering)

at the

UNIVERSITY OF WISCONSIN-MADISON

2022

Date of final oral examination: 08/25/2022

The dissertation is approved by the following members of the Final Oral Committee:
Hiroki Sone, Associate Professor, Geological Engineering (Advisor)
Laurel Goodwin, Professor, Geoscience
Lucas Zoet, Associate Professor, Geoscience
Shiva Rudraraju, Assistant Professor, Mechanical Engineering
Li-Wei Kuo, Professor, Earth Sciences, National Central University

ABSTRACT

This thesis aims to characterize the bulk time-dependent properties of fault damage zone rocks with a combination of field, experimental and numerical data.

Damage zones are ubiquitous features of fault zones. They surround the primarily slip plane, and, in many cases, are characterized by the presence of pervasive fractures and clay minerals. Where fractures and clay minerals are present, they promote stable sliding along crack surfaces and grain boundaries, which allow damage zones to deform by bulk creep deformation. Such mesoscopic ductile deformation of damage zones facilitates fault healing following earthquakes because ductile deformation mechanisms in the shallow crust (e.g., compaction creep, pressure solution) typically involve volumetric contraction. Our data suggest that a substantial magnitude of strain takes place during the healing process, which is expected to relax fault shear stress during interseismic periods. To study this phenomenon, our research focused on calculating the stress magnitude in the damage zone in comparison to the host rock, exploring evidence of time-dependent deformation of the damage zones, and characterizing the time-dependent deformation and seismic velocity change of damage zones in comparison to intact host rock.

Forces in the Earth's crust defines the stresses acting on faults which drive earthquakes. Tracking how stress accumulates due to plate motion and is released due to fault slip have been central topics in the study of earthquake mechanics and associated seismic hazards. Previous analyses of data collected from the Taiwan Chelungpu-fault Drilling Project (TCDP), following the 1999 Chi-Chi earthquake resulted in inconsistent estimates of post-earthquake stress. This study included reviews of previous measurements, laboratory experiments, and analyses of borehole data to reconsider the stress state after the Chi-Chi earthquake. We show that the stress state varied along the TCDP borehole due to lithologic and fault-related changes in mechanical properties, which explains why past studies indicated significant variability. We also estimated pre-earthquake stress by calculating the stress change caused by the Chi-Chi earthquake and subtracting it from the post-earthquake stress. Our pre-earthquake stress estimate suggests that the stress before the Chi-Chi earthquake was low in magnitude compared to the frictional strength of shallow crustal rocks. Comparing the estimated pre and post-earthquake stress magnitudes of the damage zone and host rock shows the maximum principal stress is lower and minimum principal stress is higher at the depth interval between 1050-1250 m, which corresponds to the damage zones of the Chelungpu fault. An elastic plane strain model with fault-parallel layers of varying elastic properties shows that stress rotation due to reduced elastic stiffness cannot explain the low differential stress magnitude in damage zones. Since fault zone material is not significantly weaker than the host rock, this suggests fault shear stress was relaxed within the damage zone due to time-dependent deformation. Borehole log data also show more time-dependent ductile deformation in old damage zones compared to younger ones.

We also characterize time-dependent ductile deformation of TCDP rocks fractured to various damage densities. Various damage densities (termed D0-D4) were created by subjecting

the samples to strain rates analogous to those experienced by natural damage zones during super-shear to sub-shear ruptures. The impacted samples were then loaded to in-situ stress conditions, after which stress was held constant to measure creep deformation and velocity recovery. Both creep strain and velocity recovery during the hold stage increased with damage (i.e., from D0-D4), suggesting increasing rate of porosity reduction and contact stiffening in the damage zone compared to intact rock. Higher fracture volume closure in highly damaged specimens was also evident in micro structural observations from Scanning Electron Microscopy (SEM) and Micro-Computed tomography (MCT). Comparison of MCT images obtained before and after the creep experiments highlight an increase in contact area of fracture surfaces due to creep, aiding passage of ultrasonic waves through the sample and thereby increasing ultrasonic velocity. The temporal increase in velocity during creep shows a linear relationship with logarithm of time, consistent with a logarithmic increase in seismic velocity following large earthquakes. Such log-time extrapolation of experimental data to 6 years is analogous to the field-scale velocity recovery in the Chelungpu fault area following the 1999 event. We also modeled the volumetric strain of the specimens using a Perzyna viscoplasticity law that employs the Modified Cam Clay model as a yield criterion. The Perzyna MCC model characterizes the higher pore volume loss in damaged specimens. Fitting the model to experimental data, we suggest that an intact sample has lower viscosity and rate of viscosity change with time than a damaged sample because more frictional forces need to be overcome in an intact sample for the material to deform. Moreover, a comparison of velocity and porosity data reveals creep induced strengthening of the junctions of fracture interfaces, which increases material stiffness at a faster rate than pore compaction.

ACKNOWLEDGEMENTS

I appreciate my PhD advisor Hiroki Sone for his guidance and support in this journey under all circumstances. What I appreciate the most about him is his ability to critically analyze a problem and brainstorm on the go. My conversations with Hiroki have been very thought-provoking and invigorated me to pursue science as a career. Apart from innumerous brainstorming sessions, I am indebted to him for his efforts in grooming me into a meticulous experimentalist. During the initial days of my PhD, I tended to consider some of the details in experimentation redundant. On the way, as I started becoming more detail oriented, I found the quality of my results improve. I love to do experiments now (notwithstanding the delays and obstacles) after working with Hiroki. It has been a fulfilling process!

My committee members Laurel Goodwin, Shiva Rudraraju, Lucas Zoet and Li-wei Kuo have made their own distinctive contributions throughout my journey. Laurel played an integral part in building my foundation in Earthquake and Fault mechanics. She was quick in clarifying my questions, on reviewing my writing and in guiding me towards answers of complex problems by dropping hints during our conversations. Shiva taught me finite element and finite difference from scratch till I was able to write my own 2D and 3D codes in MATLAB. The skill sets I

learnt from Shiva benefited me immensely when I approached modeling as part of this thesis. Shiva was also a continuous support in terms of career advice and mentoring. The questions Luke posed on the physics behind coupled processes during my preliminary presentation were key to the discussion sections of my thesis chapters. Talking to Luke, I gained perspective on the merits and limitations of my research, which encouraged me to reach new boundaries. Li-Wei's efforts to provide me with essential log data, cores and site-specific information are highly appreciated. Li-Wei's flexibility and support during our trips to Taiwan made my stay memorable. If we were not hit by the pandemic, I would have enjoyed visiting Li-Wei every year to gorge on some delicious dumplings and mango shaved ice with him.

Besides conducting research, working as a founding member of Justice Equity Diversity and Inclusivity committee (JEDI) in the Department of Civil and Environmental Engineering has been a daunting task in the last few years. It is during this process that I have realized how crucial these aspects are in a mentee-mentor relationship and the entire academic community. It was a pleasure to be in the organizing committee of undergraduate and graduate listening sessions with Sarah Dance, Amanda Thuss and Matthew Ginder-Vogel. I am indebted to other JEDI committee members like Aaron Alexander, Keerthana Sreenivasan, Andrea Hicks, Katrina Rabeler and Dante Fratta for doing major work in involvement of graduate students in the faculty recruitment process, fostering JEDI-related discussions in courses and research groups, raising the issue of JEDI training for faculty and staff (including cases of microaggression), and encouraging the habit of adding pronouns after names. Working with them has cultivated in me a deep sense of responsibility for underrepresented groups and infused me with the commitment to work towards actionable objectives in the future.

My support systems during this journey have kept me sane and helped maintain a healthy work life. I would not have reached the end of this journey without Grace, Abhilash, Amber, Clara and Maciej. I strongly believe in support systems, and I wish there was a better way to appreciate them, but I am falling short of words.

I would like to thank Charlotte, Kate, Zirou and Kevin for their help in the lab. I consider myself fortunate to have socio-cultural exchanges with my office colleagues: Ben, Bharat, Connor, Elliot, Eril, Esra, Larue, Laurel, Luke, Mike, Mohammed, Morgan, Samantha, Siyu, Susan and Russ. I feel bad for Debamanyu, Talha, Ammar and Manisha for the being argumentative with them, but also appreciate them for arguing back with equal enthusiasm.

My mother Maushumi and sister Mugdha was there through thick and thin. The whole purpose of staying away from home was to match my mother's cooking skills, but my sister keeps reminding me that I have failed miserably. But thank you, Maa! I am so grateful to you!

My father had a hankering to pursue science but never got his opportunity. I wish he was here to watch me present my work. Nonetheless, I know he will be smiling down from a bright Madison summer sky.

TABLE OF CONTENTS

LIST OF FIGURES

CHAPTER 1

Introduction

1.1 Motivation

Fault slip producing earthquakes creates distributed inelastic deformation in the earth's crust, forming regions of localized fractures or pervasively fractured rocks. The fractured rock surrounding the slip plane is called the damage zone. Compared to an intact host rock, fractured damage zone rocks are less stiff, generally more permeable and have reduced seismic velocity, thereby affecting the mechanical, hydraulic and seismological properties of fault zones (Chester et al., 1993; Faulkner and Rutter, 2001, 2003). Permeability measurements and seismological observations also show a progressive decrease in permeability and increase in seismic velocity following an earthquake (Kitagawa et al., 2007; Kitagawa and Kano, 2016; Pei et al., 2019;

Vidale and Li, 2003; Xue et al., 2013). These progressive changes in mechanical behavior could be attributed to time-dependent compaction of damaged rocks (Fialko, 2006), which is enhanced in damage zones due to larger fractured volume compared to intact rock. Moreover, high crack density and, where present, an abundance of clay minerals in damage zones can promote sliding along cracks and grain boundaries to accommodate time-dependent deformation. Such temporal and spatial variations in deformation of damaged rocks can modify the stress state of the bulk rock mass and generate stress anomalies.

If a damage zone deforms by time-dependent deformation after earthquakes and during the interseismic period, it plays a key role in shear stress relaxation in the fault zone. We expect an interplay between stress relaxation due to time-dependent deformation of the damage zone and shear stress accumulation on the fault plane in response to tectonic loading. Studying this interplay is important to better understand how shear stress evolves during the seismic cycle. Knowledge of shear stress evolution over time on a fault plane is key to hazard and risk assessment; however, most fault simulation models consider an elastic time-independent rheology for the damage zones. This study suggests the need to consider a time-dependent damage zone rheology in fault simulation models to better understand how shear stress magnitudes evolve during the seismic cycle.

1.2 Societal Implications

Mechanical properties of fault damage zone rocks and resulting variability in stress can contribute to variability in the recurrence time of earthquakes, earthquake magnitudes, and power-law behavior of earthquake magnitude-frequency distributions. For example, Kaneko et al. (2011) showed that the presence of a fractured damage zone reduces the nucleation size of

earthquakes and amplifies dynamic slip rate during earthquake events. Slip rate dynamics of earthquake sequences in a fault zone with a wide and mature damage zone show that reflection of seismic waves from the boundary between low velocity fault damage zone and high velocity country rock leads to variability in earthquake location and size (Thakur et al. 2020). This dynamic effect on rupture nucleation and size evolves during the seismic cycle as the damage zone heals during post-seismic and inter-seismic periods. These studies suggest that characterizing the rheology of damage zones is imperative.

Understanding time-dependent deformation of fractured rocks has other implications. Mesoscopically ductile deformation of fractured rocks may impact wells drilled in highly fractured areas of the crust. Field studies by Hennings et al. (2012) suggested wells drilled in fractured zones are more productive in regions of high fracture density and in regions where fractures are critically oriented for slip to occur. Experimental measurement of permeability in damage-zone rocks has shown permeability several orders of magnitude higher than intact rocks (Lockner et al., 2000). While these studies suggest that fractures enhance permeability, progressive compaction of the pore volume and sliding along cracks in a fractured rock may reduce permeability at a higher rate than permeability reduction in intact rocks. Therefore, study of the time-dependent mechanical behavior of fractured rocks is critical to understanding long-term well performance. Studying the long-term ductile properties of damaged rocks is also important to ensure the long-term safety and stability of underground storage caverns in fractured rocks. Similarly, the mechanical properties of fractured zones are essential parameters to understand mining design and roadway support. Current reservoir simulation models require bulk hydraulic properties of fractured systems, which is one of the greatest uncertainties in these models. There are limited in-situ data regarding the bulk properties of damage zones, therefore

there is a need to constrain them experimentally. To address these issues, this study characterizes stress in damage zones and measures the bulk elastic and time-dependent properties of damaged materials. This thesis uses the words damaged, fractured and cracked interchangeably.

1.3 Objective

This research has focused on characterizing the bulk properties of fault damage zones by combining field, experimental and numerical studies. The aim is to understand:

a. What is the stress state in a damage zone? And what are the factors affecting the stress state in a damage zone?
b. How does the stress state in the damage zone compare to the intact rock mass?
c. What are possible evidence of time-dependent deformation of damage zone rocks?
d. What is the magnitude of time-dependent deformation of damage zone rocks? What is their constitutive behavior?
e. By what mechanisms does time-dependent deformation of damaged rocks occur?
f. Are lab experiments on analogue damage-zone materials scalable to natural damage zones?

This work represents the first attempt to utilize a variety of data sets to provide insights into bulk time-dependent properties of damage zones.

1.4 Thesis Outline

We studied the bulk time-dependent properties of Chelungpu fault damage zones using log data and cores acquired from the Taiwan Chelungpu Fault Drilling Project (TCDP). TCDP drilled two boreholes five years after the 1999 Mw 7.7 Chi-Chi earthquake to study the

mechanics of faulting in the Chelungpu fault system. TCDP is a suitable location to study time-dependent deformation of damage zones because the vertical boreholes encountered three large reverse faults at different stages in their seismic cycles as well as their damage zones. We chose TCDP for this study not only because Chi-Chi earthquake is not only one of the most extensively studied earthquakes, but also because high-quality geophysical data along with 90% core recovery provide a rich data set.

This thesis has four chapters:

1. *Measuring stress magnitudes*: Knowledge of stress magnitudes is important to study how fault shear stress increases and is released throughout the seismic cycle via coseismic fault slip as well as distributed deformation in the damage zone during the interseismic period. In the first chapter, we constrain the principal stress magnitude before and after the Chi-Chi earthquake. Our objective is to obtain a near continuous profile of stress magnitudes, acknowledging lithologic and fault-related variations along the borehole. In this chapter, we aim to explain the variability in the state of stress along TCDP reported in previous papers.

2. *Evidence of time-dependent deformation of damage zones*: In this chapter, we aim to delineate the fault damage zone in the Chelungpu fault system from geophysical logs and fracture density measurements. We compare damage-zone stress magnitudes to host-rock stress magnitudes. We search for potential evidence of time-dependent fracture healing in the damage zone from geophysical logs and stress magnitudes (reported in previous chapter). The field scale evidence of time-dependent deformation in the Chelungpu fault system underlines the need for laboratory experiments on damaged rocks.

3. *Quantify time-dependent deformation of damaged samples*: Since it is difficult to acquire cores and prepare samples from natural damage zone, we created analogue fractured rocks by impacting the samples at high strain rates. Following creation of such analogue damaged rocks, we tested the elastic, inelastic and time-dependent creep properties under in-situ stress conditions. Experimental results refined a visco-plastic constitutive model simulating experimental observations to characterize the rheology of the damaged rocks. Experimental and numerical results were combined with microstructural observations to explore qualitative and quantitative changes in porosity and contact junctions due to the experiments.

4. *Compare laboratory-obtained velocity recovery to recovery in natural settings*: In the final chapter, we evaluate how the time-dependent velocity increase in artificially created damaged material compares with post-seismic velocity recovery measured in the Chelungpu damage zone. Although pressure, temperature and fluid conditions in the laboratory cannot exactly match the natural setting, this comparison provides insights into the quality of damage we created artificially and creep mechanisms behind velocity recovery at constant stress stages.

References

Chester, F. M., Evans, J. P., and Biegel, R. L. (1993). Internal structure and weakening mechanisms of the San Andreas fault. *Journal of Geophysical Research: Solid Earth*, *98*(B1), 771–786.

Faulkner, D. R., and Rutter, E. H. (2003). The effect of temperature, the nature of the pore fluid, and subyield differential stress on the permeability of phyllosilicate-rich fault gouge. *Journal of Geophysical Research: Solid Earth*, *108*(B5). https://doi.org/https://doi.org/10.1029/2001JB001581

Faulkner, D. R., and Rutter, E. H. (2001). Can the maintenance of overpressured fluids in large strike-slip fault zones explain their apparent weakness? *Geology*, *29*(6), 503–506.

Fialko, Y. (2006). Interseismic strain accumulation and the earthquake potential on the southern San Andreas fault system. *Nature*, *441*(7096), 968–971.

Hennings, P., Allwardt, P., Paul, P., Zahm, C., Reid, R., Alley, H., et al. (2012). Relationship between fractures, fault zones, stress, and reservoir productivity in the Suban gas field, Sumatra, IndonesiaSuban Gas Field, Sumatra, Indonesia. *AAPG Bulletin*, *96*(4), 753–772.

Kaneko, Y., Ampuero, J.-P., and Lapusta, N. (2011). Spectral-element simulations of long-term fault slip: Effect of low-rigidity layers on earthquake-cycle dynamics. *Journal of Geophysical Research: Solid Earth*, *116*(B10).

Kitagawa, Y., and Kano, Y. (2016). Changes in permeability of the Nojima fault damage zone inferred from repeated water injection experiments. *Earth, Planets and Space*, *68*(1), 1–9.

Kitagawa, Y., Fujimori, K., and Koizumi, N. (2007). Temporal change in permeability of the Nojima fault zone by repeated water injection experiments. *Tectonophysics*, *443*(3–4), 183–192.

Lockner, D., Naka, H., Tanaka, H., Ito, H., and Ikeda, R. (2000). Permeability and strength of core samples from the Nojima fault of the 1995 Kobe earthquake. In *Proceedings of the international workshop on the Nojima fault core and borehole data analysis* (Vol. 129, pp. 147–152).

Pei, S., Niu, F., Ben-Zion, Y., Sun, Q., Liu, Y., Xue, X., et al. (2019). Seismic velocity reduction and accelerated recovery due to earthquakes on the Longmenshan fault. *Nature Geoscience*, *12*(5), 387–392.

Thakur, P., Huang, Y., and Kaneko, Y. (2020). Effects of low-velocity fault damage zones on long-term earthquake behaviors on mature strike-slip faults. *Journal of Geophysical Research: Solid Earth*, *125*(8), e2020JB019587.

Vidale, J. E., and Li, Y.-G. (2003). Damage to the shallow Landers fault from the nearby Hector Mine earthquake. *Nature*, *421*(6922), 524–526.

Xue, L., Li, H.-B., Brodsky, E. E., Xu, Z.-Q., Kano, Y., Wang, H., et al. (2013). Continuous permeability measurements record healing inside the Wenchuan earthquake fault zone. *Science*, *340*(6140), 1555–1559.

CHAPTER 2

Lithology and fault-related stress variations along the TCDP boreholes

Chapter published. Cited as:

Talukdar, M., Sone, H., and Kuo, L.-W. (2022). Lithology and fault-related stress variations along the TCDP boreholes: The stress state before and after the 1999 Chi-Chi earthquake. Journal of Geophysical Research: Solid Earth, e2021JB023290. https://doi.org/10.1029/2021JB023290

Abstract

Understanding the stress state both before and after an earthquake is essential to study how stress on faults evolves during the seismic cycle. This study integrates wellbore failure analysis, laboratory experiments, and edge dislocation model to study the stress state before and

after the Chi-Chi earthquake. The post-earthquake in-situ stress state observed along boreholes of the Taiwan Chelungpu-Fault Drilling Project (TCDP) is heterogeneous due to lithological variations. Along the borehole, we observe that drilling-induced tensile fractures are only present in sandstones, whereas breakouts are mostly present in silt-rich rocks. Laboratory experiments on TCDP cores also show that tensile and compressive strength are weaker in sandstones than in silt-rich rocks. These observations imply that both maximum and minimum horizontal principal stresses are higher in silt-rich intervals. Extended leak-off tests in the TCDP borehole also show lower minimum horizontal stress in sand-rich intervals, consistent with the above observations. We combine these observations to estimate a profile of stress magnitudes along the well which explains the variability of stress states found in previous studies. The stress heterogeneity we observed underlines the importance of acknowledging the spatial scale that a stress data represents. We then use an edge dislocation model constrained by GPS surface displacements obtained during Chi-Chi earthquake to calculate the coseismic stress changes. Our inferred pre-earthquake stress magnitudes, obtained by subtracting the coseismic stress change from the post-earthquake stress, suggests subcritical stress state before the earthquake above and below the fault despite the large displacements observed during the Chi-Chi earthquake in the region where TCDP encountered the fault.

2.1 Introduction

Stress in the earth's crust drives earthquakes, therefore characterizing the state of stress in the crust is essential for mechanistic assessments of seismic risk and hazard. Not only does stress drive earthquakes but earthquakes also modify the stress state in the crust by releasing and redistributing the stress in the surrounding crust. This feedback between earthquake and stress

occurs over a variety of length and time scales, highlighting the importance of understanding stress before, after and between earthquakes.

Scientific drilling in fault zones provide unique opportunities to study the magnitude of stress around faults and physical properties of rocks in the fault zone. Stress around boreholes induces wellbore failures like breakouts and drilling-induced tensile fractures, which allow us to infer the direction and magnitude of the principal stresses along the borehole. These stress induced wellbore failures, in combination with hydraulic fracturing tests and strength measurement on drilled core samples, provide opportunities to estimate the in-situ stress state (Moos and Zoback, 1990; Zoback et al., 2003). In the last two decades, major scientific drilling projects like San Andreas Fault Observatory at Depth (SAFOD), Japan Trench Fast Drilling Project (JFAST) and Taiwan Chelungpu Fault Drilling Project (TCDP) have provided key insights into the stress states after Parkfield, Tohoku and Chi-Chi earthquakes, respectively. Hickman and Zoback (2004) analyzed the well log acquired from SAFOD to suggest a transitional strike-slip to reverse faulting stress regime with high horizontal differential stress. Geophysical image logs acquired from JFAST suggests a stress state change from reverse faulting regime before the earthquake to normal faulting regime post-rupture due to coseismic stress release (Lin et al., 2013). This study further suggested a near complete shear stress release, down to ~0.3 MPa, after the Tohoku-Oki earthquake.

In the Taiwan Chelungpu-Fault Drilling Project (TCDP) penetrating the slip plane of the 1999 Chi-Chi earthquake, and International Continental Scientific Drilling Program (ICDP) project, previous estimates of in-situ stress calculated from well logs and core measurements do not provide a coherent understanding. Lin et al. (2006) first conducted anelastic strain recovery measurements on TCDP cores interpreting that the state of stress in the Chelungpu fault system

after the earthquake is normal faulting. Subsequent studies used extended leak-off tests, rock strength measurements and wellbore failure analysis to infer that the post-earthquake state of stress is normal fault to strike slip fault (Lin et al., 2007), strike slip fault (Hung et al., 2009), reverse fault (Haimson et al., 2010), transitional strike slip to reverse fault (Haimson et al., 2010). The relative magnitude of the principal stresses in these studies are shown in Figure 2.1 together with the frictional limit for optimally oriented faults drawn with a friction coefficient of 0.85 as the stress magnitudes are below 100 MPa (Byerlee, 1978). Since there is significant variability in the stress states inferred from these studies, it leaves a question about which stress state represents the correct stress state along the TCDP boreholes or whether the results reflect a heterogeneous stress state.

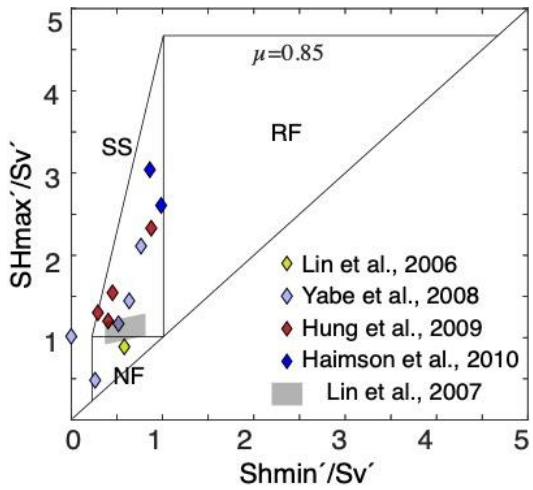

Figure 2.1. In-situ state of stress in the TCDP borehole reported in previous literature compared with frictional limits on horizontal stress magnitudes imposed by coefficient of friction of 0.85. The effective horizontal stress magnitudes are normalized.

There are multiple causes of stress heterogeneities in the crust. While some studies suggest difference in strength and physical properties as the major cause of stress heterogeneity

indicating an apparent lithology control (Bourne, 2003; Gunzburger and Cornet, 2007; Gunzburger and Magnenet, 2014; Sone and Zoback, 2013; Zhang and Zhang, 2017), other studies have also indicated that slip along secondary faults and fractures can lead to stress perturbation as observed in boreholes (Barton et al., 1988; Day-Lewis et al., 2010; Shamir and Zoback, 1992). Furthermore, geometry of faults and presence of asperities on fault planes control slip distributions (Segall and Pollard, 1980; Sibson, 1985), which determines where and how stress redistributes due to slip along faults. There are rapid lithological variations in the Chelungpu fault system and many secondary faults observed in the TCDP cores (Hung et al., 2009). Therefore, we revisit the TCDP data to understand the potential cause of the in-situ stress variability.

Borehole log data and cores acquired from active fault zones after earthquakes provide information about the post-earthquake in-situ stress state. Conversely, it is the not the post-earthquake but the pre-earthquake crustal stress field that drives earthquakes. It is possible to infer pre-earthquake stress if we can estimate the coseismic stress changes from geophysical data and subtract from the post-earthquake stress observed in boreholes. Such knowledge about the pre-earthquake stress state can provide insights into whether the strength of the brittle crust is weak or strong relative to laboratory measured rock strengths.

In this study, we combine information of lithological variations, previous hydraulic fracturing data, new laboratory strength measurements of TCDP cores, and a comprehensive analysis of borehole data to infer the post-earthquake in-situ state of stress. We also evaluate the coseismic stress change using an edge dislocation model constrained by coseismic surface displacements, which is subtracted from the post-earthquake stress to infer the pre-earthquake

stress state. We finally discuss the criticality of the stress using the inferred pre-earthquake stress compared to laboratory measured strengths.

2.2 Geological Setting

The Taiwan mountain belt is geographically divided into the Coastal Plains, the Western Foothills, the Hsuehshan Range, the Coastal Ridge, the Longitudinal Valley and the Coastal Range (Ho, 1986). The boundary between the Coastal Plain and the Western Foothills is the converging margin of the northwesterly subducting Philippine plate under the Eurasian plate, which ruptured the Chelungpu fault and produced the 1999 Chi-Chi earthquake (Figure 2.2a).

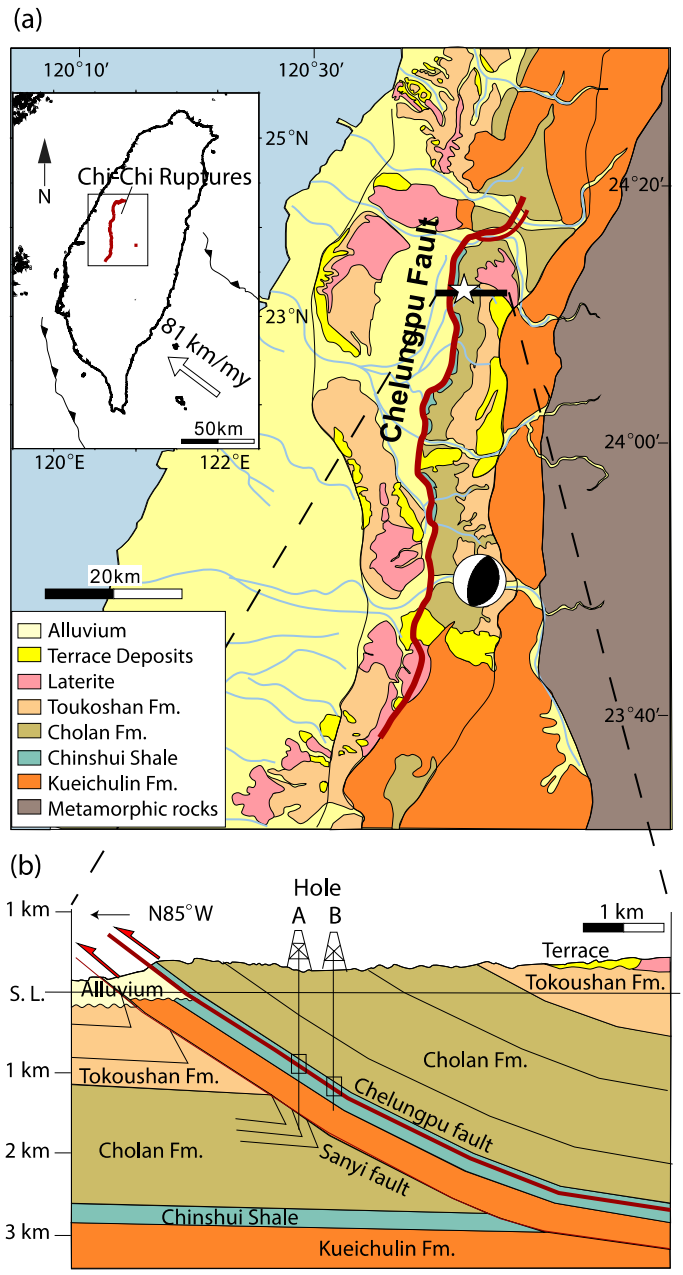

Figure 2.2. a) Geologic map of Central Taiwan showing the Chelungpu fault which ruptured during the 1999 Chi-Chi earthquake. The epicenter is shown by the location of the beach ball focal mechanism. The star shows the drill site. b) Taiwan-Chelungpu fault Drilling Project drilled two boreholes across the fault system Hole A and B (image modified after Hung et al. 2009, distance between Holes A and B are not to scale).

The September 21, 1999, Chi-Chi earthquake (Mw = 7.6) had an extensive surface rupture of 85 km along the Chelungpu fault, as shown by the dark red line in Figure 2.2a. The primary sense of slip was by reverse faulting (Ma et al. 1999). The rupture process started at the epicenter, 8 km below surface in the southern region of the fault (as shown by the beach ball in Figure 2.2a) and propagated to the north within a total time span of 30 seconds. Surface displacements of over 10 m were observed in the northern portion of the fault, and 1-4 m in the southern portion. Many studies on the collected seismic records have revealed the rupture process of the fault during the earthquake (Ma et al., 2001; Ji et al., 2001; Ji et al., 2003), and a remarkable contrast in the slip behavior between the northern and southern portion was found. Slip velocity was much faster in the northern portion (2- 4 m/s) than the southern portion (less than 1m/s), and seismic radiation was dominated by low frequency waves in the north, whereas in the south, higher frequency radiation was observed.

2.2.1 Taiwan Chelungpu-Fault Drilling Project

Taiwan Chelungpu Fault Drilling Project (TCDP) drilled two scientific research boreholes (Hole A and B) in the northern part of the Chelungpu fault, about 2 km east of the surface rupture near the town of Da-Keng, shown by the star in Figure 2.2a. The boreholes were drilled from 2004-2005, i.e. about five to six years after the earthquake. The boreholes intersect the primary slip plane which ruptured during the Chi-Chi earthquake at 1111 m (Hole A) and 1133 m (Hole B), respectively. The boreholes encounter lithological units and other faults, both dipping 30° to the east. Because Hole B is 40 m further east from Hole A, they penetrate similar lithological units and fault interfaces, but at slightly different depths from the surface (Figure 2.2b).

The drilling coring operation extended from 500-2000 m in Hole A and 950-1300 m in Hole B, as shown by the vertical cross section in Figure 2.2b. Geophysical logging data acquired during the drilling project include high resolution electrical resistivity image data recorded using the Formation Micro Scanner™ (FMS) and Formation Micro Imager™ (FMI). FMS collected resistivity image data in the upper portion of Hole A (500-1300 m) whereas FMI was used for the lower portion of Hole A (1200-1870 m) and the entire section of Hole B. Because the FMS tool contains only 64 sensor buttons compared to the 192 sensor buttons of the FMI tool, the FMS tool has less coverage of the borehole wall. We study these FMI and FMS logs in detail to characterize structures and lithological boundaries along the borehole. We also utilize the gamma ray and sonic log to draw inference on stress magnitude along the borehole.

2.2.2 Lithological variations

The Chelungpu fault system mainly comprises shallow dipping thrust faults, parallel to the bedding in the area (Sone et al., 2007; Yeh et al., 2007). The primary geological units in the upper 2 km are the Cholan Formation, Chinshui Shale and Kueichulin Formation in the hanging-wall block (Sheng-Rong et al., 2007), and then the Cholan Formation again in the footwall below the reverse fault (Figure 2.2b). Lithology in this area is characterized by alternating sandstone, siltstone and shale with the presence of intermediate stratigraphic units like silty sandstone, sandy siltstone, and inter-layered sandstone and siltstones (Sheng-Rong et al., 2007).

The natural gamma ray log is a measure to differentiate lithologies. Higher gamma ray is associated with higher potassium, uranium and thorium, usually present in clay minerals and organic materials present in the rock (Hassan et al. 1976). In TCDP rocks, the primary clay minerals present are illite, kaolinite, chlorite and smectite (Kuo et al., 2009). TCDP core observations confirm that the silt-rich layers correspond to higher gamma ray intervals than

sand-rich cores (Figure 2.3). Thus, we use gamma ray count as a proxy for lithological variations along the boreholes, setting gamma ray threshold values to classify the lithologies (Figure 2.3a, b). The litho-stratigraphic column obtained as such is consistent with those obtained from Song et al. (2007) based on direct core observations.

From the comparison of gamma ray logs from two boreholes, we observe that a 22 m upwards shift of Hole B data matches the Hole A gamma ray log, consistent with the local bedding dip of about 30° seen in drilled cores (Figure 2.3). Therefore, it is possible to combine observations from Hole A and B, allowing comparison of repeated but independent observations collected on the same lithological unit and structures.

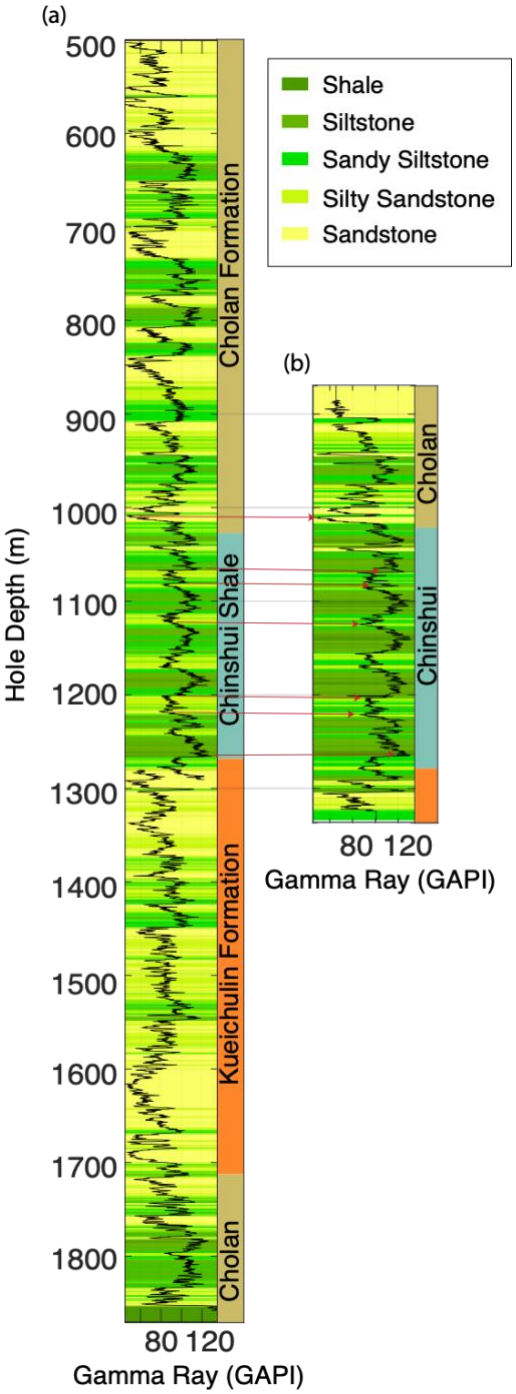

Figure 2.3. Gamma ray log in a) Hole A and b) Hole B logs used to define the lithology in the area. An upwards shift of Hole B gamma ray log by 22 m matches the Hole A gamma ray.

2.3 Wellbore failure

Drilling of boreholes in the earth perturbs the local stresses around the borehole. This perturbed stress on the borehole wall varies in magnitude as a function of azimuth according to the Kirsch equations (Kirsch, 1898). In a vertical wellbore, the effective circumferential stress, $\sigma_{\theta\theta} = S_{\theta\theta} - P_p$, at the borehole wall varies azimuthally as (Moos and Zoback, 1990).

$$\sigma_{\theta\theta} = S_{Hmax} + S_{hmin} - 2(S_{Hmax} - S_{hmin}) \cos 2\theta - 2\,P_P - \Delta P - \sigma^{\Delta T} \qquad (2.1)$$

where $S_{\theta\theta}$ is the circumferential stress at the borehole wall, S_{Hmax} and S_{hmin} are maximum and minimum horizontal principal stresses, respectively, θ is the angle from the azimuth of S_{Hmax}, P_P is the formation pore pressure, ΔP is the difference between the drilling mud pressure and the formation pore pressure, and $\sigma^{\Delta T}$ is the circumferential thermal stress induced by cooling of the wellbore. This equation assumes that the stresses are Andersonian, thus the vertical stress is a principal stress acting parallel to the borehole axis and that the rock is isotropic. We use a sign convention where compression is positive and extension is negative.

In a vertical borehole, maximum effective circumferential stress, $\sigma_{\theta\theta}^{max}$, occurs in the direction of S_{hmin} (θ =90°) and minimum effective circumferential stress, $\sigma_{\theta\theta}^{min}$, occurs in the direction of S_{Hmax} (θ=0°) (Figure2.6a). When these values exceed the compressive and tensile strength of the rock, wellbore failure occurs, namely breakouts and drilling-induced tensile fractures (DITFs), respectively. Therefore, occurrence and azimuth of breakouts and DITFs inform us about the direction and magnitude of horizontal principal stresses when combined with knowledge of the rock strengths.

2.3.1 Borehole Breakouts

We observed that breakouts are ubiquitous features along the TCDP wells, both in the FMS and FMI image logs. In these resistivity image logs, re-scaled to enhance the contrast, the

image section is lighter when sensing higher resistivity material and vice versa. In the TCDP borehole, the color variation is subtle between different lithologies because the higher porosity in the sand-rich formation and the higher clay-mineral content in the silt-rich formation both contribute to lowering resistivity. Nonetheless, silt-rich layers appear relatively darker than sand-rich layers (Figure 2.4).

Breakouts appear as dark out-of-focus zones with unclear boundaries that occur 180° apart from each other, reflecting the conductive mud present between the imaging tool and the formation. In Hole A and Hole B, breakout width is on average ~30°, mostly ranging between 15° and 45° (Figure 2.5b). Resistivity images at certain depths show disappearance of breakouts when there is a transition from a silt-rich stratigraphic unit to pure sand layers (Figure 2.4a, c, d). Breakouts are primarily present in siltstones and rarely present in sandstones. However, when present in sandstones, breakouts in sandstones are narrower in width compared to those in silt-rich layers. Comparison of breakout widths with lithological variation in Hole A shows how the breakout width is greater in siltstone compared to sandstones.

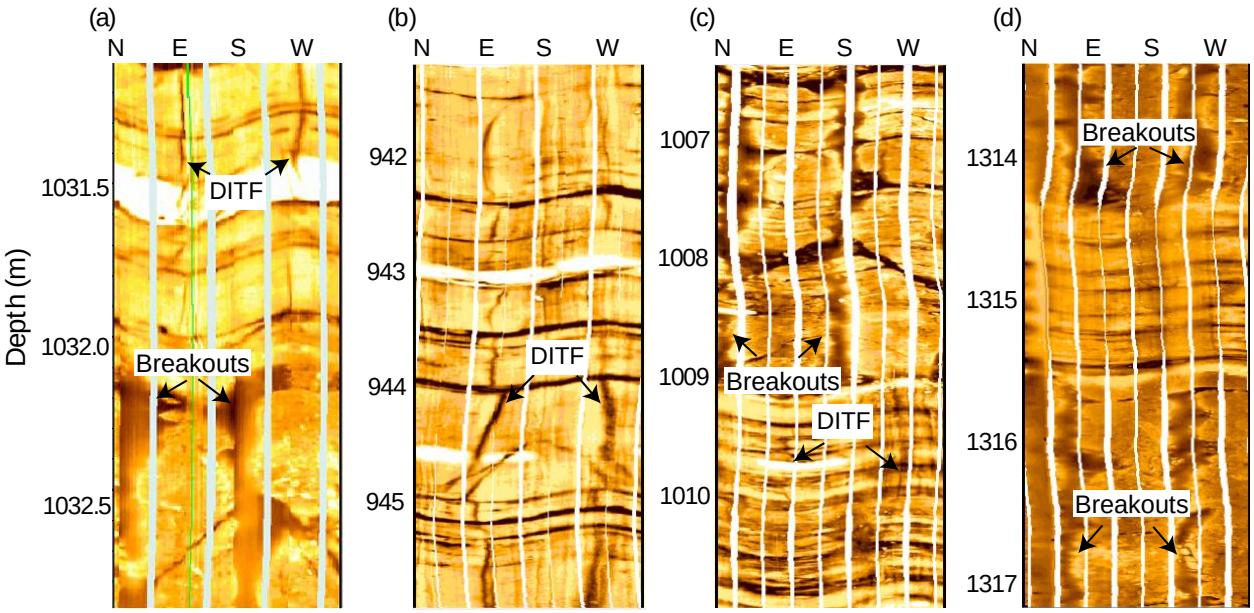

Figure 2.4. Occurrence of wellbore failures observed in the resistivity image logs. Lighter colors indicate higher resistivity (sand-rich) whereas darker colors indicate lower resistivity (silt-rich, shaley) rocks. a) DITFs are present until 1032 in sandstone with lighter shade whereas breakouts are only present in sandy siltstone below 1032 m with a comparatively darker shade. b) Presence of DITFs in sandstone. c) Transition from darker silt-rich layer to sand-rich layer at 1009 m show disappearance of breakouts and occurrence of DITFs in sandstone. d) Breakouts are only observed in the darker siltstone at the top and bottom of the figure. a,b,c are FMI images from Hole B whereas d is an FMI image from Hole A.

Utilizing the depth shift between Holes A and B determined from the natural gamma ray logs, we overlay the breakout azimuths information from Holes A and B (Figure 2.5a). Results shows that the breakout azimuths are consistent between the two boreholes and the mean breakout azimuth is around N20°E. This suggests that the direction of S_{Hmax} is N110°E (Figure 2.5a). We find no significant change in breakout azimuth down to 1300 m as Hung et al. (2009) also observed.

Note that the deviation of the borehole is only 3° until 1600 m and increases to 12° at 1830 m where the deepest breakout is observed. Previous studies have shown that deviation

below 12° does not influence the stress analysis using breakouts (Peska and Zoback, 1995), therefore the effect of deviation is neglected in this study.

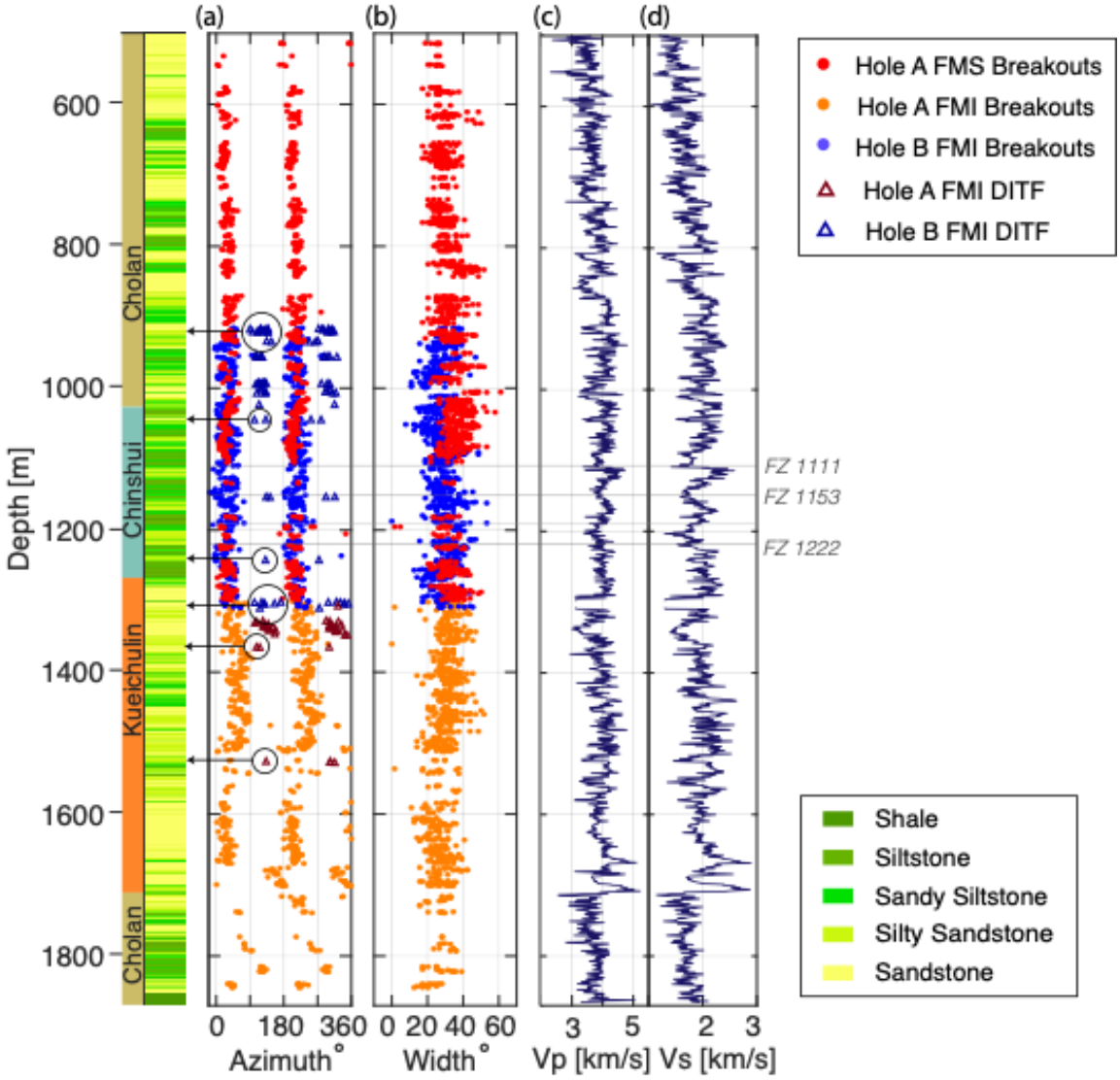

Figure 2.5. a) An overlay of breakout and DITF azimuths of Hole A and Hole B. b) Breakout width of Hole A and B combined. b) P and c) S wave velocity log data.

2.3.2 Drilling-induced tensile fractures

We identify DITFs as thin conductive fractures that occur parallel to or subparallel to the borehole axis. As in breakouts, the dark color reflects the conductive mud filling the fractures, but DITFs appear sharper because the borehole wall is not rugose. The azimuth of drilling-

induced tensile fractures (DITFs) in Hole A and B is approximately N110°E (Figure 2.5a), consistent with the breakout azimuth. Contrary to suppression of breakouts in sandstone layers, DITFs are primarily present in sandstone layers and absent in other lithologies (Figure 2.4b). A similar observation was made by Sone and Zoback (2014b) where they observed absence of DITFs in high gamma ray layers within the Barnett shale, Fort Worth Basin. Figure 2.5a also shows DITF presence in sandstone layers and absence in siltstone layers, as shown by black circles in the plot of breakout azimuth with depth. The upper part of Hole A image log studied using the FMS tool doesn't show DITFs because of the poor coverage and quality of the FMS data. In an FMS image log, the vertical white strips (or no data region) observed in Figure 2.4 are wider and could coincide with the azimuth where DITFs are observed in FMI images, potentially hiding DITF occurrences.

2.4 Strength of rocks

The uniaxial compressive strength of TCDP cores has been measured by various authors, and the results demonstrate a high degree of variability. Uniaxial compressive strength (UCS) of rocks cored at 1120 m (Hole B) depth was found to be 32.9 MPa and 44 MPa under water saturated and dry conditions, respectively (Chen, 2005; Lin et al., 2007). UCS of TCDP cores from 889-892 m (Hole A); however, was found to be almost twice at 79.5 ± 2.2 MPa (Oku et al., 2007) (Table 2.1). This variability in strength of TCDP cores is explained by the lithological variation as Hung et al. (2009) reports UCS of porous sandstone (Hole B) to be 8-11 MPa but that of homogeneous shale (Hole B) to be ~70 MPa. We also conducted UCS tests, which also suggests an increase in compressive strength with increasing silt content (for details of UCS tests, see appendix 2.9.1). Higher UCS of siltstones can be attributed to the porosity contrast of

sandstone and siltstone of TCDP cores. We found from helium porosimeter measurements that the porosity of sandstone (~20%) was higher than the siltstone variety (~6%).

We conducted Brazilian tensile tests on cores to find that the tensile strength also increases with increasing silt content (Table 2.1). The average tensile strength of sandstone (~ 0.5 MPa) was found to be significantly lower than siltstone (~ 7.5 MPa), with intermediate compositions such as silty sandstone and sandy siltstone showing 1.9 and 4.4 MPa, respectively. Our results are consistent with tensile strength inferred from extended leak off tests by subtracting reopening pressure from breakdown pressure (Hung et al., 2009), where the inferred tensile strength of sandstone and shale were 0.5 and 7.4 MPa, respectively.

Table 2.1. List of compressive and tensile strength measurements from the literature and this study.

Rock Type	*Hole, Depth*	*UCS (MPa)*	*Tensile Strength (MPa)*	*Reference*
Siltstone	A, 890 m	79.5 ± 2.2	N/A	(Oku et al., 2007)
Siltstone	B, 1031 m	76.4	N/A	This study
Siltstone	B, 1033 m	N/A	7.5 ± 0.5	This study
Siltstone	A/B	70	7.4	(Hung et al., 2009)
Sandy Siltstone	B, 746.5 m	58.3 ± 11	4.4 ± 0.4	This study
Silty Sandstone	B, 1120 m	32.9 (Wet), 44 (Dry)	N/A	(Chen, 2005; Lin et al., 2007)
Silty Sandstone	B, 1183 m	28.5 ± 3.2	1.9 ± 0.6	This study
Sandstone	A/B	9.5 ± 1.5	0.5	(Hung et al., 2009)
Sandstone	B (811.6 m)	N/A	0.5 ± 0.05	This study

2.5 Constraining principal stress magnitudes

The rock strength data together with the occurrences of breakouts and DITFs suggests that horizontal stress magnitudes are generally higher in silt-rich rocks. The preferential occurrence of breakouts in silt-rich rocks, despite their higher UCS, suggest that $\sigma_{\theta\theta}^{max}$ is greater in silt-rich rocks (Figure 2.6b). Since $\sigma_{\theta\theta}^{max}$ is a function of $3S_{Hmax} - S_{hmin}$ according to the Kirsch equations, presence of breakouts in the stronger silt-rich rocks is indicative of higher

S_{Hmax} in silt-rich layers. Similarly, the DITFs preferentially observed in sandstones, suggest that $\sigma_{\theta\theta}^{min}$ in sandstone is lower than -0.5 MPa, whereas DITF absences in silt-rich rocks suggest that the $\sigma_{\theta\theta}^{min}$ in siltstone is higher than -7.5 MPa (Figure 2.6b). In other words, the absolute value of tensile circumferential stress in sandstone is higher than its tensile strength and the absolute tensile circumferential stress in siltstone is lower than its tensile strength. Given that $\sigma_{\theta\theta}^{min}$ is a function of $3S_{hmin} - S_{Hmax}$, this is indicative of higher S_{hmin} in silt-rich layers than in sandstones. Therefore, horizontal stress magnitudes are overall more compressive in silt-rich rocks than in sandstones.

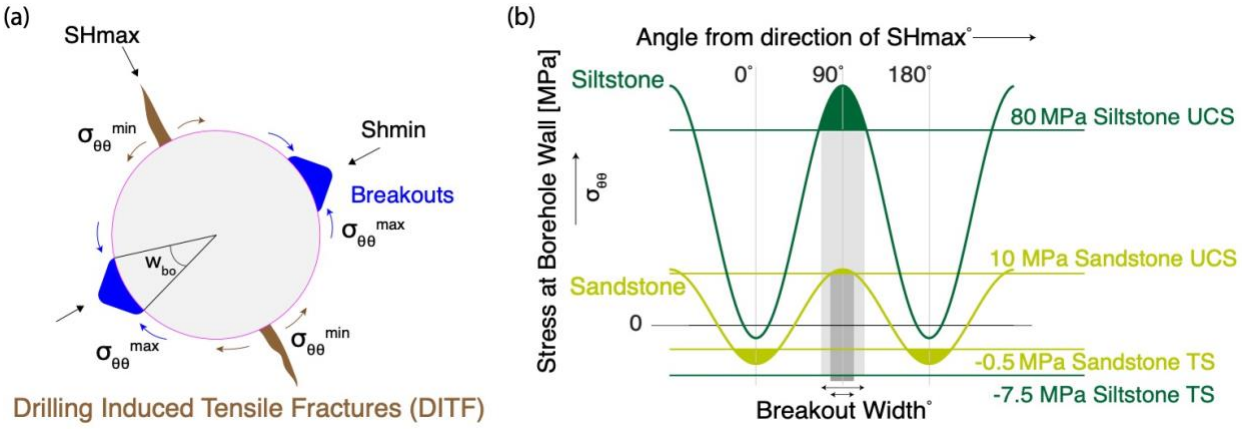

Figure 2.6. a) Cross-section of a borehole showing expected location of wellbore failures. Compressive failures occur as breakouts in the S_{hmin} direction where circumferential stress is most compressive ($\sigma_{\theta\theta}^{max}$). Tensile failures occur as drilling induced tensile fractures (DITFs) in the S_{Hmax} direction where circumferential stress is most tensile ($\sigma_{\theta\theta}^{min}$). b) Azimuthal variation of circumferential stress at the borehole wall with angle from direction of S_{Hmax} (vertical axis not drawn to scale). The green and yellow sinusoids are circumferential stresses within siltstone and sandstone, respectively. Presence of breakouts in siltstone and absence in sandstone imply higher compressive circumferential stress in siltstones than in sandstones. Tensile failures in sandstone imply lower minimum circumferential stress ($\sigma_{\theta\theta}^{min}$) than its tensile strength.

If we assume that breakouts span over the azimuthal range where $\sigma_{\theta\theta}$ exceeds the UCS, the S_{Hmax} magnitude is uniquely related to the breakout width.

$$S_{Hmax} = \frac{(UCS+2Pp+\Delta P+\sigma^{\Delta T})-S_{hmin}(1+2\cos(\pi-W_{bo}))}{1-2\cos(\pi-W_{bo})} \quad (2.2)$$

where W_{bo} is the angular width of the breakout, UCS is the uniaxial compressive strength, and remaining variables are the same as equation (2.1). Thus, if we know the pore pressure, mud pressure, thermal stress, UCS, and S_{hmin}, we can find the magnitude of S_{Hmax}. Note that this equation assumes an isotropic failure criterion, i.e., we do not consider the effects of bedding plane and bedding dip on the stress concentration and anisotropic strength of rocks (Lee et al., 2012). Equation (2.2) is also based on a Mohr-Coulomb failure criterion (friction angle is ignored because ΔP is zero) which does not consider the effect of the intermediate principal stress magnitude on rock strength, and thus also on the estimate of S_{Hmax} (Valley and Evans, 2019). We chose to use this relatively simple approach because not enough samples were available to characterize the polyaxial strength criteria for each rock type and our emphasis is on the effect of lithological variation which is reasonably captured by the variation in UCS.

The borehole is drilled at a constant overbalanced mud pressure suggesting that the borehole failures are caused by circumferential stress on the borehole wall. The mud pressure gradient used during TCDP drilling was 10.8 MPa/km whereas the hydrostatic pore pressure was measured to be 9.8 MPa/km (Hung et al., 2009). Some temporary variability in mud pressure at the bottom of the borehole could occur periodically, in depth, due to the push and pull of the bottom-hole assembly when connecting or disconnecting drill pipes. Its effect is neglected in this study as we do not see any periodic occurrences of wellbore failures and it is not impacting our calculation to the first order. Therefore, ΔP in the TCDP boreholes are taken to be 1 MPa/km. The vertical stress is calculated by integrating the density log.

Thermal stress is induced in the borehole wall due to cooling caused by the mud circulation, altering the stress magnitude at the borehole wall. To evaluate the magnitude of thermal stress caused by borehole cooling, we refer to temperature measurement conducted every three meters in TCDP Hole A after drilling (Kano et al., 2006). Kano et al. 2006 observed a linear thermal gradient of 22°C/km, whereas in a typical borehole, drilling mud temperature gradient is ~10-15°C/km (McDonald, 1976). Therefore, maximum temperature difference between mud and the formation at 2 km depth is less than 24°C. Given typical elastic and thermoelastic properties of sedimentary rocks, ΔT of 25°C only cause small changes in the estimate of stress magnitudes, on the order of several MPa (Zoback et al. 2003). We also note that this cooling-induced thermal stress promotes DITFs, but not breakout occurrence. If there is ample time for the borehole wall temperature to re-equilibrate with the surroundings before image logs are acquired, the thermal stress effect will diminish over time and its influence on the S_{Hmax} estimate derived from breakout width will become further insignificant. Therefore, we proceed with the analysis neglecting the thermal stress term.

2.5.1 Constraining S_{hmin} magnitude

Extended leak-off tests were conducted in TCDP Hole B at four different depths: 1019.5 m, 1085 m, 1179.0 m and 1279.6 m (Hung et al., 2009). Using the leak-off test data, Hung et al., (2009) inferred S_{hmin} from instantaneous shut-in pressure (ISIP) of the first two injection cycles as 16.3, 23.8, 16.2 and 19.6 MPa for the four depths indicated above, respectively. We note that the shut-in pressures of the first two injection and shut-in cycles were nearly the same for all tests except for the one at 1279.6 m. Haimson et al. (2010) reanalyzed the extended leak-off tests and interpreted those shut-in pressures from the leak-off test at 1279.6 m is 29.8 MPa instead of

19.6 MPa, due to a leak in the second cycle. All of these measurements suggest that the S_{hmin} is smaller than the vertical stress, S_v, thus a normal or strike-slip faulting environment.

We expect the magnitude of S_{hmin} to increase with depth along the borehole (i.e. horizontal stress gradient). We observe an increase in S_{hmin} readings with depth from 1019.5 m to 1085 m. The next S_{hmin} measurement at 1179.0 m is 16.2 MPa, lower than the shallower reading of 23.8 MPa at 1085 m. The leak-off tests suggest that there are heterogeneities in the S_{hmin} gradient along the borehole. Stress memory experiments by Yabe et al. (2008) and anelastic strain recovery data by Lin et al. (2006) also show heterogeneity in the S_{hmin} gradient. Previous S_{hmin} measurements are summarized in appendix 2.9.3.

Heterogeneity in S_{hmin} gradient around the Chelungpu fault system could be a result of differential response of the lithological units to tectonic loading. Such lithology-dependent change in S_{hmin} magnitude was attributed to variation in elastic properties of intercalated Devonian shale, sandstone and limestone layers by Evans et al. (1989a). Hydraulic fracturing observations by Evans et al. (1989b) showed that stiffer beds have higher S_{hmin} compared to compliant beds. In TCDP, we observed similar correspondence between formation stiffness and S_{hmin}. Such correlation can be understood to be a result of uniform horizontal tectonic strain applied to formations of varying stiffness (e.g., Bourne, 2003). Under uniform tectonic strain, larger horizontal stress arises in the stiffer siltstone layers, and lower horizontal stress in the compliant sandy layers.

To evaluate the variation in S_{hmin} caused by tectonic deformation, we consider a layered rectangular media deformed uniformly by horizontal tectonic contraction (Δe_{Hmax}) (Thiercelin and Plumb, 1994). We can calculate the stress change induced in the direction perpendicular to the tectonic contraction, corresponding to S_{hmin}, using the Hooke's law of elasticity and invoking

two boundary conditions: 1) traction-free top surface, and 2) plane strain condition in the vertical plane parallel to the tectonic loading direction (i.e., infinite horizontal extent in the load perpendicular direction) (See appendix 2.9.2 for derivation)

$$\Delta S_{hmin} = -\Delta e_{Hmax}\, vE / (1-v^2) \qquad (2.3)$$

Thus, the change in S_{hmin} is a function of the applied uniform strain, Young's Modulus *E* and Poisson ratio *v*. We calculate *E* and *v* from velocity and density logs to obtain a profile of $vE/(1-v^2)$ with depth. $vE/(1-v^2)$ and S_{hmin} gradient show a positive correlation with R squared value of 0.19 (Figure 2.7a). The correlation is indicative of how the elastic properties variation is controlling the S_{hmin} variation, but the weak correlation may also suggest the possibility of additional causes for the S_{hmin} variation.

Silt-rich layers are also rich in clay, which are more ductile and exhibit visco-plastic behavior (Sone and Zoback, 2014a; 2014b). Ductile deformation leads to long-term viscous relaxation of differential stress leading to increase in S_{hmin} in a normal or strike-slip faulting environment. Such S_{hmin} variation has been observed in shale-bearing basins (Gunzburger and Cornet, 2007; Gunzburger and Magnenet, 2014; Sone and Zoback, 2014a). Extensive hydraulic fracturing stress measurements in Piceance basin, Colorado, USA, showed that minimum horizontal stress is lower in sandstone than in shale or clay-rich rocks (Warpinski and Teufel, 1989; Y. Zhang and Zhang, 2017). Plumb et al. (1991) also suggests that S_{hmin} variations in shale bearing basins is not only a result of elastic stiffness but also the presence of clay. In TCDP, we see a strong positive correlation between S_{hmin} gradient and gamma ray, which is a proxy for clay-content (Figure 2.7b), consistent with the idea that S_{hmin} is relatively high in clay-rich formations because of viscous relaxation. Such a strong correlation may not apply in other wells.

The better correlation of gamma ray with S_{hmin} gradient compared to the elastic properties (Figure 2.7a, b) may suggest viscous relaxation as a more probable explanation for the S_{hmin} variation. Because clay-rich rocks are also stiffer in TCDP rocks (Figure 2.7c), it is possible that gamma ray is also simultaneously serving as a proxy for stiffness and reflecting the influence of elastic constant, $vE/(1-v^2)$, on S_{hmin}. Distinguishing the elastic and visco-plastic effects on S_{hmin} is not possible with available data and current technology, but it is plausible that both effects yield the current S_{hmin} variation.

In this study, we estimate the S_{hmin} profiles along the TCDP borehole using the linear empirical relations from figures 2.7a and 2.7b. A profile of S_{hmin} gradient is obtained utilizing the $vE/(1-v^2)$ and gamma ray profiles and applying the empirical relations. Then the depth is multiplied to obtain the profiles of Shmin based on the elastic properties and gamma ray. We only discuss the results obtained from the gamma ray-based approach here because the correlation with S_{hmin} gradient was better and it may potentially encompass the consequences of both elastic and viscous effects. The result obtained from the empirical relation with $vE/(1-v^2)$ are shown in the appendix for comparison (appendix 2.9.4), but the conclusions of the subsequent analysis do not change depending on which empirical relation is used.

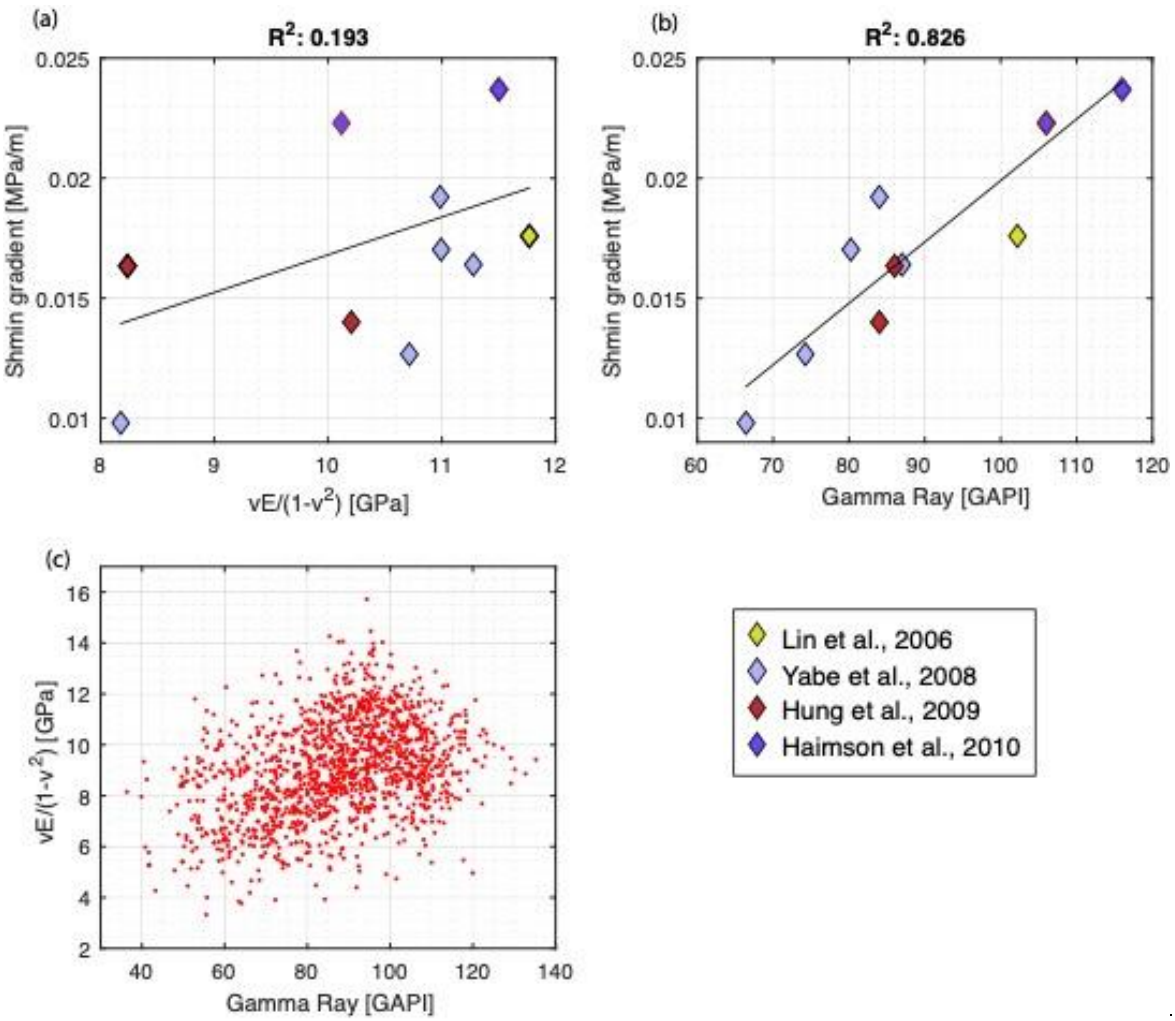

Figure 2.7 Correlations between S_{hmin} gradient, elastic properties, and gamma ray. a,b) Cross plot between S_{hmin} gradient (from previous literature) with $vE/(1-v^2)$ and gamma Ray. c) Cross plot between $vE/(1-v^2)$ and gamma ray.

2.5.2 Constraining S_{Hmax} magnitude

We can infer the magnitude of S_{Hmax} from the estimated S_{hmin} values and breakout width measurements using equation 2.2, if we have an estimate of compressive rock strengths. As a practical approach to estimating the UCS profile along the entire section of the TCDP borehole, we used the sonic log to estimate a profile of rock strength (Figure 2.5c, d). In Figure 2.8, UCS values are plotted against P wave velocity (Vp) corresponding to the depths of core samples

tested in the lab. The vertical error bars indicate the range of UCS values within a sample group. The horizontal error bars indicate the range of Vp values within a ± 0.5 meter interval around the sample depth. The robust positive correlation between Vp and UCS is evident, thus we establish an empirical relationship between the two parameters to capture the variability in UCS along the borehole. We note that this empirical relationship is qualitatively consistent with the strength reduction expected in fault zones. Although strength measurements of fault zone rocks were not possible due to the lack of intact samples, increase in fracture density generally cause reduction in both UCS and Vp (Fan et al., 2018; Hoek and Brown, 1980).

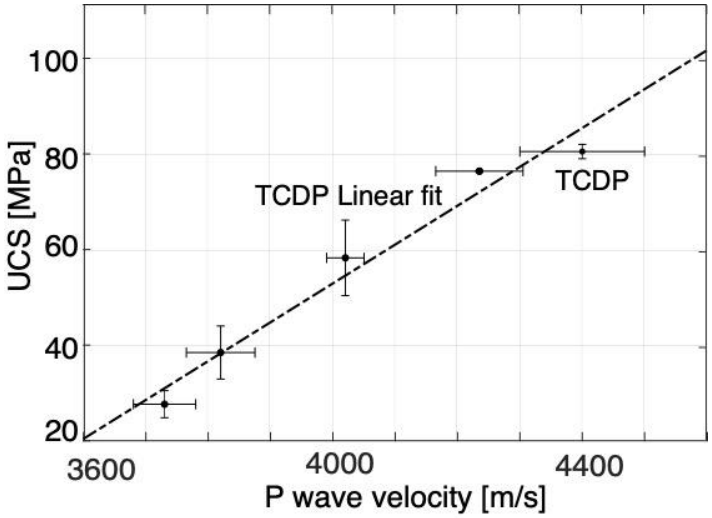

Figure 2.8 UCS of TCDP rocks plotted against P wave velocity from the sonic log.

Combining information from the estimated UCS profile, breakout width (Figure 2.5b) and estimated S_{hmin} profile (Section 2.5.1) into equation 2.2, we can determine the magnitude of S_{Hmax} at those depths where the breakout width data is available (Figure 2.9a). Where no breakouts are observed in the image log, we provided bounds on the S_{Hmax} value, unless the lack of breakout data was due to poor image quality. Based on equation 2.2, absence of breakouts provides an upper limit to the magnitude of S_{Hmax} given a S_{hmin} magnitude.

Figure 2.9 shows the resulting near-continuous profiles of the lithology-dependent stress state as inferred qualitatively from figure 2.7, 2.8. We see that the S_{Hmax} magnitudes constrained by breakout width (solid green symbols in figure 2.9b) generally plot at higher magnitudes compared to the upper limit of S_{Hmax} determined by the breakout absence (open green symbols in figure 9b). Because breakouts primarily occur in silt-rich layers and breakouts are absent in sand-rich layers, this signifies the generally higher S_{Hmax} magnitude in silt-rich layers and vice versa. This is because 70 MPa difference in UCS between siltstone and sandstone would require, for instance, a 70x3 = 210 MPa difference in S_{hmin} to explain the difference in breakout occurrence between siltstone and sandstone, if there is no variation in S_{Hmax}. We do not observe such large variation in S_{hmin}, so difference in S_{Hmax} is most likely the primary reason for the difference in breakout occurrence.

We note that the FMS image logs recovered from the upper section of TCDP Hole A, in general has poor azimuthal coverage due to the smaller number of sensor buttons on the tool. Caliper logs also showed that borehole enlargement occurred at some depths, likely due to the longer time between drilling and logging, further reducing the azimuthal coverage and degrading the image quality due to rough borehole walls. Thus, breakout width is not always measured with high accuracy. We expect a maximum error in breakout width to be approximately 15°. For a 35° width breakout found at 10 MPa pore pressure, 50 MPa UCS, and 20 MPa S_{hmin}, uncertainty of 15° in breakout width translates to S_{Hmax} uncertainty of ±1.4 MPa. Thus, the uncertainty of S_{Hmax} due to error in breakout width is relatively small compared to its magnitude. Therefore, the error bars are not shown in Figure 2.9 for clarity.

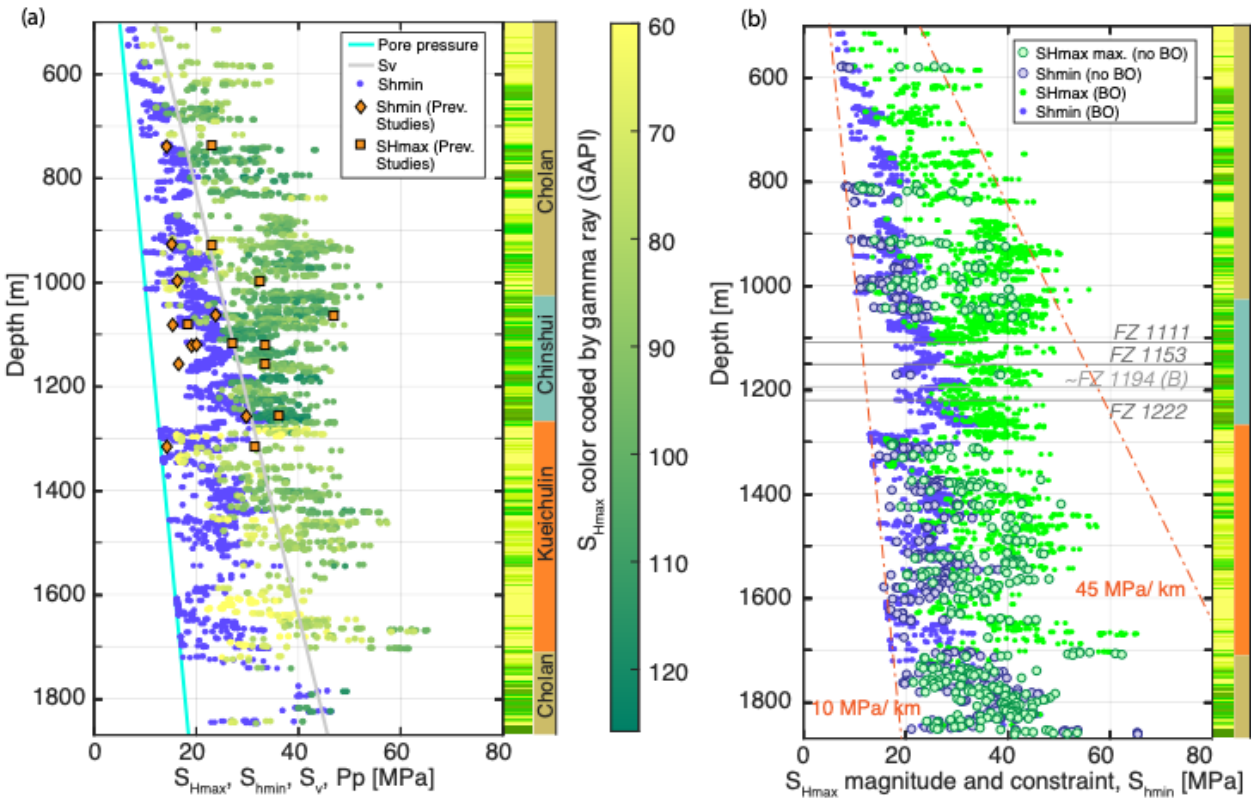

Figure 2.9.a) Profile of three principal stress magnitudes with depth. Estimates of S_{hmin} and S_{Hmax} are low for sand-rich layers and high for silt-rich layers. b) Upper limit of S_{Hmax} from absence of breakouts given a S_{hmin} magnitude is overlaid on stress magnitudes in regions of breakout occurrence.

2.6 Pre-earthquake stress

To be able to understand the stress conditions leading to failure, we attempt to estimate the pre-earthquake stress state before the Chi-Chi earthquake. We can infer the pre-earthquake stress field if we can calculate the coseismic stress changes. In this section, we use dislocation theory to model the displacement field caused by slip on the Chelungpu fault and use Hooke's law to obtain corresponding stress changes.

We compute displacements in a two-dimensional vertical cross section due to a uniform slip along a reverse fault using solutions derived in Segall (2010). The solution combines the Volterra's formula with the Melan's Green function (Melan, 1932) to obtain displacements due

to an edge dislocation (See appendix 2.9.5 for details). The cross section on which we calculate the solution extends in the vertical direction (x_2 direction) and the horizontal direction (x_1 direction) perpendicular to the strike of the Chelungpu fault, i.e., East-West (Figure 2.10a). There is no displacement along the x_3 axis parallel to the strike of the fault (i.e., plane strain). This assumption holds to the first order because the geological structure continues along the strike of the Chelungpu fault (Figure 2.2). The fault is considered to be a combination of two edge dislocations in a homogeneous, isotropic, linear elastic half space. Two edge dislocations with opposite slip sense are superposed, one at the free surface on the fault trace and the other at the downdip limit of the fault. The reverse fault we consider dips at 30° and extends 15 km in the downdip direction along the fault. Although simplistic, this two-dimensional model has been found to capture the essential first-order feature of the observed displacement field of the Chi-Chi earthquake (Segall, 2010).

In order to constrain the 2D coseismic displacement field near the TCDP borehole, we referred to the strike-normal horizontal and vertical surface displacements (u_1 and u_2) obtained from GPS data in previous literatures (Ji et al., 2001; Johnson et al., 2001; Yu et al., 2001, 2003) (See appendix 2.9.6). Here fault strike is almost North-South (Figure 2.2a), thus the horizontal and vertical axis in the fault dislocation model corresponds to the eastward and upward directions, respectively (Figure 2.10b). GPS displacement in the region where the TCDP boreholes were drilled show that the coseismic horizontal displacement perpendicular to the fault strike was ~4.5 m and vertical displacement was ~2.9 m (Yu et al., 2001). We find that a slip amount of 8 m on the fault plane reproduces these vertical and horizontal surface displacements to a reasonable degree as shown in Figure 2.10b.

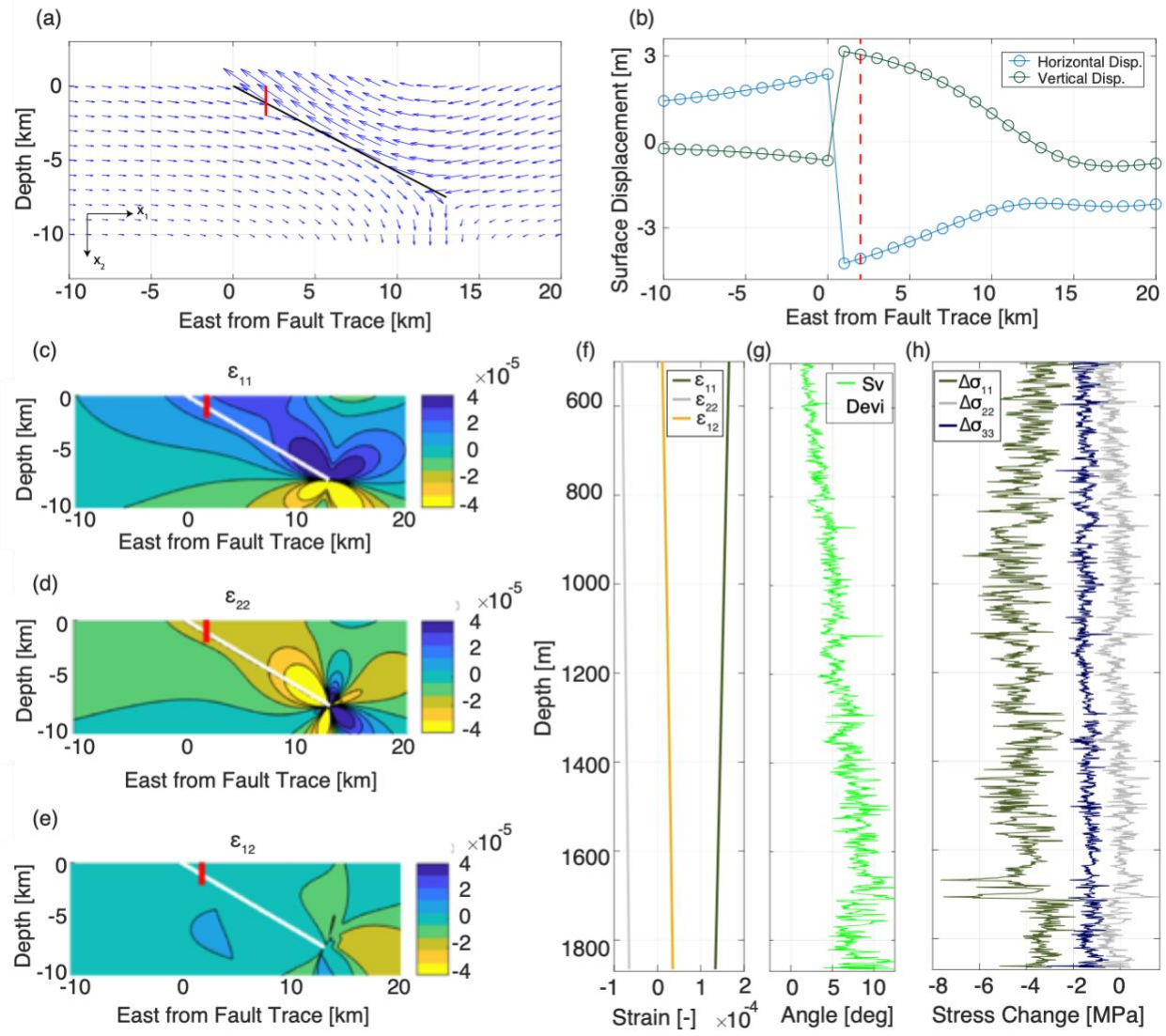

Figure 2.10. a) Displacement field induced by a reverse fault dipping at 30° with 8 meters fault slip. The edge of the fault is 13 km east of the fault trace on the surface. The red line shows the location of the TCDP borehole, which is ~1.92 m east of the fault intersecting the fault plane at 1111 m; b) The eastward and vertical surface displacement. The red line shows the location of TCDP 1.92 km east of the fault; c-e) strain tensor components derived from the displacement field solution; f) Strain component profiles along the TCDP boreholes 1.92 km east of the fault; g) Deviation of σ_{22} from vertical is less than 15°; h) Corresponding stress component changes obtained from the strain profile, elastic properties based on the sonic log data, and plane strain boundary condition.

Differentiating the displacement field constrained above, we calculate the corresponding normal ($\varepsilon_{11}, \varepsilon_{22}$) and shear strain fields (ε_{12}) (Figure 2.10c, d, e). We obtained a vertical transect of strain measurement at a distance of 1.92 km East of the fault trace, corresponding to the TCDP borehole location intersecting the Chelungpu fault at 1111 m depth (Figure 2.10f). The 2D strain tensor components are used to calculate the coseismic stress change along the TCDP borehole by applying the Hooke's law with plane strain boundary condition. To acknowledge the large variability of the elastic properties in the TCDP region, we use elastic constants recovered from the sonic log data (Figure 2.6f, g), although the dislocation model is computed using uniform elastic properties (Table 2.S4). Since we assumed plane strain condition with no changes in strain along the strike of the fault (=0), $\Delta\sigma_{33}$ is calculated as $\Delta\sigma_{33} = \nu(\Delta\sigma_{11} + \Delta\sigma_{22})$ (Figure 2.10h).

Coseismic stress change calculated along the TCDP borehole shows that the change in shear stress component is non-zero, $\Delta\sigma_{12} \neq 0$ (Figure 2.10h). This indicates that the principal directions of the coseismic stress change are not necessarily aligned with the x_1 and x_2 axes. The deviation of the most vertical principal direction (of the stress change) from the x_2 axis is shown in Figure 2.10g which reaches 13° at deeper depth. 13° is less than the uncertainty of the principal stress directions inferred from the wellbore failure observations. Therefore, for simplicity, we directly subtract the magnitudes of coseismic stress change $\Delta\sigma_{11}$, $\Delta\sigma_{22}$ and $\Delta\sigma_{33}$ from the post-earthquake principal stress magnitudes S_{Hmax}, S_v and S_{hmin}, respectively, to obtain the pre-earthquake principal stress magnitudes (Figure 2.11).

In Figure 2.11, the darker colors show pre-earthquake principal stress magnitudes whereas the lighter colors represent post-earthquake principal stress magnitudes. Since $\Delta\sigma_{11}$ component of the stress change tensor has the highest magnitude (Figure 2.10h), S_{Hmax} shows the

highest increase in its magnitude from post to pre-earthquake. Increase in S_{hmin} from post to pre-earthquake is less significant than S_{Hmax}. The pre-earthquake S_v is not distinguishable from post-earthquake S_v in Figure 2.9 because coseismic changes in vertical stress are close to zero (Figure 2.10h). We also note here that since the vertical stress is almost the same before and after the earthquake but coseismic S_{hmin} decrease was substantial, there are certain depths where the faulting environment is estimated to have transitioned from strike-slip before the earthquake to the current normal faulting environment after the earthquake. Similarly, substantial S_{hmin} change close to the fault zone suggests that the pre-earthquake faulting environment was reverse faulting stress state instead of the current strike-slip environment.

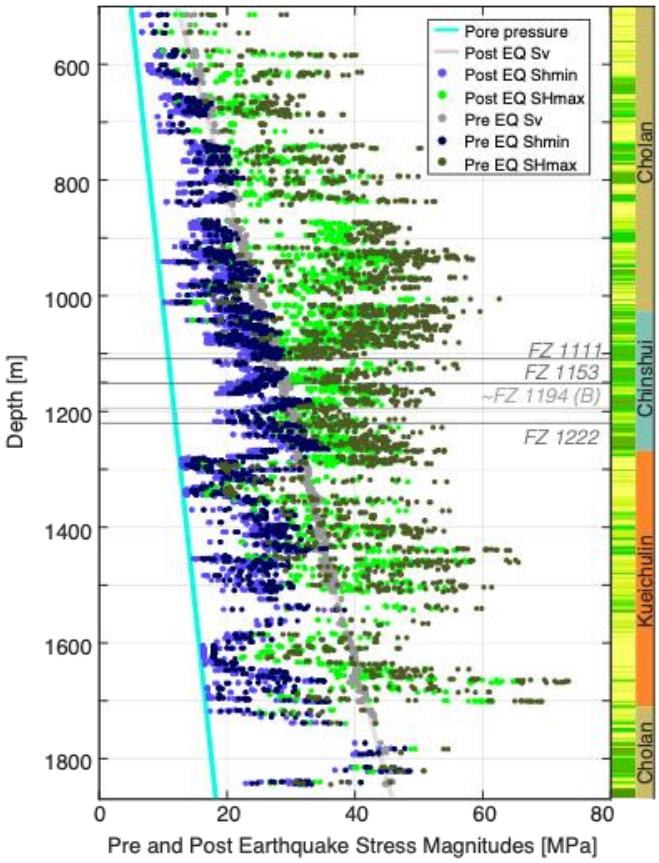

Figure 2.11. Pre-earthquake stress magnitudes plotted with the post-earthquake stress magnitudes. Increase in S_{hmin} and S_{Hmax} magnitudes pre-earthquake and insignificant difference in S_v magnitude.

2.7 Discussion

2.7.1 Lithology-dependent stress change

The superposition of previous stress magnitude calculations obtained by various methods on our results suggest that our estimated stress profile acknowledging the layer-by-layer rock property changes is able to capture the stress heterogeneity (Figures 2.9a, 2.12a). The inconsistency in previous stress estimates was primarily because these studies analyzed stress at different depth where a wide range of lithology was encountered. In Figure 2.12a, we observe that the most sand-rich layers plot towards the normal faulting environment whereas the most silt-rich layers plot in the strike-slip/reverse faulting regime. The intermediate compositions fall in the strike slip regime. Thus, stress is generally more compressive (i.e., higher S_{Hmax} and S_{hmin}) in silt-rich layers compared to sand-rich layers, as was also seen in Figure 2.9.

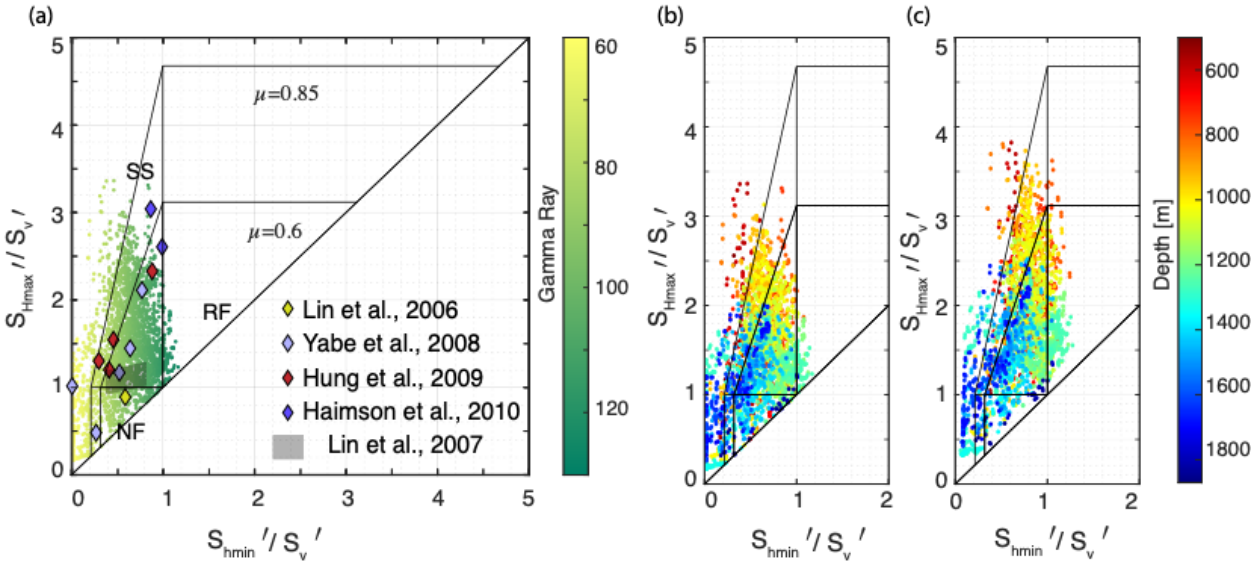

Figure 2.12. Calculated post and pre-earthquake effective horizontal stress magnitudes compared with the frictional limits (i.e., stress polygon) and previous stress measurements. a) Comparison with previous observations. b, c) Post-earthquake and pre-earthquake stresses color coded with depth and compared with the stress polygon, respectively.

As described in section 2.5, the predicted stress magnitude variation closely follows the variation in data used for the stress calculations. Since we calculate S_{hmin} from gamma ray log (Figure 2.7), increase in S_{hmin} between 1050-1280 m is predominantly due to the presence of silt-rich facies in the Chinshui Shale (Figure 2.9a). On the other hand, from equation 2.2, we see that S_{Hmax} magnitude is influenced by various parameters. Given the negligible variation in thermal stress, mud pressure, and pore pressure, we find that S_{Hmax} magnitude is mostly influenced by the UCS and S_{hmin} variation. For breakout width below 60°, equation 2.2 shows that the estimated S_{Hmax} magnitude has a positive correlation with UCS and S_{hmin}. Therefore, calculated S_{Hmax} is higher in silt-rich layers reflecting both the higher UCS inferred from the higher Vp and the higher S_{hmin} magnitude inferred from the higher gamma ray values. Higher S_{Hmax} in silt rich layers can also be understood by the elastic layered media model we discussed in section 2.5.1 and appendix 2.9.2. On applying layer parallel strain to a layered formation with stiff silt layers and compliant sand layers, stress accumulation will be greater in the stiff silt layers leading to higher stress magnitude in the S_{Hmax} direction parallel to the direction of loading.

Both the pre- and post-earthquake stress profiles we obtained show a transition in stress state below 1300 m depth upon entry into the Kueichulin formation, which is a sand rich layer. At depth range 1300-1450 m, the stress state is primarily normal faulting environment, and the stress state is less compressive below 1450 m compared to the shallower sections. In this sandstone rich formation from 1300-1450 m, breakout azimuth deviates from the general trend of 20° to almost 80° (Figure 2.5a). Because the empirical relationships used in the stress calculation

is primarily based on hydraulic fracturing and rock strength data collected from the shallower sections, it is somewhat questionable whether these observations do reflect true changes in stress state in the deeper section of the TCDP borehole.

The formation scale changes in stress magnitude in sandstone rich Kueichulin formation are consistent with inferences from other studies. For example, an analysis of optimally oriented planes determined from stress change in combination with earthquake focal mechanism showed that the stress state changes at 1300 m around the Kueichulin formation top (Chan et al., 2012). Chan et al. (2012) suggests that the state of stress in TCDP is strike slip to reverse fault between 900-1300 m, but the faulting environment switches to normal faulting at 1300 m. Yabe et al. (2008) conducted stress memory experiments through analysis of deformation rate and acoustic emission rate on TCDP cores. Above 1150 m, results showed strike slip faulting, whereas one core from 1316 m showed $S_{Hmax} = S_v$, denoting a normal fault to strike slip faulting environment. These results are consistent with the less compressive stress states in sandstone inferred from our stress profile. The consistency of our observations with previous studies suggest that our stress measurements are relevant to some degree below 1300 m, even though empirical relationships used in this study are derived from data in the shallower section.

2.7.2 Fault related changes in stress

We also observe formation-scale stress changes that occur in the Chinshui Shale. Stress gradient lines in Figure 2.9b shows that S_{Hmax} magnitude below 1050 m depth, entering the Chinshui Shale, becomes consistently lower than the 45 MPa/km gradient line. On the other hand, the S_{hmin} magnitude between 1050-1280 m in the Chinshui Shale is higher than the surrounding formations as can be seen by the comparison with the 10 MPa/km gradient line. S_{hmin} increase in Chinshui shale is a direct consequence of lithology dependence, for which

gamma ray log is a proxy. The decrease in S_{Hmax}; however, is not caused by lithology. As discussed above, for breakout widths narrower than 60°, the higher S_{hmin} and UCS within silt-rich rocks should generally lead to higher S_{Hmax} estimates if stress is solely controlled by lithology. The decrease in S_{Hmax} magnitude estimate is a consequence of low material strength as inferred from the decrease in velocity of damaged rocks in the vicinity of the Chelungpu fault (Yeh et al., 2007). Thus, in the Chinshui Shale, S_{Hmax} magnitude is influenced by both lithology and fault-related damage.

The decrease in S_{Hmax} magnitude and the increase in S_{hmin} magnitude close to the fault leads to a relatively isotropic stress state. Figure 12b shows that the stress states corresponding to depth range 1100-1250 m around the Chelungpu fault zone plots close to the point where S_v= S_{Hmax}= S_{hmin}. Faulkner et al. (2006) suggest that reduced stiffness and increased Poisson ratio of damaged rocks can lead to a decrease in differential stress close to the fault core. While the cause of such isotropic stress state is unknown, Ma et al. (2012) analyzed micro-earthquakes observed by borehole seismometers installed in TCDP and also suggested that isotropic events with no identifiable shear waves components were dominant in the vicinity of the fault, indicative of isotropic stress states near the fault zone.

Plot of breakout azimuth with depth shows that the breakout azimuth until 1300 m is fairly continuous (~30°) with no major azimuthal change going through the Chelungpu fault zone (Figure 2.5b). This indicates that there are no major changes in the azimuth of the horizontal principal stresses (or stress rotation) caused by fault slip within the volume investigated by the TCDP borehole. Our observation is contrary to some previous studies which suggest 90° rotation of S_{Hmax} across the primary slip plane (Lin et al., 2007; Wu et al., 2007), but is consistent with Hung et al., (2009) that also suggests no stress rotation.

In general, local stress perturbations caused by fault slip occur due to the development of stress singularities where there is an abrupt change in the amount or direction of fault slip, for instance at the periphery of a large slip patch or at geometrical irregularities. Thus, the overall spatial scale at which the stress perturbation occurs is mostly governed by the length scale of the area of highest slip. For example, in the edge dislocation model in Figure 2.10, stress concentration occurs at the edge of the fault where there is an abrupt termination of fault slip, and the stress perturbation extends in the entire region surrounding the fault. Slip distribution on the Chi-Chi earthquake has been inverted by many authors based on GPS, InSAR and teleseismic data (Ji et al., 2001; Johnson et al., 2001; Ma et al., 2001; Zhang et al., 2008). Despite the differences between these results at finer scales, a common feature that arises in these models is a large slip patch under the TCDP borehole with a length scale of at least 10 km. The slip distribution in this northern slip patch is also suggested to be homogeneous based on the depletion of high frequency content in the strong motion record from the northern section of the Chi-Chi slip plane. Therefore, we expect that the stress perturbation caused by the Chi-Chi earthquake in the volume surrounding TCDP boreholes would manifest itself over the entire extent of the borehole rather than locally at the fault zone depths.

2.7.3 Pre-earthquake stress compared with frictional limits

The cross plot of pre-earthquake horizontal principal stress magnitudes (Figure 2.12c), normalized by the vertical stress, show that our stress calculation results are valid within the physical limits set by a frictional coefficient of 0.85. The majority of the data points plot within the strike-slip and normal faulting regimes of the stress polygon and very few plot within the reverse faulting regime. This signifies that the pre-earthquake stress was not in a state of criticality by reverse faulting in the northern part of the fault where TCDP encountered the fault.

This may indicate that the state of stress was critical by reverse faulting only in the southern part of the fault where the rupture nucleated (Ma et al., 2003) and subcritical in the northern part of the fault. The largest fault slip; however, was observed in the slip patch identified around the TCDP borehole area reaching fault slips of about 10 meters. This high slip amount despite sub-critical stress state in the region may be consistent with the notion that dynamic fault-weakening mechanisms operated at the northern segment of the fault, as suggested by various authors, such as hydrodynamic lubrication (Kanamori and Brodsky, 2004) and thermal pressurization (Noda and Lapusta, 2013; Sone et al., 2007; Tanikawa and Shimamoto, 2009). Our pre-seismic and post-seismic stress results provide an important constraint in studying the coseismic mechanical processes along seismogenic faults.

2.7.4 Uncertainty in the Coseismic Stress Model

Various simplifications were made when calculating the coseismic stress change. One can prefer to use three-dimensional heterogeneous coseismic slip distributions determined from inversion of seismic and geodetic data, which may be better than the uniform slip assumption we made. However, between the various slip models of the Chi-Chi earthquake (Ji et al., 2001; Johnson et al., 2001; Ma et al., 2001; Yu et al., 2001; 2003; Zhang et al., 2008), there is only agreement in the first order pattern of greater slip in the northern half of the fault and less in the southern half. The finer details are different depending on the data and methodology used, which would lead to non-unique results if one were to employ the slip models to calculate coseimic stress change.

Although the along-strike length of the ruptured Chelungpu fault (~85 km) was much greater than the depth extent (~15 km), the plane strain boundary condition assumed in the displacement solution may not fully hold because of along strike variability in fault slip. The

assumption of uniform fault slip in the model also does not capture the along-dip heterogeneity found in Chi-Chi earthquake slip models. The coseismic stress change was also calculated neglecting strike-parallel slip components, but the Chelungpu fault did not rupture in a pure reverse faulting sense close to the TCDP drill site. Rake angles are close to 45° according to some studies (Ji et al., 2001; 2003). Such oblique slip component will cause out-of-plane components of the coseismic stress change which is not accounted for in our calculations. Nonetheless, TCDP is situated within the largest slip patch of the Chi-Chi earthquake, suggesting that the slip distribution was relatively homogeneous around TCDP. The magnitude of the coseismic stress change is also found to be relatively small compared to the absolute stress magnitude, thus the influence of heterogeneous slip and oblique fault slip will not largely change our estimate of the pre-earthquake stress state. Although the result presented here should be taken as a first order estimate, the conclusions of our study are not expected to change upon acknowledgment of the finer details of the fault slip pattern.

2.8 Conclusions

Our study shows that the appearance and disappearance of wellbore failures in image logs of the TCDP borehole are dependent on lithology. Along TCDP, there is ~70 MPa difference in compressive strength of rocks between the compliant sandstone and stiffer siltstone layers measured in the laboratory. Integrating these observations along with extended leak-off test results, we deduce that the post-earthquake in-situ horizontal stress magnitudes are lower in sandstone and higher in siltstone. Our inferred stress magnitudes fall within limits set by the frictional coefficient and capture the variability in stress states reported by previous studies in TCDP. Detailed borehole analysis also captures the relatively isotropic stress state within the

Chelungpu fault system. Our study highlights the importance of understanding spatial variations of stress at various scales.

We provide another snapshot of the stress state in the seismic cycle by calculating the state of stress before the Chi-Chi earthquake. Majority of the pre-earthquake stress magnitude data fall within the stress polygon, indicating subcritical stress state in the region where TCDP encountered the fault.

Acknowledgement

This research was funded by the National Science Foundation (EAR1727661). We thank Wei-Ting Lin for help in collecting samples and Kevin R. Cashman for support in preparing core plugs for laboratory testing. The authors would also like to thank the anonymous reviewers and editors for their constructive comments that helped to improve the manuscript.

References

Amadei, B., Swolfs, H. S., and Savage, W. Z. (1988). Gravity-induced stresses in stratified rock masses. *Rock Mechanics and Rock Engineering*, *21*(1), 1–20.

Barton, C. A., Zoback, M. D., and Burns, K. L. (1988). In-situ stress orientation and magnitude at the Fenton Geothermal Site, New Mexico, determined from wellbore breakouts. *Geophysical Research Letters*. https://doi.org/10.1029/GL015i005p00467

Bourne, S. J. (2003). Contrast of elastic properties between rock layers as a mechanism for the initiation and orientation of tensile failure under uniform remote compression. *Journal of Geophysical Research*. https://doi.org/10.1029/2001jb001725

Byerlee, J. (1978). Friction of rocks. *Pure and Applied Geophysics*.

https://doi.org/10.1007/BF00876528

Chan, C. H., Hsu, Y. J., and Wu, Y. M. (2012). Possible stress states adjacent to the rupture zone of the 1999 Chi-Chi, Taiwan, earthquake. *Tectonophysics*. https://doi.org/10.1016/j.tecto.2012.03.031

Chen, C. W. (2005). *The study of the mechanical characteristics from the host rock of the Chelungpu Fault*. MS, Thesis, 169 p, Natl. Taiwan Univ., Taipei.

Day-Lewis, A., Zoback, M., and Hickman, S. (2010). Scale-invariant stress orientations and seismicity rates near the San Andreas Fault. *Geophysical Research Letters*. https://doi.org/10.1029/2010GL045025

Evans, K. F., Engelder, T., and Plumb, R. A. (1989), Appalachian Stress Study: 1. A detailed description of in situ stress variations in Devonian shales of the Appalachian Plateau, *J. Geophys. Res.*, 94(B6), 7129– 7154, doi:10.1029/JB094iB06p07129.

Evans, K. F., Oertel, G., and Engelder, T. (1989), Appalachian Stress Study: 2. Analysis of Devonian shale core: Some implications for the nature of contemporary stress variations and Alleghanian Deformation in Devonian rocks, *J. Geophys. Res.*, 94(B6), 7155– 7170, doi:10.1029/JB094iB06p07155.

Fan, X., Chen, R., Lin, H., Lai, H., Zhang, C., and Zhao, Q. (2018). Cracking and failure in rock specimen containing combined flaw and hole under uniaxial compression. *Advances in Civil Engineering, 2018*.

Faulkner, D. R., T. M. Mitchell, D. Healy, and M. J. Heap (2006), Slip on 'weak' faults by the rotation of regional stress in the fracture damage zone, *Nature*, 444, 922– 925, doi:10.1038/nature05353

Gunzburger, Y., and Cornet, F. H. (2007). Rheological characterization of a sedimentary formation from a stress profile inversion. *Geophysical Journal International*, *168*(1), 402–418.

Gunzburger, Y., and Magnenet, V. (2014). Stress inversion and basement-cover stress transmission across weak layers in the Paris basin, France. *Tectonophysics*. https://doi.org/10.1016/j.tecto.2014.01.016

Haimson, B., Lin, W., Oku, H., Hung, J. H., and Song, S. R. (2010). Integrating borehole-breakout dimensions, strength criteria, and leak-off test results, to constrain the state of stress across the Chelungpu Fault, Taiwan. *Tectonophysics*, *482*(1–4), 65–72. https://doi.org/10.1016/j.tecto.2009.05.016

Hassan, M., Hossin, A. and Combaz, A. (1976). Fundamentals of the differential gamma ray log-interpretation technique. In *SPWLA 17th Annual Logging Symposium*. OnePetro.

Ho, C. S. (1986). A synthesis of the geologic evolution of Taiwan. *Tectonophysics*, *125*(1–3), 1–16.

Hoek, E., and Brown, E. T. (1980). Empirical strength criterion for rock masses. *Journal of the Geotechnical Engineering Division*, *106*(9), 1013–1035.

Hung, J. H., Ma, K. F., Wang, C. Y., Ito, H., Lin, W., and Yeh, E. C. (2009). Subsurface structure, physical properties, fault-zone characteristics and stress state in scientific drill holes of Taiwan Chelungpu Fault Drilling Project. *Tectonophysics*. https://doi.org/10.1016/j.tecto.2007.11.014

Ji, C., Helmberger, D. V., Song, T. R. A., Ma, K. F., and Wald, D. J. (2001). Slip distribution and tectonic implication of the 1999 Chi-Chi, Taiwan, earthquake. *Geophysical Research*

Letters. https://doi.org/10.1029/2001GL013225

Ji, C., D. V. Helmberger, D. J. Wald, and K.-F. Ma (2003), Slip history and dynamic implications of the 1999 Chi-Chi, Taiwan, earthquake, *J. Geophys. Res.*, 108(B9), 2412, doi:10.1029/2002JB001764.

Johnson, K. M., Hsu, Y. J., Segall, P., and Yu, S. B. (2001). Fault geometry and slip distribution of the 1999 Chi-Chi, Taiwan earthquake image from inversion of GPS data. *Geophysical Research Letters*. https://doi.org/10.1029/2000GL012761

Kanamori, H., and Brodsky, E. E. (2004). The physics of earthquakes. *Reports on Progress in Physics*. https://doi.org/10.1088/0034-4885/67/8/R03

Kano, Y., Mori, J., Fujio, R., Ito, H., Yanagidani, T., Nakao, S., and Ma, K. F. (2006). Heat signature on the Chelungpu fault associated with the 1999 Chi-Chi, Taiwan earthquake. *Geophysical Research Letters*. https://doi.org/10.1029/2006GL026733

Kirsch, C. (1898). Die theorie der elastizitat und die bedurfnisse der festigkeitslehre. *Zeitschrift Des Vereines Deutscher Ingenieure*, *42*, 797–807.

Kuo, L. W., Song, S. R., Yeh E. C., and Chen H. F. (2009). Clay mineral anomalies in the fault zone of the Chelungpu Fault, Taiwan, and their implications, *Geophys. Res. Lett*., 36, L18306, doi:10.1029/2009GL039269.

Lee, H., Ong, S. H., Azeemuddin, M., and Goodman, H. (2012). A wellbore stability model for formations with anisotropic rock strengths. *Journal of Petroleum Science and Engineering*, *96*, 109–119.

Lin, W., Yeh, E. C., Ito, H., Hung, J. H., Hirono, T., Soh, W., et al. (2007). Current stress state

and principal stress rotations in the vicinity of the Chelungpu fault induced by the 1999 Chi-Chi, Taiwan, earthquake. *Geophysical Research Letters*. https://doi.org/10.1029/2007GL030515

Lin, W., Conin, M., Moore, J. C., Chester, F. M., Nakamura, Y., Mori, J. J., et al. (2013). Stress state in the largest displacement area of the 2011 Tohoku-Oki earthquake. *Science*. https://doi.org/10.1126/science.1229379

Ma, K. F., C. T. Lee, Y. B. Tsai, T. C. Shin, and J. Mori (1999), The Chi-Chi Taiwan earthquake: Large surface displacements on inland thrust fault, *Eos Trans. AGU*, 80(50), 605, 611.

Ma, K. F., Mori, J., Lee, S. J., and Yu, S. B. (2001). Spatial and temporal distribution of slip for the 1999 Chi-Chi, Taiwan, earthquake. *Bulletin of the Seismological Society of America*. https://doi.org/10.1785/0120000728

Ma, K.-F., Brodsky, E. E., Mori, J., Ji, C., Song, T.-R. A., and Kanamori, H. (2003), Evidence for fault lubrication during the 1999 Chi-Chi, Taiwan, earthquake (Mw7.6), *Geophys. Res. Lett.*, 30, 1244, doi:10.1029/2002GL015380, 5.

Ma, K.-F., Y.-Y. Lin, S.-J. Lee, J. Mori, and E. E. Brodsky (2012), Isotropic events observed with a borehole array in the Chelungpu fault zone, Taiwan, *Science*, 337(459), 459–463, doi:10.1126/science.1222119.

McDonald, W. J. (1976). *Steady-state and transient wellbore temperatures during drilling*. Department of Energy, Office of Energy Technology, Division of Geothermal~….

Melan, E. (1932). Der Spannungszustand der durch eine Einzelkraft im Innern beanspruchten Halbscheibe. *ZAMM-Journal of Applied Mathematics and Mechanics/Zeitschrift Für*

Angewandte Mathematik Und Mechanik, *12*(6), 343–346.

Moos, D., and Zoback, M. D. (1990). Utilization of observations of well bore failure to constrain the orientation and magnitude of crustal stresses: Application to continental, Deep Sea Drilling Project, and Ocean Drilling Program boreholes. *Journal of Geophysical Research: Solid Earth*, *95*(B6), 9305–9325. https://doi.org/https://doi.org/10.1029/JB095iB06p09305

Noda, H., and Lapusta, N. (2013). Stable creeping fault segments can become destructive as a result of dynamic weakening. *Nature*, *493*(7433), 518–521.

Oku, H., Haimson, B., and Song, S. R. (2007). True triaxial strength and deformability of the siltstone overlying the Chelungpu fault (Chi-Chi earthquake), Taiwan. *Geophysical Research Letters*. https://doi.org/10.1029/2007GL029601

Peska, P., and Zoback, M. D. (1995). Observations of borehole breakouts and tensile wall-fractures in deviated boreholes: A technique to constrain in situ stress and rock strength. In *The 35th US Symposium on Rock Mechanics (USRMS)*.

Plumb, R. A., Evans, K. F., and Engelder, T. (1991), Geophysical log responses and their correlation with bed-to-bed stress contrasts in Paleozoic rocks, Appalachian Plateau, New York, *J. Geophys. Res*., 96(B9), 14509– 14528, doi:10.1029/91JB00896.

Segall, P. (2010). *Earthquake and volcano deformation*. Princeton University Press.

Segall, P., and Pollard, D. D. (1980). Mechanics of discontinuous faults. *Journal of Geophysical Research: Solid Earth*, *85*(B8), 4337–4350.

Shamir, G., and Zoback, M. D. (1992). Stress orientation profile to 3.5 km depth near the San Andreas Fault at Cajon Pass, California. *Journal of Geophysical Research*.

https://doi.org/10.1029/91JB02959

Sheng-Rong, S., Li-Wei, K., Yeh, E.-C., Chien-Ying, W., Hung, J.-H., and Kuo-Fong, M. (2007). Characteristics of the lithology, fault-related rocks and fault zone structures in TCDP Hole-A. *TAO: Terrestrial, Atmospheric and Oceanic Sciences*, *18*(2), 243.

Sibson, R. H. (1985). Stopping of earthquake ruptures at dilational fault jogs. *Nature*, *316*(6025), 248–251.

Sone, H., and Zoback, M. D. (2013). Mechanical properties of shale-gas reservoir rocks — Part 1: Static and dynamic elastic properties and anisotropy. *Geophysics*. https://doi.org/10.1190/geo2013-0050.1

Sone, H., and Zoback, M. D. (2014a). Time-dependent deformation of shale gas reservoir rocks and its long-term effect on the in-situ state of stress. *International Journal of Rock Mechanics and Mining Sciences*. https://doi.org/10.1016/j.ijrmms.2014.04.002

Sone, H., and Zoback, M. D. (2014b). Viscous relaxation model for predicting least principal stress magnitudes in sedimentary rocks. *Journal of Petroleum Science and Engineering*. https://doi.org/10.1016/j.petrol.2014.09.022

Sone, H., Noda, H., and Shimamoto, T. (2007). The coseismic fault weakening processes inferred from frictional and transport properties of fault rocks, TCDP. *Scientific Drilling*. https://doi.org/10.2204/iodp.sd.s01.06.2007

Tanikawa, W., and Shimamoto, T. (2009). Comparison of Klinkenberg-corrected gas permeability and water permeability in sedimentary rocks. *International Journal of Rock Mechanics and Mining Sciences*, *46*(2), 229–238.

Terzaghi, K., and Richart, F. E. (1952). Stress in rock around cavities. *Géotechnique*, *3*, 57–99.

Valley, B., and Evans, K. F. (2019). Stress magnitudes in the Basel enhanced geothermal system. *International Journal of Rock Mechanics and Mining Sciences*, *118*, 1–20.

Warpinski, N. R., and Teufel, L. W. (1989). In-situ stresses in low-permeability, nonmarine rocks. *Journal of Petroleum Technology*, *41*(04), 405–414.

Wu, H. Y., Ma, K. F., Zoback, M., Boness, N., Ito, H., Hung, J. H., and Hickman, S. (2007). Stress orientations of Taiwan Chelungpu-Fault Drilling Project (TCDP) hole-A as observed from geophysical logs. *Geophysical Research Letters*. https://doi.org/10.1029/2006GL028050

Yabe, Y., Song, S.-R., and Wang, C.-Y. (2008). In-situ stress at the northern portion of the Chelungpu fault, Taiwan, estimated on boring cores recovered from a 2-km-deep hole of TCDP. *Earth, Planets and Space*, *60*(8), 809–819.

Yeh, E. C., Sone, H., Nakaya, T., Ian, K. H., Song, S. R., Hung, J. H., et al. (2007). Core description and characteristics of fault zones from Hole-A of the Taiwan Chelungpu-Fault Drilling Project. *Terrestrial, Atmospheric and Oceanic Sciences*. https://doi.org/10.3319/TAO.2007.18.2.327(TCDP)

Yu, S.-B., Kuo, L.-C., Hsu, Y.-J., Su, H.-H., Liu, C.-C., Hou, C.-S., et al. (2001). Preseismic deformation and coseismic displacements associated with the 1999 Chi-Chi, Taiwan, earthquake. *Bulletin of the Seismological Society of America*, *91*(5), 995–1012.

Yu, S.-B., Hsu, Y.-J., Kuo, L.-C., Chen, H.-Y., and Liu, C.-C. (2003). GPS measurement of postseismic deformation following the 1999 Chi-Chi, Taiwan, earthquake. *Journal of Geophysical Research: Solid Earth*, *108*(B11).

Zhang, L., Wu, J. C., Ge, L. L., Ding, X. L., and Chen, Y. L. (2008). Determining fault slip distribution of the Chi-Chi Taiwan earthquake with GPS and InSAR data using triangular dislocation elements. *Journal of Geodynamics*. https://doi.org/10.1016/j.jog.2007.10.003

Zhang, Y., and Zhang, J. (2017). Lithology-dependent minimum horizontal stress and in-situ stress estimate. *Tectonophysics*. https://doi.org/10.1016/j.tecto.2017.03.002

Zoback, M. D., Barton, C. A., Brudy, M., Castillo, D. A., Finkbeiner, T., Grollimund, B. R., et al. (2003). Determination of stress orientation and magnitude in deep wells. *International Journal of Rock Mechanics and Mining Sciences*, *40*(7–8), 1049–1076. https://doi.org/10.1016/j.ijrmms.2003.07.001

Zoback, M. (2010). Reservoir Geomechanics, Cambridge Univ. Press, Cambridge, U. K.

2.9 Appendix

2.9.1 Experimental Procedure and Data

We prepared cylindrical plugs of TCDP rocks from cores acquired from the drilling project. We extracted 1” diameter plugs with a coring machine. Then the ends of the specimen are cut with a precision saw so that the length of the samples are 2” and the ends of the specimens are parallel to within 0.01 mm. This protocol follows the ISRM suggested methods. Testing is done in a servo-controlled triaxial apparatus and axial load is applied until the peak stress is reached. The peak stress is recorded as the Uniaxial Compressive Strength (UCS).

Table 2.S1. Summary of uniaxial compressive strength tests conducted for this study

Sample	Hole	UCS (MPa)	Vp log (km/s)	Starting Depth (m)	Ending Depth (m)	Loading Direction
UCS_A1	B	25.5	3.82	1183.09	1183.28	Parallel to borehole
UCS_A2	B	29.9	3.82	1183.09	1183.28	Parallel to borehole
UCS_A3	B	30.4	3.82	1183.09	1183.28	Parallel to borehole

UCS_A4	B	32.1	3.82	1183.09	1183.28	Parallel to borehole
UCS_A5	B	24.8	3.82	1183.09	1183.28	Parallel to borehole
UCS_B2	A	76.4	4.235	1031.06	1032.07	Parallel to borehole
UCS_C1	A	66.2	4.05	746.5	746.8	Parallel to borehole
UCS_C2	A	50.4	4.05	746.5	746.8	Perpendicular to borehole

We prepared disks 1” in diameter and ~ 0.5” in thickness to measure the Brazilian tensile strength of the rocks. The rock is loaded by two opposing metal platens which applies diametrical load from the periphery of the cylinder to induce tensile stresses within the specimen, leading to failure (standard ISRM suggested method for tensile testing).

Table 2.S2. Summary of tensile strength measurements conducted for this study

Sample	Hole	BTS (MPa)	Depth (m)	Loading Direction
BTS_D1	B	0.45	811.6	Parallel to borehole
BTS_D2	B	0.55	811.6	Parallel to borehole
BTS_A1	B	1.4	1183	Parallel to borehole
BTS_A2	B	2.3	1183	Parallel to borehole
BTS_A3	B	1.8	1183	Parallel to borehole
BTS_A4	B	1.3	1183	Parallel to borehole
BTS_C1	B	4.0	746.7	Parallel to borehole
BTS_C2	B	4.8	746.7	Parallel to borehole
BTS_B1	B	8.0	1033	Parallel to borehole
BTS_B2	B	7.0	1033	Parallel to borehole

2.9.2 Derivation of change in horizontal stress magnitude for a layered media undergoing uniform elastic deformation

We describe here the potential relationship between horizontal stress components and elastic properties for a layered media strained by tectonic loading. We visualize a rectangular block oriented parallel to the axes of a cartesian coordinate system, where the x, y, and z axes denotes East, North, and Down directions. The block is assumed to comprise of multiple layers oriented perpendicular to the z axis with each layer possessing different elastic properties. Next, we assume

that the layered media is loaded in the East-West (x) direction by uniform elastic deformation due to tectonic loading. As the block undergoes uniform elastic strain in the x direction, the stress magnitudes change in the x, y and z directions. The linear relationship between the change in strain and stress components within a layer due to this tectonic deformation can be described following the Hooke's law as:

$$\Delta e_{xx} = 1/E\ (\Delta\sigma_{xx} - v\ (\Delta\sigma_{yy} + \Delta\sigma_{zz})) \quad \text{(i)}$$

$$\Delta e_{yy} = 1/E\ (\Delta\sigma_{yy} - v\ (\Delta\sigma_{xx} + \Delta\sigma_{zz})) \quad \text{(ii)}$$

$$\Delta e_{zz} = 1/E\ (\Delta\sigma_{zz} - v\ (\Delta\sigma_{yy} + \Delta\sigma_{xx})) \quad \text{(iii)}$$

where Δe_{xx}, Δe_{yy} and Δe_{zz} are the strain changes in the x, y and z directions, respectively, $\Delta\sigma_{xx}$, $\Delta\sigma_{yy}$ and $\Delta\sigma_{zz}$ are the stress changes in the x, y and z directions, respectively. E is the Young's modulus and v is the Poisson ratio within the layer of consideration. In a layered media, E and v are different for each layer, which determines the change in magnitude of strain for each layer.

We apply two boundary conditions to solve the system of three equations (Eq. i-iii).

1. As the earth's surface is a free surface, we assume no stress change in the vertical direction but finite expansion in the vertical direction. That suggests $\Delta\sigma_{zz} = 0$; $\Delta e_{zz} \neq 0$.
2. We assume the body to be extending infinitely in the y direction, therefore there is no displacement occurring in the y direction, or $\Delta e_{yy} = 0$.

Applying these boundary conditions into Eq. (ii), we get:

$$\Delta\sigma_{yy} = v\ \Delta\sigma_{xx} \quad \text{(iv)}$$

This equation suggests that the horizontal stress change in the direction normal to the tectonic loading is the stress change in the direction of the tectonic load multiplied by the Poisson ratio. Applying the boundary conditions and Eq (iv) to Eq (i) and (ii) yield:

$$\Delta\sigma_{xx} = \Delta e_{xx}\, E / (1-v^2) \quad (v)$$

$$\Delta\sigma_{yy} = -\Delta e_{xx}\, vE / (1-v^2) \quad (vi)$$

Assuming the maximum horizontal stress is in the direction of the tectonic loading, $S_{Hmax} = \sigma_{xx}$ and $S_{hmin} = \sigma_{yy}$. Therefore, if horizontal stresses arise from horizontal elastic loading alone, S_{hmin} will vary between layers proportionally against the variation in the combination of elastic properties, $vE / (1-v^2)$.

We note that these equations hold for a transversely isotropic, homogeneous medium where the Youngs modulus and Poisson ratio is assumed to be same in all directions. Additionally, it doesn't take into consideration the directional mismatch that may occur due to the 30° dip of bedding planes in the region with respect to the S_{hmin} plunge direction.

2.9.3 S_{hmin} and S_{hmin} gradient obtained from previous studies

Below we provide the S_{hmin} and S_{hmin} gradient values used for the correlations between S_{hmin} gradient- Gamma Ray and S_{hmin} gradient- $vE / (1-v^2)$ in Section 2.5.1 of the manuscript.

Table 2.S3. Summary of S_{hmin} observed in previous literature

Literature	Hole	Depth [m]	S_{hmin} [MPa]	S_{hmin} gradient [MPa/m]	Procedure
Haimson et al. 2010	B	1085.0 1279.6	23.7 29.8	0.0222 0.0236	Hydraulic Fracturing
Hung et al. 2009	B	1019.5 1085.0 1179.0 1279.6	16.3 23.7 16.2 19.6	0.0163 0.0222 0.0140 0.0156	Hydraulic fracturing

Yabe et al. 2008	A	739.0 927.0 1082.0 1122.0 1316.0	14.2 15.2 13.7 19.1 12.9	0.0192 0.0163 0.0126 0.0170 0.0098	Stress memory tests
Lin et al. 2007	A	1120.0	19.7	0.0176	Anelastic strain recovery

2.9.4 Stress polygon obtained using elastic properties

As shown in section 2.9.2, we consider the effect of elastic tectonic loading on a layered media to obtain a relationship between S_{hmin} and $vE / (1-v^2)$. We obtain the elastic properties from sonic log to calculate $vE / (1-v^2)$ and correlate $vE / (1-v^2)$ with S_{hmin} gradient (in section 2.9.3) (Figure 2.7a). The corresponding stress polygon obtained from this correlation is shown in Figure 2.S1. While the scatter in stress is slightly different from Figure 2.12, there is overall agreement with past stress measurements and the conclusions of our study does not change.

Inability of the elastic properties to fully describe the past stress measurements, especially the results by Haimson et al., (2010) also suggests the need to consider additional factors that affect the S_{hmin}. One such factor we emphasize in this paper is the ductility of clay-rich rocks, which can relax the differential stress accumulation in rocks over time. To address both elastic and ductile deformation of the rocks, we use S_{hmin} gradient- Gamma Ray relationship in the main manuscript and the result obtained from S_{hmin} gradient- $vE / (1-v^2)$ is presented here only for comparison.

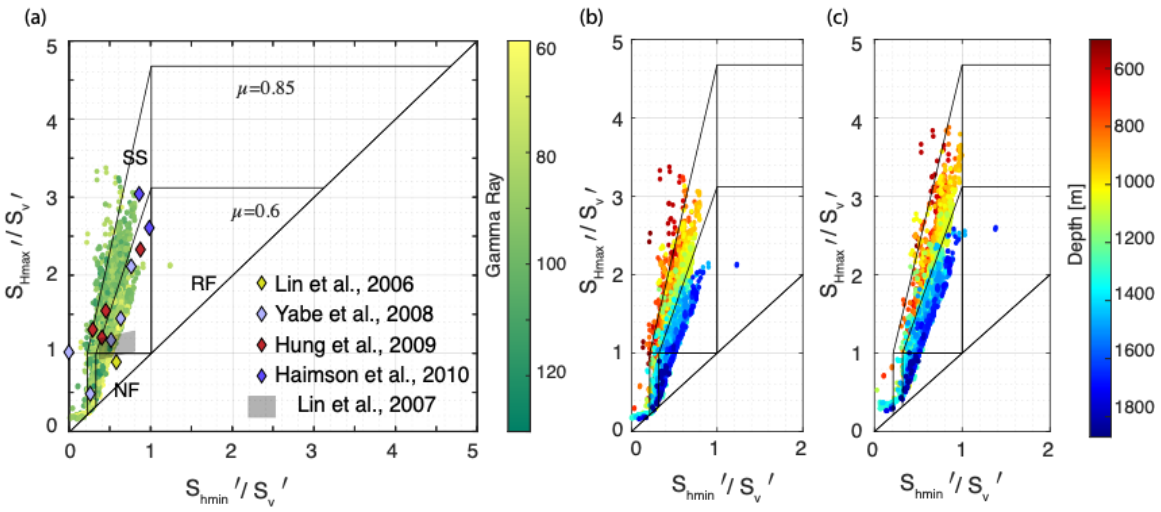

Figure 2.S1. Calculated post and pre-earthquake effective horizontal stress magnitudes normalized with effective vertical stress plotted with the stress polygon. S_{hmin} magnitude is estimated from $vE/(1-v^2)$ to calculate post-earthquake stress magnitudes. a) Post earthquake stress estimates color coded by gamma ray, b) post-earthquake stress estimates color coded by borehole depth, and c) pre-earthquake stress magnitudes color coded by borehole depth.

2.9.5 Equations and model parameters for edge dislocation model

Equations presented here follows derivations presented in Segall (2010). The horizontal and vertical displacement fields due to a single dip-slip edge dislocation is described as:

$$u_1 = \frac{s_1}{\pi(1-v)}\left\{\frac{(1-v)}{2}(\theta_2-\theta_1) + \frac{x_1(x_2-\xi_2)}{4r_1^2} - \frac{x_1[x_2-(3-4v)\xi_2]}{4r_2^2} + \frac{\xi_2 x_2 x_1(x_2+\xi_2)}{r_2^4}\right\} +$$

$$\frac{s_2}{\pi(1-v)}\left\{\frac{(1-2v)}{2}\log({}^{r_2}/_{r_1}) - \frac{(x_2-\xi_2)^2}{4r_1^2} + \frac{[x_2^2+\xi_2^2-4(1-v)\xi_2(x_2+\xi_2)]}{4r_2^2} + \frac{x_2\xi_2(x_2+\xi_2)^2}{r_2^4}\right\} \quad \text{(vii)}$$

$$u_2 = \frac{s_1}{\pi(1-v)}\left\{\frac{(1-2v)}{2}\log({}^{r_2}/_{r_1}) + \frac{(x_2-\xi_2)^2}{4r_1^2} - \frac{[(x_2+\xi_2)^2-2\xi_2^2-2(1-2v)\xi_2(x_2+\xi_2)]}{4r_2^2} + \frac{x_2\xi_2(x_2+\xi_2)^2}{r_2^4}\right\} +$$

$$\frac{s_2}{\pi(1-v)}\left\{\frac{(1-v)}{2}(\theta_2-\theta_1) + \frac{x_1(x_2-\xi_2)}{4r_1^2} - \frac{x_1[x_2-(3-4v)\xi_2]}{4r_2^2} + \frac{\xi_2 x_2 x_1(x_2+\xi_2)}{r_2^4}\right\} \quad \text{(viii)}$$

where coordinates x_1 and x_2 are defined in the horizontal and vertical directions, s_1 and s_2 are fault slip components in the horizontal and vertical directions, ξ_1 and ξ_2 are x_1 and x_2 coordinates of the buried edge dislocation, respectively. The only material property in the displacement equations (vii) and (viii) is the Poisson ratio (v). We calculate Poisson ratio from P and S wave velocity logs, where the average Poisson ratio along TCDP was about 0.33.

The remaining variables are defined in relation to the position of two edge dislocations inherent in this solution. Because one full space solution for an edge dislocation does not capture the presence of a traction-free plane at the earth's surface, Segall (2010) adds contribution from (1) the subsurface dislocation and (2) an imaginary dislocation above the surface mirror image about the free surface ($x_2 = 0$) but with an opposite sign, to ensure that the stresses due to the subsurface dislocation are canceled out at the free surface. Eq. (vii) and (viii) already incorporate contributions from the buried dislocation and its corresponding image (dislocation). r_1 and r_2 are distances between the observation points where the displacements are calculated and the buried and image dislocation, respectively (Eq. ix and x).

$$r_1 = \sqrt{(x_1 - \xi_1)^2 + (x_2 - \xi_2)^2} \tag{ix}$$

$$r_2 = \sqrt{(x_1 - \xi_1)^2 + (x_2 + \xi_2)^2} \tag{x}$$

θ_1 in Eq. (vii) and (viii) is the angle between the fault plane (line in 2D) and the line connecting the dislocation to the observation point (Eq. xi). Similarly, θ_2 is the angle between the imaginary fault plane in the air and the line connecting the image dislocation to the observation point (Eq. xiv).

$$\theta_1 = \tan^{-1}\frac{x_1 - \xi_1}{x_2 - \xi_2} - (90° + \phi) \tag{xi}$$

$$\theta_2 = \tan^{-1}\frac{x_1-\xi_1}{x_2+\xi_2} - (90° - \phi) \quad \text{(xii)}$$

where ϕ is the dip of the fault plane.

Eq. (xi) and (xii) solves the displacement field for a pair of buried and image dislocation whose fault plane extends infinitely into the earth. Thus, two solutions are added, one with the edge dislocation on the free surface and the other with the edge dislocation at the down-dip edge of the fault, to get the displacement field due to a confined fault. The displacement caused by a 30° dipping fault is shown by a quiver plot (Figure 2.11a).

Table 2.S4. Summary of model parameters

Model Parameters	Values
Shear Modulus (G)	10 GPa
Poisson ratio (v)	0.33
[c1 c2]: coordinate of edge dislocation in x1-x2 coordinate system	[13, -7] km
Fault dip	30°
Amount of slip	8 m

2.9.6 GPS surface displacements close to the TCDP boreholes

Taiwan Chelungpu Fault drilling project drilled boreholes at 24.20 latitude and 120.75 Longitude. We use GPS surface displacement data from stations located near the TCDP boreholes for the edge dislocation model, as reported by Yu et al. (2001). In Table S5, *De* and *Du* denote the east and upward components of displacement, respectively.

Table 2.S5. Coseismic surface displacements near the TCDP boreholes.

Station Number	Latitude	Longitude	*De* [m]	*Du* [m]
AF25	24.125	120.744	-4.007±0.002	4.173±0.011
AF27	24.086	120.744	-4.280±0.005	3.505±0.023

M314	24.105	120.742	-5.127±0.009	1.968±0.025
M324	24.222	120.735	-3.423±0.006	3.972±0.023
M345	24.141	120.744	-6.057±0.011	0.910±0.033
Average	-	-	4.579	2.906

CHAPTER 3

Evidence of stress relaxation in the damage zone of the Chelungpu fault system

Abstract

High fracture density in fault damage zones can promote sliding of fracture surfaces and grains past each other and reduction of fracture volume. These processes in fault damage zones can accommodate considerable bulk creep deformation. This study provides potential evidence of time-dependent bulk deformation of the damage zone rocks in the Chelungpu fault system, which would progressively alter both the stress state around faults and shear stress on faults

during the interseismic period. We characterized the damage zone in the Chelungpu fault system by documenting a combination of fracture density increase observed in cores, reduction in sonic log velocity, and increase in caliper-measured borehole width. Comparing the damage zones of the three faults in the Chelungpu fault system, we observed that the youngest fault damage zone showed pronounced sonic velocity reduction even though fracture density is the same for all three fault zones, which is consistent with the shorter healing time of the youngest fault. Caliper log data also showed a time-dependent enlargement of the borehole wall at the youngest fault damage zone. We also observed that the damage zone records lower differential stress than the surrounding host rock. A relatively isotropic stress state before the 1999 Chi-Chi earthquake suggests that stress magnitudes were far from critical in the damage zone. We use an elastic plane strain model with fault-parallel layers of varying elastic properties to show that stress rotation due to the reduced elastic stiffness of the damage zones is not sufficient to explain their low differential stress magnitude. Therefore, we suggest that the low differential stress in the Chelungpu fault damage zone can be attributed to the long-term shear stress relaxation due to ductile deformation of damage-zone rocks.

3.1 Introduction

A fault system is broadly comprised of a fault core, flanking damage zone and surrounding host/country rock. The fault core is a narrow, commonly mms-cms wide zone which accommodates plate motion by localized slip during slow-slip events, aseismic creep and/or earthquakes (Chester et al., 1993; Scholz, 2019; Shipton and Cowie, 2001). The surrounding fault damage zone is characterized by high fracture density (Chester and Logan, 1986), which lowers the stiffness of fault damage zone rocks (Faulkner et al., 2006) as compared to the intact host rock. Such compliant damage zones can cause enhanced interseismic shear strain rates as observed in

geodetic studies, for instance along the San Andreas and San Jacinto faults (Lindsey et al., 2014; Materna and Bürgmann, 2016).

The magnitude of off-fault strain accumulation has been inferred from the discrepancy between geologic slip rate, geodetic slip rate and kinematic block models. Kinematic modeling by Bird (2009) suggested that 1/3 of the plate motion along the Pacific-North American plate boundary in California occurs as permanent distributed off-fault deformation. Johnson (2013) also showed that kinematic models better fit geodetic velocities in Southern California when intra-block deformation was allowed, and such off-fault strain rates may constitute 28-33% of the total geodetic moment rate. InSAR derived surface displacement data have documented a slip deficit on faults during shallow earthquakes: Bam, Izmit, Hector Mine and Landers earthquakes (Fialko, 2006). The remainder of the slip has been attributed to inelastic and distributed off-fault deformation during the inter-seismic period (Fialko, 2006). These observations indicate that damage zone deformation may be taking place either in small hidden faults or as distributed rock deformation.

Since deformation may concentrate in damage zones and evidence of off-fault strain accumulation is found from various geodetic observations, we suggest that a substantial amount of interseismic off-fault tectonic deformation is accommodated in damage zones even where the fault plane itself is partially to fully locked. Damage zones likely deform by progressive sliding of fracture surfaces and time-dependent closure of fracture surfaces during the interseismic period (Meyer et al., 2021; Sone and Condon, 2017). Such off-fault strain accumulation in fault damage zones may progressively alter the damage zone stress state and in turn alter the shear stress magnitude on the fault plane (Sone and Uchide, 2016). We suggest that in the presence of a thick

damage zone, time-dependent damage zone deformation can lead to relaxation of the shear stress that would otherwise accumulate on a locked fault during the inter-seismic period.

In this paper, we report potential evidence of time-dependent off-fault distributed deformation in the Chelungpu fault system that ruptured during the Mw 7.3, 1999 Chi-Chi earthquake in Taiwan. We derive evidence from well logs and cores drilled across the Chelungpu fault system (as shown in the cross section of the fault system in Figure 3.4a). We further argue that the apparent near-isotropic stress state around the fault zone reflects time-dependent plastic deformation occurring in the damage zone.

3.2 Methods

TCDP drill core is suitable for this study because it cut fault damage zones that are likely at different stages in the seismic cycle. Moreover, core recovery of greater than 90%, high quality log data, and abundant literature already provide rich information about the rock type, rock properties and structures encountered in the Chelungpu fault system. The rock types in this area range from sand rich layers to silt rich layers, with intermediate lithologies like sandy siltstone, silty sandstone and bioturbated siltstone.

We characterized the damage zone in the Chelungpu fault system with the help of geophysical logs like caliper and sonic logs. A caliper log provides a continuous measure of borehole diameter with depth. During the TCDP, the logging operations used four arm calipers, where caliper readings from two perpendicular arms are averaged to provide borehole diameter information.-Differences between the bit size used during drilling (6 inches) and caliper readings imply enlargement of the borehole. Logging operators also collected the P wave and S wave velocity of the formation.

We integrated borehole failure observations, laboratory experiments, log data and hydraulic fracturing measurements to calculate the in-situ state of stress along the TCDP borehole (details in Talukdar et al., 2022). Talukdar et al. (2022) observed that both the locations of borehole failures and rock strength were dependent on lithology, underlining a lithologic control on in-situ stress magnitude. They also used the correlation between gamma ray log and minimum principal stress magnitudes measured by previous workers to estimate a profile of variations in minimum horizontal principal stress (S_{hmin}). They integrated compressive strength measurements with breakout width observations and the estimated S_{hmin} profile to calculate the maximum horizontal principal stress (S_{Hmax}). Using a near-continuous profile of in-situ post-earthquake S_{hmin} and S_{Hmax}, they utilized two-dimensional edge dislocation theory to calculate the coseismic principal stress change during the Chi-Chi earthquake. This calculated coseismic stress change was subtracted from the post-earthquake in-situ stress profile to estimate the pre-earthquake principal stress magnitudes (Talukdar et al., 2022).

3.3 Results

3.3.1 Depth range of damage zone

The Taiwan Chelungpu Drilling Project (TCDP) encountered three large faults in each borehole (Yeh et al., 2007; Sone et al., 2007). Hole A encountered faults at 1111, 1153 and 1222 m depths as shown by the horizontal gray lines in Figure 3.1a. Hole B was drilled further away from the fault surface rupture (Figure 3.4a), therefore, it encountered the same fault at slightly greater depths: 1134, 1194 and 1243 m (Hirono et al., 2007). We observe an increase in one of the caliper readings close to the faults in Hole A and Hole B (Figure 3.1a). We attribute this increase in size of one of the two calipers close to the faults to breakout growth in the fault damage zone. A similar observation has been made by Sahara et al. (2014), where borehole breakouts are seen

to deepen and expand in regions of high fracture density, leading to preferential increase in caliper reading in the direction of the breakout. Preferential increase in one caliper reading in the fault zone extends from 1080-1260 m (Figure 3.1a); this depth range is therefore considered to represent the location of the damage zone of the Chelungpu fault system.

The depth range over which seismic velocity reduction is observed in sonic logs highlights the extent of damage zone in the Chelungpu fault system. We observe that the elastic wave velocity is lower in fault zones present between 1080 and 1250 m (Figure 3.1b). The reduction in both P- and S- wave velocity is attributed to the presence of highly fractured zones, where greater velocity reduction in the hanging wall is possibly due to greater fracture damage near the surface (Ma, 2009). Similar asymmetric damage distribution, with more damage in the hanging wall, has been observed in other dip slip faults like the Nojima fault, Japan (Lin et al., 2007) and Wenchuan earthquake fault, China (Li et al., 2013).

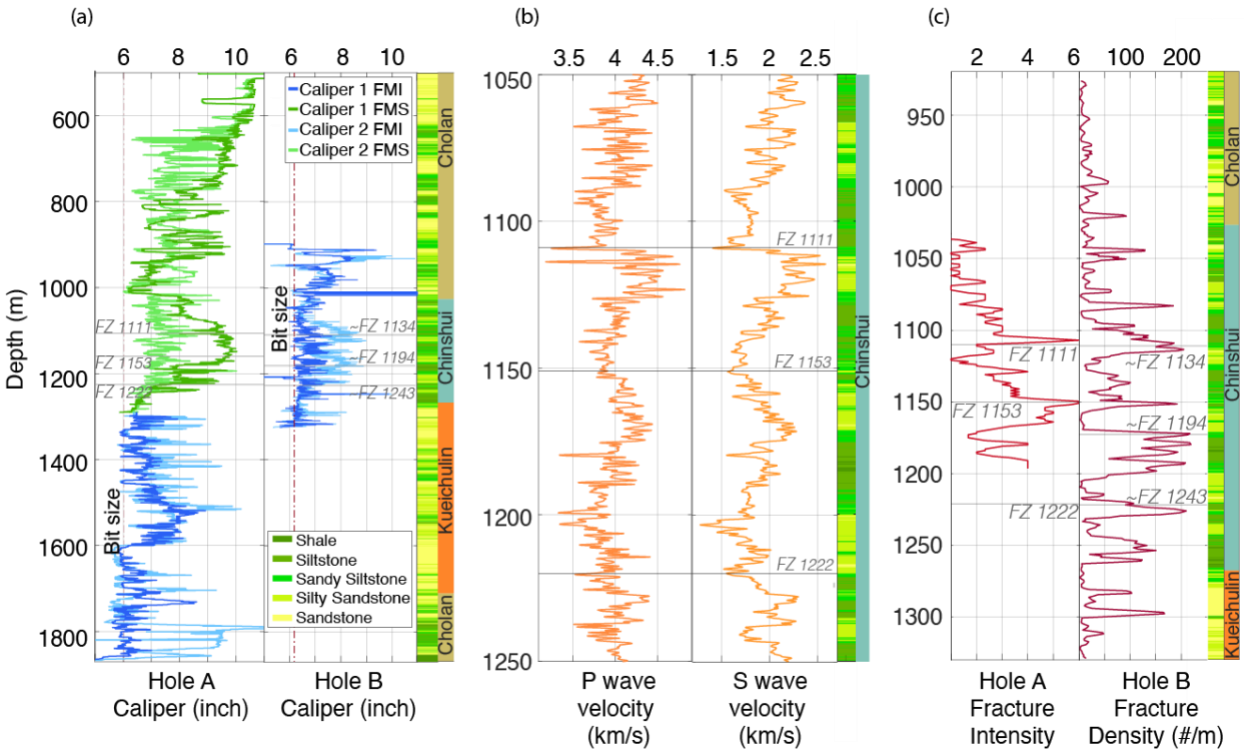

Figure 3.1. Data sets showing the extent of damage zones a) Caliper data in Hole A and B. Hole B log depth is shifted up by 22 m for comparison with Hole A data based on the lithology depth shift found in the previous chapter. Difference in caliper 1 and 2 indicates borehole enlargement at the fault damage zone. b) P and S wave velocity from Hole A sonic log. c) Fracture intensity (Hole A) and fracture density (Hole B) observed from drilled cores.

We counted visible fractures in Hole A and B cores acquired after drilling to characterize fracture density, i.e., the number of fractures per meter of core (Figure 3.1c). For Hole A, this is described in fracture intensity, an index between 0 and 7 designated based on the fracture density. Fracture intensity is defined in Sone et al. (2007) as shown in Appendix 3.6.1. The depth range of damage zone from 1080-1260 m shows an increase in fracture number (Figure 3.1c). The fracture number increases with proximity to faults.

3.3.2 Comparison between old and new fault damage zones

Previous studies show that the shallowest of the three faults is the youngest fault, which formed during the Chi-Chi earthquake (Ma et al., 2006). We observed that sonic velocity reduction is most prominent for the shallowest (or youngest) fault and least prominent in the deeper (or older) faults (Figure 3.1b). Likewise, if we compare the difference in caliper readings for the three fault zones in Figure 3.1a, the shallowest fault shows the highest difference between readings, but the difference in caliper readings is less for the deeper faults. The fracture density, however, is similar in all three fault zones. Equal fracture densities in all three fault zones combined with differences in seismic velocity reduction and caliper readings suggests there are more open and unhealed fractures in the damage zone of the younger fault which lowers the stiffness and strength of the damage zone rocks. Therefore we hypothesize that the pronounced velocity reduction in the shallowest fault records the shorter healing time of the youngest fault compared to the deeper and older faults.

3.3.3 Time-dependent borehole enlargement

Hole A logging took place during two drilling periods as shown in Figure 3.2a. The first period involved drilling from the surface down to 1300 m below surface. The second drilling period cut from 1300 m- 2000 m. After each drilling period, logging data were collected. Time of exposure is calculated from the day of drill bit penetration to the day of logging. Time of exposure of the shallower section (up to 1300 m), or first drilling period of Hole A, was more than the time of exposure of the deeper section, or second period (1300 -2000 m) (Figure 3.2b). Time of exposure of Hole B (drilled in a single period) was shorter than both drilling periods of Hole A.

Figure 3.2b shows that caliper measurements increase with exposure time during each run. Within each run, duration of exposure in the top part of the borehole is larger than the bottom because drilling was completed from top to bottom followed by logging. Caliper width is therefore larger in the shallower portion of the borehole as compared to the deeper portion, indicating time-dependent borehole enlargement which is possibly due to time-dependent deformation of the rocks exposed along the borehole. Time-dependent borehole enlargement can be caused by diffusion of high mud pressure into the formation (Paul and Zoback, 2008). Nonetheless, the difference between mud pressure and pore pressure in the TCDP borehole is considered to have been less than 1 MPa/km (Haimson et al., 2010; Hung et al., 2009), therefore it was not likely a major factor producing borehole enlargement in this setting.

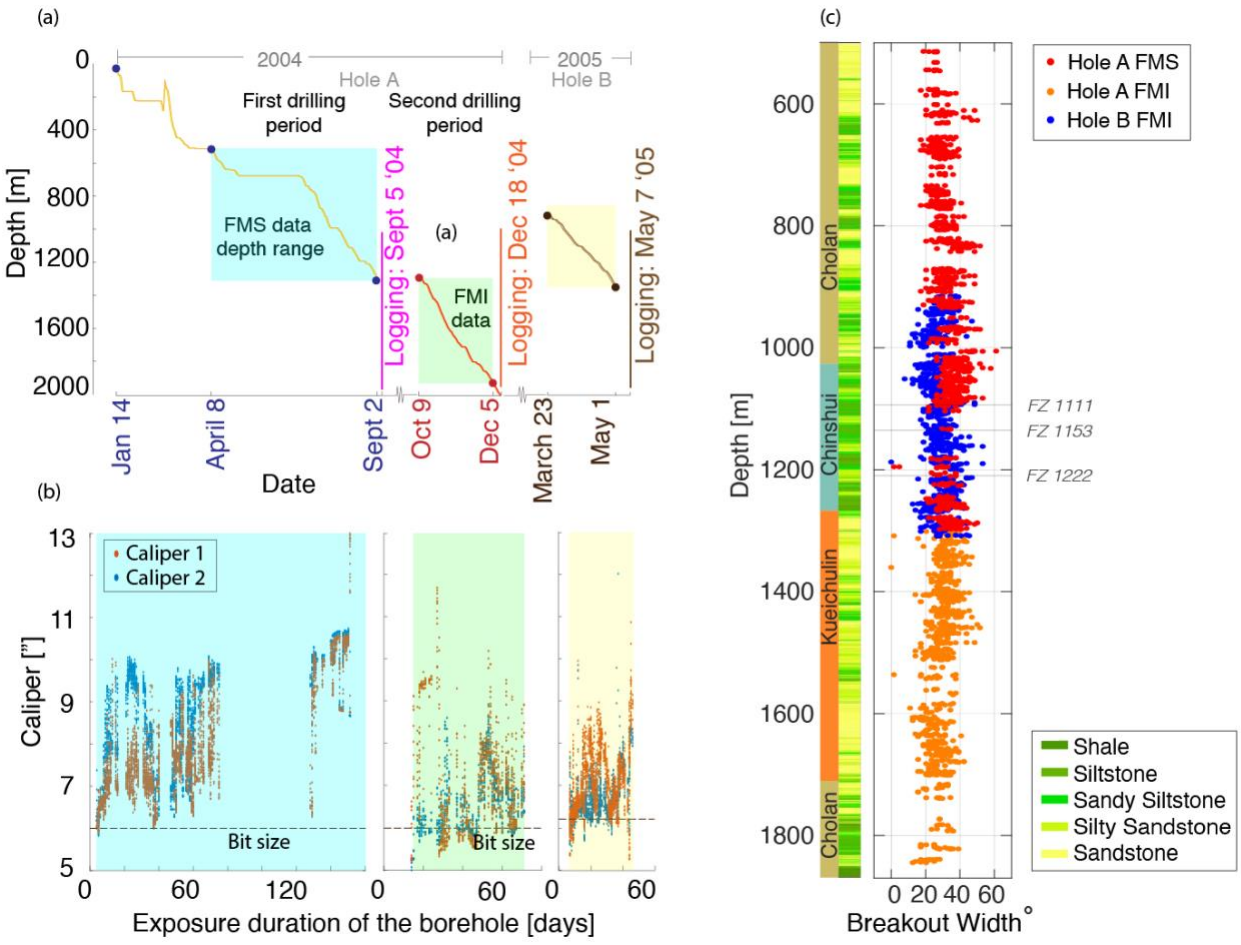

Figure 3.2. a) Depth reached by drilling plotted with date of drilling. b) Caliper log data plotted with exposure time of the borehole. c) Borehole breakout widths from image logs.

Similarly, we observe that Hole A breakout width (shown in red) is larger than Hole B breakout width (shown in blue) in the depth range of 1000- 1100 m; i.e., within the damage zone of FZ 1111 (Figure 3.2c). Boundary element models of successive stages of breakout extension have illustrated that breakout width remains constant after breakout initiation in a perfectly elastic medium (Crouch et al., 1983; Mastin, 1984). Zoback et al. (1985) note that breakout width grows in the earth's crust, as the rheology of the crust is not elastic but deforms with time. Time-dependent growth of breakout width has been observed in Auburn geothermal well, New York (Plumb and Hickman, 1985), Soultz geothermal field, France (Cornet et al., 2007) and Nankai

Trough drilling project, Japan (Moore et al., 2011). In the TCDP boreholes, we observe higher breakout width in Hole A than Hole B. The longer exposure time of Hole A may have resulted in more time-dependent deformation of the damaged rocks, leading to breakout growth and borehole enlargement over time.

3.3.4 State of stress in the fault damage zone

We plot the near-continuous profile of in-situ stress magnitudes following the 1999 Chi-Chi earthquake obtained from wellbore failure observations in Talukdar et al. (2022) (Figure 3.3a). We observe that the gradient of S_{Hmax} decreases at depths greater than 1000 m, as indicated by the dotted orange line showing a 45 MPa/km gradient. We also observe an increase in S_{hmin} with respect to the 10 MPa/km gradient line between 1080 and 1260 m. These changes in principal stress magnitudes between 1080 and 1260 m suggest lower differential stress magnitudes within the damage zone, especially compared to the hanging wall. The stress state along the borehole is also plotted in a normalized stress polygon in Figure 3.3b. We see that plots of pre-earthquake stress state mostly fall within frictional limits set by a typical rock friction coefficient of 0.6-0.85 (Byerlee, 1978), but the stress state in the Chelungpu fault damage zone (from 1080-1260 m) was close to isotropic state at $S_{hmin} = S_{Hmax} = S_v$ (Figure 3.3c).

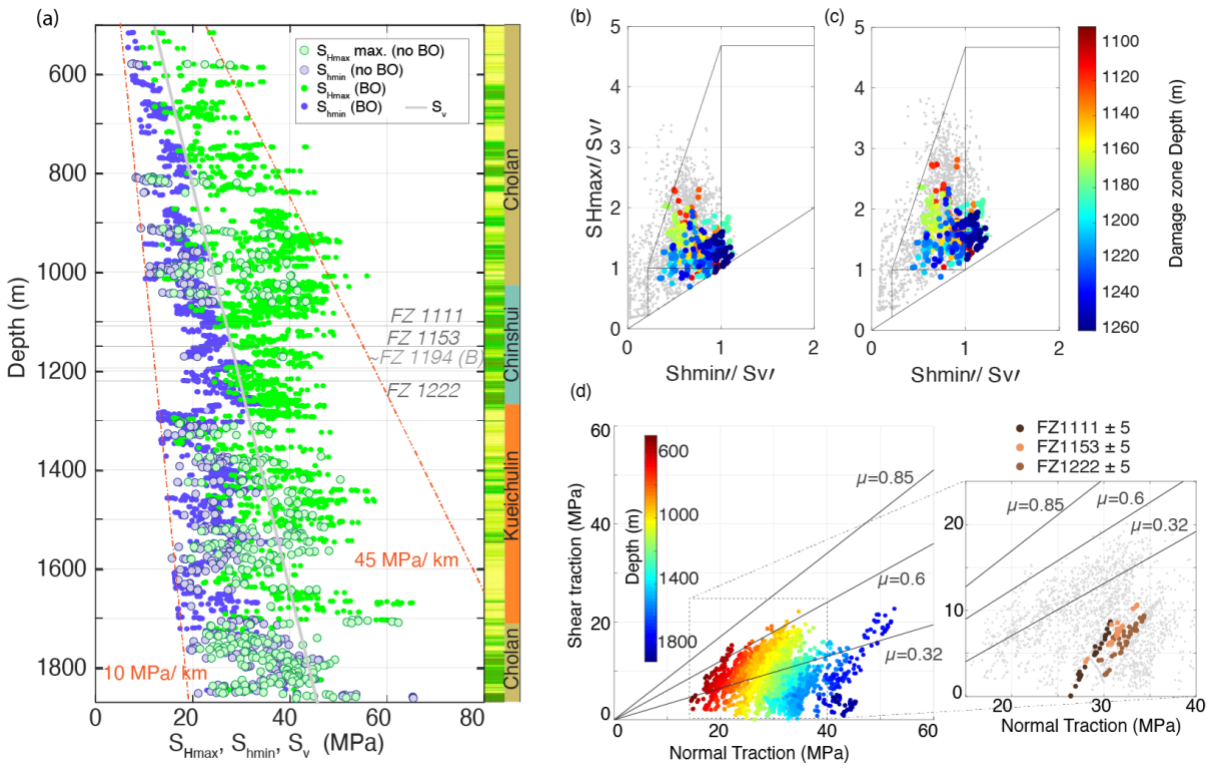

Figure 3.3. a) Variation in principal stress magnitudes S_{Hmax}, S_{hmin}, S_v and Pore fluid pressure (Pp) with depth. Two orange lines show gradient of 10 MPa/km and 45 MPa/km that highlight lower S_{Hmax} gradient and higher S_{hmin} gradient in the fault zone. b) Plot of effective in-situ horizontal stress magnitude normalized with respect to effective vertical stress in the damage zone, color coded by depth. c) Pre-earthquake stress polygon for the same section, color coded by depth. d) Plot of shear vs normal traction at every point where the principal stress magnitudes are calculated. Slip tendency in the fault zones (FZ, in plot to the right) is generally lower than the slip tendency in the entire section of the borehole. Slip tendency is also lower than typical Byerlee coefficient of 0.6 and 0.85, as well as the friction coefficient of 0.32, measured by Mizoguchi et al. (2008).

We also used pre-earthquake stress magnitudes to calculate shear and normal traction resolved on fractures and secondary fault planes, which are dominantly parallel to the primary slip plane of the Chi-Chi earthquake as seen from core observations and image logs (Yeh et al., 2007). The ratio of shear stress to normal stress (i.e., the slip tendency) along the entire borehole is again within typical friction coefficients of 0.6 and 0.85 (Figure 3.3d), but the slip tendency is much

lower in the damage zone within 5 meters of the fault cores (Figure 3.3e). Slip tendency of less than 0.25 close to the fault core is even lower than the measured frictional coefficent of fault gouge material recovered from Hole B fault zones (Mizoguchi et al., 2008). Note that these are best estimates of the pre-earthquake stress state. Therefore, unless the shear traction was released by previous fault slip and did not recover since, the low shear traction (below the frictional limit of gouge materials) is unusual to observe in such active fault zone systems.

3.4 Discussion

We propose that the current near-isotropic stress in the damage zone and inferred extremely low pre-earthquake shear traction on the fault plane is a consequence of interseismic deformation and stress relaxation that results from the mesoscopically ductile nature of highly fractured rocks in the damage zone (Sone and Uchide, 2016). Observations of fault healing and time-dependent borehole enlargement discussed above are all indicative of the slow time-dependent deformation that can occur within the damage zone over time. Laboratory experiments also suggest that rocks with damage exhibit some ductility due to the presence of microfractures (Meyer et al., 2021; Sone and Condon, 2017; Talukdar et al., 2021)

While we argue that the isotropic stress state recorded by the damage zone can be attributed to time-dependent stress relaxation which reduces the differential stress with time (Figure 3.3b, c), it is also known that the damage zone stress state can approach isotropic due to the increase in microcrack density and associated change in elastic stiffness with increasing proximity to the fault core (Faulkner et al., 2006). Damage zones are suggested to have higher Poisson's ratio and lower Young's Modulus with increasing micro-fractures (Figure 3.4b), leading to a local rotation in principal stress and lower differential stress in the fault zone, or a stress state closer to isotropic

state. We evaluate if such local change in elastic properties in the fault zone is responsible for the locally isotropic stress state observed around the Chelungpu fault in TCDP.

In TCDP, we observe a decrease in fracture density with distance from the fault core. Thus, we model the damage zone as fault parallel layers, each with lower Poisson's ratio and higher Young's modulus with distance from the fault (Figure 3.4b). We use the multilayer model by Casey (1980) to calculate the change in magnitude and direction of principal stresses due to the damage-induced changes in elastic properties upon entering a layer with different elastic properties. The multilayer model assumes constant strain along the slip direction and traction equilibrium along the interface between layers:

$$\sigma_{yy} = \sigma'_{yy} \qquad (3.1)$$

$$\tau_{xy} = \tau'_{xy} \qquad (3.2)$$

$$\varepsilon_{xx} = \varepsilon'_{xx} \qquad (3.3)$$

where *x* and *y* are parallel and perpendicular, respectively, to a 30° dipping fault in an East-West vertical profile containing the dip direction. σ, τ and ε indicate normal stress, shear stress and normal strain components, respectively within a layer. The apostrophe (') indicates the stress components in an adjacent layer.

Using the above boundary conditions (Equations 3.1, 3.2 and 3.3) and Hooke's Law, we can obtain σ, τ and ε magnitudes for the range of possible elastic properties contrast to calculate the corresponding possible range of S_{Hmax} and S_v in the fault-parallel layers (Figure 3.4c). The stress magnitude thus determined are dependent on the Young's modulus ratios (R_E = ratio of Young's modulus of damage zone to Young's modulus of host rock), ratio of Poisson's ratio (R_v = ratio of Poisson's ratio of damage zone to Poisson's ratio of host rock) and the absolute

magnitude of host rock Poisson's ratio (v_0). The stress magnitudes are independent of the absolute magnitude of Young's modulus though.

We assumed a far field stress magnitude of 50 MPa and 27 MPa for S_{Hmax} and S_v, respectively, based on our calculations of pre-earthquake in-situ stress magnitudes (Talukdar et al., 2022). The intermediate stress S_{hmin}, which obeys the plane strain boundary condition in this model, is not relevant to our discussion because it is the principal stresses in the vertical plane spanned by the x and y axes which are driving forces of the dip slip fault motion. Elastic properties are obtained from density and sonic logs. Poisson's ratio ranged from 0.25-0.35 whereas Young's Modulus ranged from 22 GPa to 32 GPa. These maximum and minimum values determine the R_E and R_v values considered in the calculation. The resultant stress magnitudes are plotted as four diamond polygons in Figure 3.4c, each corresponding to different R_E. Higher R_E yields lower S_{Hmax} and S_v. The maximum azimuthal change of Sv in the vicinity of the Chelungpu fault due to the contrast in elastic property across the fault damage zone is also less than 15° (Figure 3.4d).

To find the difference in principal stress magnitudes in the multilayer model given by the range of elastic properties, we computed the ratio of maximum shear stress ($(\sigma_1 - \sigma_2)/2$) to mean stress ($(\sigma_1 + \sigma_2)/2$) (Figure 3.4e). Since the state of stress is perfectly isotropic when ratio of maximum shear stress to mean stress is equal to 0, the magnitude of $(\sigma_1 - \sigma_2)/(\sigma_1 + \sigma_2)$ is a proxy for how much the stress state deviates from isotropic state. The magnitude of $(\sigma_1 - \sigma_2)/(\sigma_1 + \sigma_2)$ is lower at higher Young's modulus ratio. We then compare the $(\sigma_1 - \sigma_2)/(\sigma_1 + \sigma_2)$ ratio calculated from the elastic multilayer model, and the borehole observations. We find that the observed stress state in the damage zone is more isotropic than predicted from the elastic model.

Faulkner et al. (2006) observed a significant rotation of principal stress azimuth (from 80° to 40°) as the Poisson's ratio magnitude ranged from 0.25 in the host rock to 0.5 in the most damaged layer, which also led to lower differential stress magnitude. In this study, the range of Poisson ratio is 0.25 to 0.3, therefore there is less rotation of the principal stress direction and differential stress magnitude do not reduce drastically. The ratio of maximum shear stress and mean stress is higher than observed differential stress (Figure 3.4e). This suggests that elastic contrast cannot explain the low differential stress in the damage zone, highlighting the need to consider inelastic and time-dependent deformation of the damage zone to explain the stress observations.

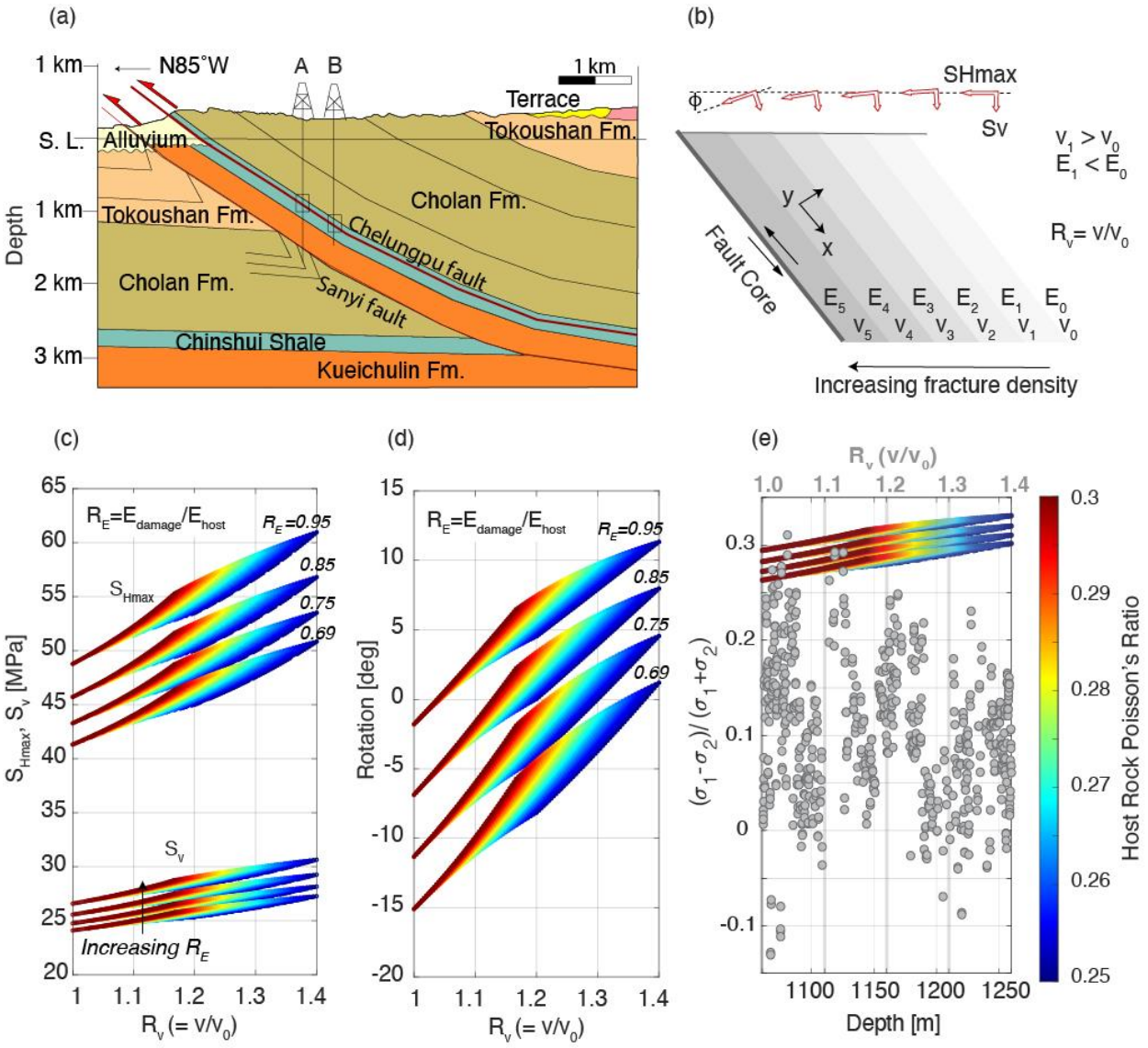

Figure 3.4. a) Vertical cross section of the Chelungpu fault system showing two boreholes (Hole A and B) drilled across the fault. b) Multilayer model showing layers of different elastic properties moving away from the fault core (not drawn to scale, number of layers arbitrary). ϕ is angle of rotation of the principal stress due to elastic property contrast. c) Principal stress magnitudes calculated from the multilayer model for a set of Young's modulus ratios and Poisson ratio ratios, color coded by the host rock Poisson's ratio. d) Rotation angle of the vertical principal stress plotted against a range of Poisson's ratio contrast (R_v). Possible range of S_v rotation is within ± 15° for host rock Poisson's ratio 0.25-0.35. e) Model (each diamond corresponds to a R_E ratio) and field data (gray circles) comparison of the ratio of maximum shear stress to mean stress. The multilayer model data has larger maximum shear stress to mean stress ratio than field observations.

3.5 Conclusions

We identify damage zones in the Chelungpu fault system as regions with low sonic velocity, increase in fracture density and enhanced caliper borehole diameter. Fracture density is the same in fault zones at different stages of the seismic cycle, but sonic velocity reduction and borehole enlargement are pronounced in the youngest faults compared to the older faults. This suggests that sonic velocity recovery and healing of fractures in the damage zone is a time-dependent phenomenon and correlated with fault zone age. The caliper diameter also has a positive correlation with exposure time of the borehole wall indicating a time-dependent borehole enlargement. Longer time of exposure of the first drilling period of Hole A drilling also leads to larger breakout width in Hole A compared to Hole B, suggesting time-dependent deformational behavior of the rock mass along the borehole.

Stress calculations also indicate that maximum principal stress magnitude is lower and minimum principal stress magnitude is higher in the damage zone, resulting in a relatively isotropic stress state. Changes in elastic properties in damage zone rocks could lower the differential stress in the damage zone by lowering stiffness and increasing Poisson's ratio; however, the elastic plane strain model alone cannot explain the observed low differential stress magnitude in the damage zone of the Chelungpu fault system. We therefore suggest that the low differential horizontal stress magnitude is indicative of long-term stress relaxation that occurred because of the ductile deformation of damaged rocks. Our results emphasize the need for characterizing time-dependent ductile deformation of damage zone rocks and its importance in interpreting fault zone stress states.

Acknowledgement

This study was supported by National Science Foundation Award No. EAR1727661.

References

Bird, P. (2009). Long-term fault slip rates, distributed deformation rates, and forecast of seismicity in the western United States from joint fitting of community geologic, geodetic, and stress direction data sets. *Journal of Geophysical Research: Solid Earth*, *114*(B11).

Byerlee, J. (1978). Friction of rocks. *Pure and Applied Geophysics PAGEOPH*. https://doi.org/10.1007/BF00876528

Casey, M. (1980). Mechanics of shear zones in isotropic dilatant materials. *Journal of Structural Geology*, *2*(1–2), 143–147.

Chester, F M, and Logan, J. M. (1986). Implications for mechanical properties of brittle faults from observations of the Punchbowl fault zone, California. *Pure and Applied Geophysics*, *124*(1), 79–106.

Chester, Frederick M, Evans, J. P., and Biegel, R. L. (1993). Internal structure and weakening mechanisms of the San Andreas fault. *Journal of Geophysical Research: Solid Earth*, *98*(B1), 771–786.

Cornet, F. H., Bérard, T., and Bourouis, S. (2007). How close to failure is a granite rock mass at a 5 km depth? *International Journal of Rock Mechanics and Mining Sciences*, *44*(1), 47–66.

Crouch, S. L., Starfield, A. M., and Rizzo, F. J. (1983). Boundary element methods in solid mechanics.

Faulkner, D. R., Mitchell, T. M., Healy, D., and Heap, M. J. (2006). Slip on'weak'faults by the rotation of regional stress in the fracture damage zone. *Nature*, *444*(7121), 922–925.

Fialko, Y. (2006). Interseismic strain accumulation and the earthquake potential on the southern San Andreas fault system. *Nature*, *441*(7096), 968–971.

Haimson, B., Lin, W., Oku, H., Hung, J. H., and Song, S. R. (2010). Integrating borehole-breakout dimensions, strength criteria, and leak-off test results, to constrain the state of stress across the Chelungpu Fault, Taiwan. *Tectonophysics*, *482*(1–4), 65–72. https://doi.org/10.1016/j.tecto.2009.05.016

Hirono, T., Yeh, E.-C., Lin, W., Sone, H., Mishima, T., Soh, W., et al. (2007). Nondestructive continuous physical property measurements of core samples recovered from hole B, Taiwan Chelungpu-Fault Drilling Project. *Journal of Geophysical Research: Solid Earth*, *112*(B7).

Hung, J. H., Ma, K. F., Wang, C. Y., Ito, H., Lin, W., and Yeh, E. C. (2009). Subsurface structure, physical properties, fault-zone characteristics and stress state in scientific drill holes of Taiwan Chelungpu Fault Drilling Project. *Tectonophysics*. https://doi.org/10.1016/j.tecto.2007.11.014

Johnson, K. M. (2013). Slip rates and off-fault deformation in Southern California inferred from GPS data and models. *Journal of Geophysical Research: Solid Earth*, *118*(10), 5643–5664.

Li, H., Wang, H., Xu, Z., Si, J., Pei, J., Li, T., et al. (2013). Characteristics of the fault-related rocks, fault zones and the principal slip zone in the Wenchuan Earthquake Fault Scientific Drilling Project Hole-1 (WFSD-1). *Tectonophysics*, *584*, 23–42.

Lin, A., Maruyama, T., and Kobayashi, K. (2007). Tectonic implications of damage zone-related fault-fracture networks revealed in drill core through the Nojima fault, Japan. *Tectonophysics*, *443*(3–4), 161–173.

Lindsey, E. O., Sahakian, V. J., Fialko, Y., Bock, Y., Barbot, S., and Rockwell, T. K. (2014).

Interseismic strain localization in the San Jacinto fault zone. *Pure and Applied Geophysics*, *171*(11), 2937–2954.

Ma, K.-F., Tanaka, H., Song, S.-R., Wang, C.-Y., Hung, J.-H., Tsai, Y.-B., et al. (2006). Slip zone and energetics of a large earthquake from the Taiwan Chelungpu-fault Drilling Project. *Nature*, *444*(7118), 473–476.

Ma, S. (2009). Distinct asymmetry in rupture-induced inelastic strain across dipping faults: An off-fault yielding model. *Geophysical Research Letters*, *36*(20).

Mastin, L. G. (1984). *The development of borehole breakouts in sandstone*. Stanford University, California.

Materna, K., and Bürgmann, R. (2016). Contrasts in compliant fault zone properties inferred from geodetic measurements in the San Francisco Bay area. *Journal of Geophysical Research: Solid Earth*, *121*(9), 6916–6931.

Meyer, G. G., Brantut, N., Mitchell, T. M., Meredith, P. G., and Plümper, O. (2021). Time dependent mechanical crack closure as a potential rapid source of post-seismic wave speed recovery: Insights from experiments in Carrara Marble. *Journal of Geophysical Research: Solid Earth*, *126*(4), e2020JB021301.

Moore, J. C., Chang, C., McNeill, L., Thu, M. K., Yamada, Y., and Huftile, G. (2011). Growth of borehole breakouts with time after drilling: Implications for state of stress, NanTroSEIZE transect, SW Japan. *Geochemistry, Geophysics, Geosystems*, *12*(4).

Paul, P., and Zoback, M. (2008). Wellbore-stability study for the SAFOD borehole through the San Andreas Fault. *SPE Drilling \and Completion*, *23*(04), 394–408.

Plumb, R. A., and Hickman, S. H. (1985). Stress-induced borehole elongation: A comparison between the four-arm dipmeter and the borehole televiewer in the Auburn geothermal well. *Journal of Geophysical Research: Solid Earth*, *90*(B7), 5513–5521.

Sahara, D. P., Schoenball, M., Kohl, T., and Müller, B. I. R. (2014). Impact of fracture networks on borehole breakout heterogeneities in crystalline rock. *International Journal of Rock Mechanics and Mining Sciences*, *71*, 301–309.

Scholz, C. H. (2019). *The mechanics of earthquakes and faulting*. Cambridge university press.

Shipton, Z. K., and Cowie, P. A. (2001). Damage zone and slip-surface evolution over $μ$m to km scales in high-porosity Navajo sandstone, Utah. *Journal of Structural Geology*, *23*(12), 1825–1844.

Sone, H, Condon, K. J., and others. (2017). Ductile behavior of thermally-fractured granite rocks. In *51st US Rock Mechanics/Geomechanics Symposium*.

Sone, H., and Uchide, T. (2016). Spatiotemporal evolution of a fault shear stress patch due to viscoelastic interseismic fault zone rheology. *Tectonophysics*. https://doi.org/10.1016/j.tecto.2016.04.017

Sone, H., Yeh, E.-C., Nakaya, T., Ji-Hao, H., Kuo-Fong, M., Chien-Ying, W., et al. (2007). Mesoscopic structural observations of cores from the Chelungpu fault system, Taiwan Chelungpu-fault Drilling Project Hole-A, Taiwan. *TAO: Terrestrial, Atmospheric and Oceanic Sciences*, *18*(2), 359.

Talukdar, M, Sone, H., and Griffith, W. A. (2021, June 18). Viscoplastic Modeling of Elastic and Creep Deformation of Fractured Berea Sandstone. *55th U.S. Rock Mechanics/Geomechanics Symposium*.

Talukdar, M., Sone, H., and Kuo, L.-W. (2021). Lithology and fault related stress variations along the TCDP borehole: the stress state before and after the Chi-Chi earthquake.

Yeh, E. C., Sone, H., Nakaya, T., Ian, K. H., Song, S. R., Hung, J. H., et al. (2007). Core description and characteristics of fault zones from Hole-A of the Taiwan Chelungpu-Fault Drilling Project. *Terrestrial, Atmospheric and Oceanic Sciences*. https://doi.org/10.3319/TAO.2007.18.2.327(TCDP)

Zoback, M. D., Moos, D., Mastin, L., and Anderson, R. N. (1985). Well bore breakouts and in situ stress. *Journal of Geophysical Research: Solid Earth*, *90*(B7), 5523–5530.

3.6 Appendix

3.6.1 Fracture intensity of Hole B cores

Figure 3.S1 shows the fracture intensity rating as defined by Sone et al. (2007) based on the number and characteristics of macroscopic fractures observed in the TCDP Hole A cores. For details on nomenclature, please refer to Section 2 of Sone et al. (2007).

index	definition	example
0	none or almost no fractures (1–2)	1249 
1	few fractures (3–7) in 1m core	1082 
2	several fractures (8–19) in 1m core	1228 
3	many fractures (>20) in 1m core	1104 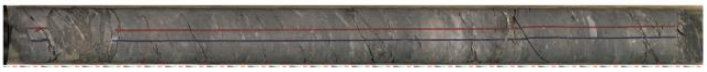
4	dense network of fractures	1145 
5	partially brecciated fractured rock	1164 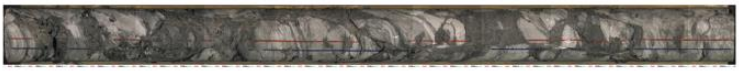
6	fault breccia	1152 
7	fault gouge	1111 

Figure 3.S1. Definition of fracture intensity index according to Sone et al., 2007.

CHAPTER 4

Time-dependent deformation of synthetically fractured rocks: Experimental Results and Viscoplastic modeling

Abstract

Fault damage zones undergo time-dependent deformation, which will progressively modify the stress state of fault zones. Characterizing such progressive stress evolution during the

interseismic period is important for seismic risk and hazard assessment. Therefore, in this study, we measure the time-dependent deformation of artificially fractured rocks. TCDP (Taiwan Chelungpu fault Drilling Project) core samples are fractured by impacting in a Split Hopkinson Pressure bar at strain rates analogous to those experienced by a natural damage zone during sub-shear to super-shear rupture. Samples are impacted at different strain rates to create a range of damage intensities which would increase towards the principal slip zone. We then subject the samples to constant stress hold stages in a triaxial apparatus to measure the creep deformation of the rocks. With increased damage, the creep deformation increased. This increase in creep with damage is attributed to the higher compaction of fracture volume, as observed from microstructural observations. Next, we modeled the volumetric strain of the specimens using a Perzyna viscoplasticity law that employs the Modified Cam Clay model as the yield criterion (Haghighat et al. 2020). The model fits the experimental data well, but we observe tradeoffs between parameters, which means that the experimental data can be fit equally well using different sets of constitutive parameters. The viscoplastic model shows that highly damaged specimens with greater fracture volume and higher creep deformation have higher elastic and inelastic compliance. Due to the high density of microfractures in highly damaged specimens, the overall resistance to flow of the specimen is low, leading to low apparent viscosity of the material. Conversely, intact samples have high viscosity.

4.1 Introduction

Damage zones are ubiquitous features in fault zones, and are characterized by the presence of pervasive fractures (Ben-Zion and Sammis, 2009; Kim et al., 2014). Fractures reduce the elastic stiffness of damage zones, therefore damage zones are mechanically weak, and susceptible to further deformation (Healy, 2008). Compliant damage zone rocks not only deform

elastically, but also deform plastically under tectonic forces. Plastic deformation of materials is usually time-dependent, thus characterizing such time-dependent deformation of fault damage zone rocks is important to understanding the rheology and long-term behavior of fault zones.

Pore volume reduction under applied stress is enhanced in semi to unconsolidated sediments due to the high pore volume in their structure. In field scale, compaction of unconsolidated sands in Wilmington field and San Joaquin valley, California has been reported to be a time-dependent process (Kosloff et al., 1980). Similar observations have been proposed in Bolivar coast heavy oil fields (Puig et al., 1984). Laboratory experiments have observed that pore volume compaction is a time-dependent process (Cogan, 1976; Dudley et al., 1998; Ostermeier, 1995). Various explanations of such time-dependent compaction of pore volume in rocks and sediments are: pore-fluid expulsion under drained conditions (Cogan, 1976; Hornby, 1998), pressure distribution under undrained conditions (Holzer et al., 1973; Jones and Wang, 1981) as well as creep and stress relaxation of dry sediments (Carl Chang et al., 1997; Hagin and Zoback, 2004a, 2004b). Chang and Zoback (2009, 2010) and Sone and Zoback (2013b) also observed a reduction in sample volume with creep deformation in Gulf of Mexico shale and shale-gas reservoir rocks, respectively. These studies suggested that reduction in sample volume showed a positive correlation with the amount of clay and kerogen present in the rock, indicating that clay compaction induces sample volume reduction. These observations suggest that compaction and time-dependent deformation are closely related processes that determine the long-term behavior of porous materials.

In fault damage zone rocks in lithified rocks, fractures increase the porosity by adding fracture volume to pore volume. Furthermore, fault damage zones often include clay minerals. Thus, we expect fractured damage zone rocks to undergo considerable compaction in pore

volume upon application of force by a combination of processes like clay compaction and, pore and fracture aperture closure, thereby enhancing the mesoscopic ductile deformation in fractured rocks. The fracture planes may also act as slip planes which allow stable sliding along cracks, leading to bulk deformation of the material. This study aims to characterize the magnitude of time-dependent strain due to bulk creep deformation of damaged rocks.

Various constitutive relations have been proposed to characterize the time-dependent properties of rocks. While some studies suggest a power law relationship to characterize creep deformation (Dudley et al., 1994; Hagin and Zoback, 2004b; Sone and Zoback, 2013, 2014a, 2014b), other studies have used Prony series (Cheng et al., 2022; Nadimi and Shahriar, 2014; Song et al., 2021; Trzeciak et al., 2018). Both types of models are unable to capture the anelastic behavior observed between the loading and unloading stages. These studies are also unable to describe the irrecoverable or permanent strain after time-dependent deformation (Ding et al., 2017; Andargoli et al., 2019; Wang et al., 2021; Wu et al., 2015). These shortcomings highlight the need for a constitutive relationship that can model the mesoscopically plastic and time-dependent deformation. Viscoplastic models address these shortcomings of viscoelastic models. One such model recently used to describe the behavior of shales combines Perzyna viscoplasticity with the modified Cam-Clay model and utilizes only stress history as an input to predict the resultant elastic and plastic strain during deformation (Haghighat et al., 2020). In this study, we use the viscoplastic model proposed by Haghighat et al. (2020) to describe the ductile behavior of damaged rocks.

Although there are various viscoplastic models that characterizes the ductile behavior of rocks, the physical mechanisms governing such deformation and their relative contributions are unknown. Not only are the relative contributions unknown, but also the time extent over which

these physical mechanisms are active is difficult to predict. Characterizing the time extent of these physical mechanisms is important to understand the time required for one mechanism to slow down and another mechanism to get dominant. For instance, mesoscopic ductile deformation of damage zone rocks is a combination of compaction creep of the matrix porosity, fracture porosity, sliding along grain boundaries of clay rich minerals, sliding along crack surfaces and mineral plastic creep. In a shallow damage zone, we expect compaction creep of fracture porosity and sliding along crack surfaces to primarily constitute the volumetric deformation in a short time scale. The other processes like compaction creep of matrix porosity, sliding along crack surfaces and mineral plastic creep are slower mechanisms (also active in a non-fractured rock), and are therefore expected to become dominant once the creep mechanisms due to the presence of fractures slow down during the interseismic process. In this study, we attempt to use the viscoplastic formulation to provide insights into the time extent over which some of these physical mechanisms are active.

Characterizing the time-dependent deformation of damage zone rocks is important to study how strain accumulates throughout the seismic cycle. If we consider a fault system with a locked patch and a far-field tectonic displacement, shear stress accumulates in the locked region of the fault during the interseismic period due to elastic loading. However, in the presence of viscous deformation in the adjacent damage zone, the shear stress accumulated in the locked patch may progressively diffuse to the surrounding rock mass and other regions of the fault plane during the interseismic period (Sone and Uchide, 2016). The deformation that causes the shear stress diffusion in the surrounding damage zone results in healing of fractures in the damage zone. Healing of fractures or reduction of fracture volume in damage zones can increase the mechanical strength of rocks during the inter-seismic period after earthquakes (Gratier et al.

2011). Eventually, healed damage zones may regain the ability to store elastic energy and shear stress. Thus, the stress diffusion into the damage zone acts to delay the timing at which faults reach a critical stress state.

Fault damage zones show a decay in damage density with distance from the fault, therefore, rocks closest to the fault core are more likely to deform by time-dependent deformation than intact host rock. To study the effect of damage on time-dependent deformation, we created synthetic damage zone material with a range of damage density. We conducted time-dependent creep experiments to constrain the viscoplastic behavior of damaged rocks at in-situ stress conditions. Microstructures were observed using a scanning electron microscope and X-ray computed tomography scans to aid interpretation of the physical process of healing in the samples. The objective of this chapter is to understand the viscoplastic deformation of damaged rocks and understand the physical mechanisms that contribute to such deformation.

4.2 Materials and Method

4.2.1 Geological setting and materials

Taiwan is located between the Philippine Sea plate and the Eurasian plate, with two subduction zones in the east and south; Ryukyu arc trench and Luzon arc, respectively (Yue et al., 2005). Due to this location, Taiwan is one of the most seismically active countries in the world. A Mw 7.6 earthquake struck east-central Taiwan with its epicenter near the town of Chi-Chi on 21st September 1999 (Kao and Chen, 2000). The 1999 Chi-Chi earthquake was the most destructive earthquake of the 20th century in Taiwan, creating a surface rupture of about 85 km along the Chelungpu fault in Western Taiwan (Wang et al., 2005). The earthquake occurred along a North-South trending and 30° dipping fault and involved thrust and left-lateral slip

components. Five years after the earthquake, the Taiwan Chelungpu fault Drilling Project (TCDP) drilled two scientific boreholes across the Chelungpu fault system to study the mechanics of earthquake and faulting in the area (Ma et al., 2006). Two vertical boreholes: Holes A and B, encountered the slip plane of the Chi-Chi earthquake at 1111 m and 1133 m, respectively. The two boreholes collected samples at depth ranges of 500-1800 m from Hole A and 500-1300 m from Hole B. This study used host rocks collected from the TCDP borehole for mechanical testing. The four rock types used in this study are siltstone, bioturbated siltstone, sandy siltstone, and sandstone.

4.2.2 Damage creation using Split Hopkinson Pressure Bar

For this study, we impacted core samples from the Taiwan Chelungpu fault Drilling Project (TCDP) with a Split Hopkinson Pressure bar (SHPB) to create fractures within specimens (Chen and Song, 2010; Kolsky, 1949). The primary reason to choose SHPB to create fractures is to disrupt strain localization and foster pervasive damage, resulting in samples analogous to natural damage zone rocks (Aben et al., 2016; Doan and Gary, 2009). Additionally, previous experimental and field studies have indicated that the strain rates achieved by SHPB are of the same order of magnitude as strain rates observed in damage zones during sub-shear to super shear rupture (Doan and Billi, 2011; Doan and d'Hour, 2012; Xia et al., 2008; Yuan et al., 2011). These studies show that rock fabrics after SHPB impact are still recognizable through fracture networks, consistent with micro-structural observations of damaged and pulverized natural damage zone rocks (Mitchell et al., 2011). Thus, we impact the samples with SHPB to recreate natural damage zone materials, which are characterized by pervasive damage and created at high strain rates during earthquakes.

We acquired cylindrical plugs from TCDP rocks with a coring machine. Uniaxial

experiments on samples cored parallel and perpendicular to bedding show that there is not a significant anisotropy in TCDP cores. Hence, we cored perpendicular to the bedding plane. Each cylindrical core plug is 1.5 inch (38.1 mm) in length and 1 inch (25.4 mm) in diameter. We maintained the length to diameter ratio of 3:2 instead of 2:1 (standard for triaxial tests) because low length to diameter ratio improves the homogeneity of sample deformation during SHPB experiments (Dai et al., 2010). The cored cylindrical plugs were then dried at 80 ºC for 12 hours in an oven under vacuum. After drying the samples, we placed metal disks, 0.2 inch (5 mm) in thickness and 1 inch (25.4 mm) in diameter, on either end of each plug before the SHPB tests to maintain flat parallel ends after fracturing (Figure 2a). The metal disks were made of the same material (maraging steel) as the incident and transmitted bars of the SHPB to remove any impedance contrast between the incident bars and the metal. Subsequently, we jacketed the samples with heat-shrink polyolefin to retain the impacted rock inside the jacket upon impact. This jacket is the inner or first jacket of the sample in Figure 4.2a.

We cored five cylindrical plugs from each lithology tested. One sample from each group was not impacted with SHPB for comparison between impacted and damaged specimens. The remaining four specimens were impacted at incremental charge gas pressure magnitudes to produce a range of strain rate and fracture densities in the specimens. The four samples with increasing degree of damage are denoted by D1, D2, D3 and D4, respectively, whereas the intact sample is denoted as D0. For example, bioturbated siltstone samples deformed at 12, 14, 16, 18 psi charge gas pressure are marked as D1, D2, D3 and D4 respectively. The maximum strain rates attained during impact of the D1-D4 samples are summarized in Table 4.1.

Table 4.1. Applied gas pressure and achieved strain rate during SHPB impact along with porosity creation due to impact.

Rock type and damage intensity	Gas Pressure [psi]	Strain Rate [1/s]	Pre-impact Porosity (%)	Post-impact Porosity (%)	Void ratio
Siltstone					
D0	0	0	4.7	4.8	0.050
D1	15	134	4.7	5.5	0.058
D2	20	166	4.9	13.4	0.155
D3	25	200	4.8	17.9	0.218
D4	30	272	5.1	26.3	0.357
Bioturbated Siltstone					
D0	0	0	6.0	6.0	0.064
D1	14	108	6.1	7.8	0.085
D2	16	127	6.1	9.7	0.107
D3	18	170	6.6	15.4	0.182
D4	20	176	6.6	16.0	0.191
Sandy Siltstone					
D0	0	0	4.0	4.0	0.042
D1	12	87	4.2	4.6	0.048
D2	15	127	4.5	6.1	0.065
D3	20	155	4.4	12.2	0.139
D4	24	192	4.4	17.3	0.209
Sandstone					
D0	0	0	20.0	20.0	0.250
D1	10	88	20.7	19.7	0.245
D2	12	130	20.3	19.2	0.238
D3	14	154	20.8	22.7	0.294
D4	16	185	21.4	25.6	0.344

4.2.3 Creep experiments

We conducted creep experiments in a conventional servo controlled triaxial apparatus in dry conditions with no pore pressure. While a first layer of polyolefin was used to hold the sample in place during and after SHPB impact, a second layer of heat-shrink polyolefin jacket was used to seal the samples from the confining oil (Figure 4.2a). The samples were subsequently placed between two endcaps. Creep deformation of the damaged specimens was observed at various confining pressure and axial differential stress stages. We loaded the specimens to 5, 10, and 15 MPa confining pressure and held the stress constant for 3 hours (top part of Figure 4.1). After each creep stage, the confining pressure was unloaded followed by

reloading to observe the static elastic behavior of the sample. The duration of loading and unloading stages was 30 seconds. After a hydrostatic creep stage at 15 MPa confining pressure, we performed triaxial tests at a constant confining pressure of 15 MPa. Samples were subjected to axial differential stress magnitudes of 5, 10, 15, 20 and 25 MPa with loading, creep and unloading stages similar to the confining pressure stages (Figure 4.1). These confining pressure and differential stress magnitudes were chosen to resemble in-situ stress conditions from which the TCDP cores were acquired, i.e., a depth of 1000 m, which corresponds to 15 MPa vertical stress and 25 MPa horizontal stress.

We measured the output axial deformation response corresponding to the aforementioned input stress history with a Linear Variable Differential Transducer (LVDT). We used strain gage-based sensors to record the lateral deformation of the material. Deformation was recorded at a sampling interval of one second. Axial and radial strain is determined by averaging the axial strain measurements from two LVDTs and two strain gages, respectively. We took the sum of the axial strain and twice the radial strain to calculate volumetric strain. An example of a volumetric strain data from a siltstone specimen is shown in Figure 4.1. Piezoelectric crystals are embedded in the top and bottom platens to record ultrasonic waves during the experiment and determine the P and S waves velocities of the sample. The ultrasonic waves were recorded every 1 minute. One such result is shown in Figure 4.1. Figure 4.1 captures the time-dependent increase in velocity and strain during the constant stress stages.

There are three-time stamp references for a single sample in this study, ‘initial’, ‘impacted’ and ‘healed’, referring to initial intact condition of the rock, samples after SHPB

impact at high strain rate and healed due to creep, respectively. These terminologies are used in the rest of the chapter and should not be confused with ‘intact’ and ‘damaged’ samples. ‘Intact’ specimens allude to specimens which are not ‘impacted’ with SHPB, whereas ‘damaged’ specimens are ‘impacted’ with SHPB.

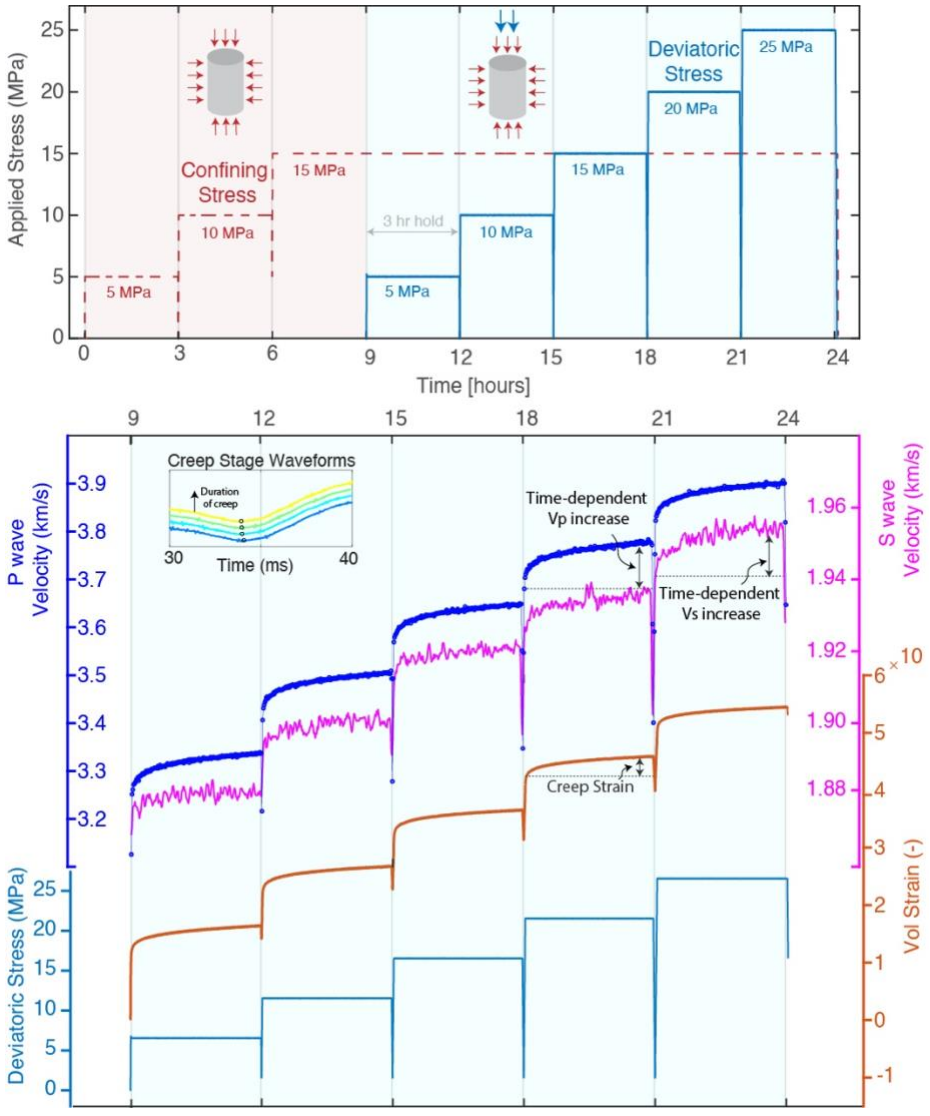

Figure 4.1. (top) Confining pressure and deviatoric stress magnitude history during each experiment. The constant stress stages are 3-hour stages. (bottom) Input deviatoric stress history and corresponding output history of creep strain, S wave velocity and P wave velocity (from top to bottom) during the triaxial stage. The plot shows time-dependent creep strain and increase in P and S wave velocity at constant deviatoric stress.

4.2.4 Porosity Calculation

We measured the porosity of each sample before SHPB impact using a helium porosimeter. Helium porosimeters are designed to measure the porosity of rock plugs using the principle of the Boyle's law. After placing the sample in the sample chamber, helium is injected into the chamber to determine the loss of helium volume into the pores, and thereby determine the sample pore volume. Porosity of the rock plugs calculated with the helium porosimeter are shown in Table 4.1. We observe that the porosities of the siltstone samples are lower (4-7%) than the sandstone samples. The sandstone samples are highly porous and weakly-consolidated, therefore the sandstone in this region has a porosity of ~20% (Talukdar et al., 2022).

Since the SHPB impact creates fractures and pores in these specimens, we also determined the porosities of the samples after SHPB impact. The helium porosimeter could not be used to measure the porosities of the impacted samples as the samples were already jacketed, and metal discs were placed on either end of each sample to keep the damaged rock in place. Instead, we used a Vernier caliper to measure the dimensions of each impacted samples to calculate the final volume of the sample V_f. The change in porosity caused by SHPB impact is added to the intact sample porosity $\emptyset_i$ to calculate the porosity of the sample after SHPB impact $\emptyset_f$.

$$\emptyset_{\mathrm{f}} = \emptyset_{\mathrm{i}} + \frac{\mathrm{V_f} - \mathrm{V_i}}{\mathrm{V_i}} \qquad (4.1)$$

Table 1 lists the porosity of each sample after damage creation. We observe that in the siltstone varieties (siltstone, sandy siltstone and bioturbated siltstone), the change in porosity is higher at higher strain rates, indicating a larger fracture volume created within the sample at

larger strain rate of impact. For example, the porosity change from D0-D4 for bioturbated siltstone was 0, 1.7, 3.6, 8.8, and 9.4 %, respectively. However, in sandstone, D1 and D2 specimens showed reduction in pore volume with higher strain rate (Table 1). Porosity changes for D1 and D2 sandstones are -0.98 and -1.1%, respectively. With further increase in strain rate, the D3 and D4 sandstone showed increases in porosity of 1.89 and 4.23 %, respectively.

4.2.5 Micro-Computed Tomography

We acquired X-ray micro computed tomography (Micro-CT) images of few samples after SHPB impact to characterize the microstructure of these impacted rocks. An NSI scanner with a Fein Focus High Power source (located at University of Texas CT scan facility) was used with a voltage of 150kV and current of 0.22 mA. Micro-CT slices are obtained with a voxel size of 14 μm. Despite the 1.5" length of the sample, only the middle 1" of the sample was scanned to avoid the high-density contrast at the rock-metal boundary which would reduce the image quality. The CT scan slices obtained along the radial direction of each sample are subsequently assembled to form a volumetric reconstruction (Figures 4.2b-e). Micro-CT volumes of D1 to D4 sandy siltstone specimens captured the increase in fracture volume with increasing strain rate of impact, as shown from Figures 4.2b-e.

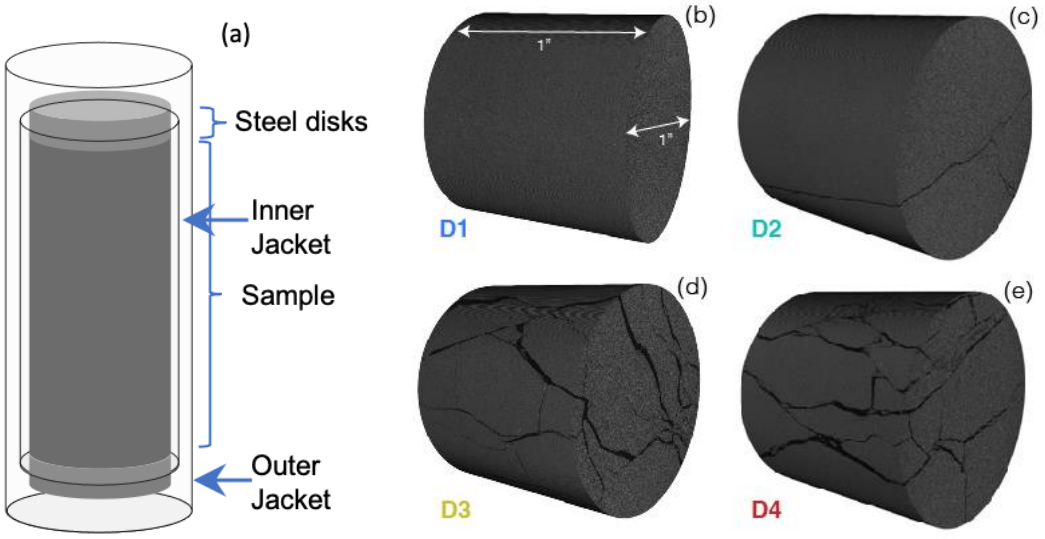

Figure 4.2. (a) Schematic of sample assembly consisting of 'maraging steel' disks and polyolefin jackets. (b-d) Volume reconstruction of sandy siltstone specimens for the middle 1" of each sample. Increasing strain rate of impact created (b) D1, (c) D2, (d) D3 and (e) D4 sample fracture networks, respectively.

4.3 Results

4.3.1. Mechanical Behavior

Representative strain data from the triaxial stages of the experiments are shown in Figure 3. In Figure 4.3a, axial strain is plotted with differential stress for all the siltstone samples to show the influence of damage on the stress-strain behavior. The resulting strain history with time is shown in Figure 4.3b. We first observe that the total axial strain is higher for damaged specimens. Figures 3a and 3b show that total axial strain of D0 (blue data in Figure 4.3) during the triaxial stage is 2.9×10^{-3}, less than $1/3^{rd}$ of the total strain of the most damaged D4 sample: ~8.7×10^{-3} (red data).

Second, we observe that for every sample, considerable deformation occurs when the sample is loaded, i.e., when differential stress is increased. The loading part of the deformation comprises two portions: i) first loading and ii) reloading. During the first loading, or the first time a sample experiences a certain magnitude of differential stress, frictional sliding leads to inelastic deformation. In this case, the sample strains more with less change in stress. Reloading is when the sample experiences stress magnitudes it has previously experienced. This part of the deformation is accommodated only by elastic deformation of the minerals and the pore space. Thus, the slope of the stress-strain relation is steeper (i.e., rock is stiffer) than during first loading. From Figure 4.3a, we observe that for the same loading step, both elastic and inelastic strain increase with increase in initial damage. The increase in elastic and inelastic deformation with damage suggests low elastic and inelastic compliance of damaged rocks. The slopes of stress-strain curves representing elastic and inelastic deformation are further discussed in section 4.4.

Third, we compare the creep stages of the damaged samples, which appear as straight horizontal lines in Figure 4.3a. We observe that the length of the horizontal lines increases as damage increases from D0 to D4, suggesting more creep in highly damaged specimens. The creep strain accumulated during each differential stress hold stage are also shown in the axial strain-time plot (Figure 4.3b). More strain in damaged specimens may be caused by compaction of the samples during creep. We observe more pore volume compaction in D4 sample (red data), likely due to the greater fracture volume available for compaction in more damaged specimens (as observed from CT scan volumes in Figure 4.2b-d).

Fourth, we observe an increase in hysteretic behavior of samples (i.e., the difference between the reloading and unloading) with increasing damage (Figure 4.3a). Increasing area of

the hysteresis loop with damage indicates that more energy is dissipated during deformation in a damaged sample than an undamaged specimen. For instance, the area under the last hysteresis loop for D4 sample is about twice the last hysteresis loop area of D0 sample. Since there are more fractures present in D4 than D0, frictional sliding along the fracture surfaces is more susceptible in D4, leading to more energy dissipation in D4.

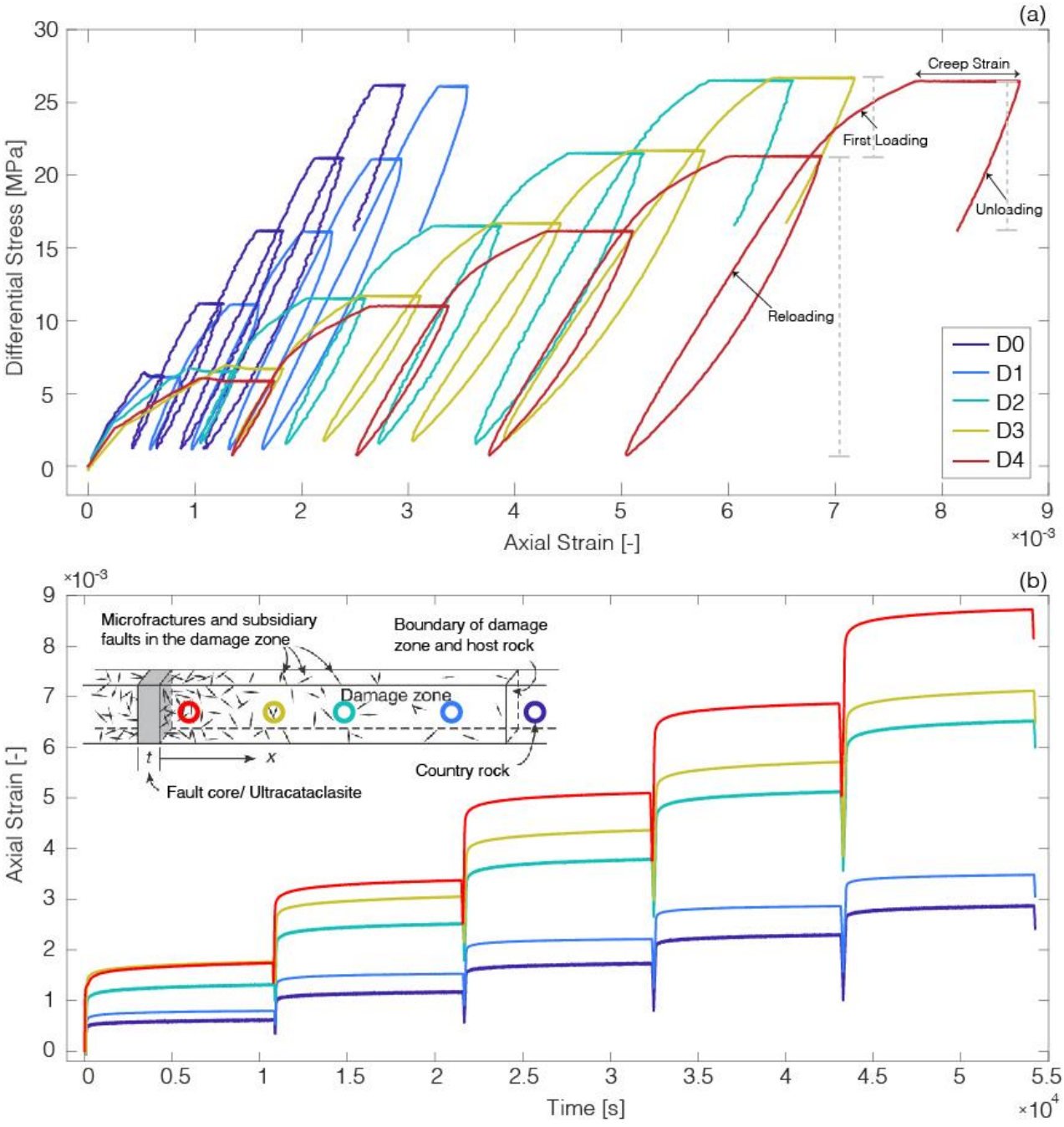

Figure 4.3. The axial strain response of each siltstone specimen to applied differential stress is plotted in (a) stress-strain plots and (b) strain-time plots at 15 MPa confining pressure. (a) From blue to red (left to right), elastic, inelastic and creep strain increases with increasing damage. (b) Axial strain history of siltstone samples with varying degrees of damage. Distances in the insert are arbitrary.

Velocity increases during loading due to reduction in fracture volume and increase in elastic stiffness of the rock, and vice versa (Figure 4.1a). Both P and S wave velocity also show time-dependent increases during the hold stages. We discuss the velocity results in Chapter 5.

4.3.2 Influence of damage and differential stress on creep behavior

In this section, we focus on the 3 hours hold stages to compare the creep behavior of the samples through strain-time plots (Figure 4.4). Creep deformation observed in Figure 4.4a is possibly a result of two different processes: (i) Time-dependent compaction of mineral and matrix porosity, (ii) Time-dependent compaction of the additional fracture volume created by SHPB and sliding of newly opened fracture surfaces past each other. Creep deformation in the intact specimen is a result of (i). Previous studies have suggested time-dependent deformation of pore spaces in clays and organic matter (Sone and Zoback, 2013; Trzeciak et al., 2018). Presence of pore spaces in clays and organic matter in the TCDP siltstone specimens could possibly result in time-dependent compaction of D0 sample. The magnitude of axial creep strain for the D0 siltstone specimen at 20 MPa differential stress is ~ 2×10^{-4}, the magnitude comparable to past 3 hr creep experiments on organic-rich shales (Sone and Zoback, 2013; Trzeciak et al., 2018).

Strain-time plots in Figure 4.4a and 4.4b at a specific differential stress magnitude also show that both axial and volumetric strain increase with increasing damage, as described previously in Section 4.3.1. The increase in creep strain from D0 to D4 suggests that D1-D4 samples not only undergo pore-volume compaction but also experience time-dependent fracture

volume reduction (or fracture closure) facilitated by asperity deformation and sliding along fracture surfaces. This suggests that the difference between D0 and D1 creep strain (dark and light blue data, respectively) is a result of time-dependent closure of the newly created fractures present in D1. Samples impacted at higher strain rate show more time-dependent deformation because they contain more fracture volume and higher fracture density.

To compare strain rates during creep stages, we calculate the strain rate for a time interval of 1000 seconds during each experiment (Figure 4.4d, e). Axial and volumetric strain rate data demonstrates that strain rate is highest at the beginning of creep stage and diminishes at the end of the stage. Damaged samples show higher axial and volumetric creep strain rate than intact samples, indicating faster fracture volume closure and fracture sliding in more damaged samples.

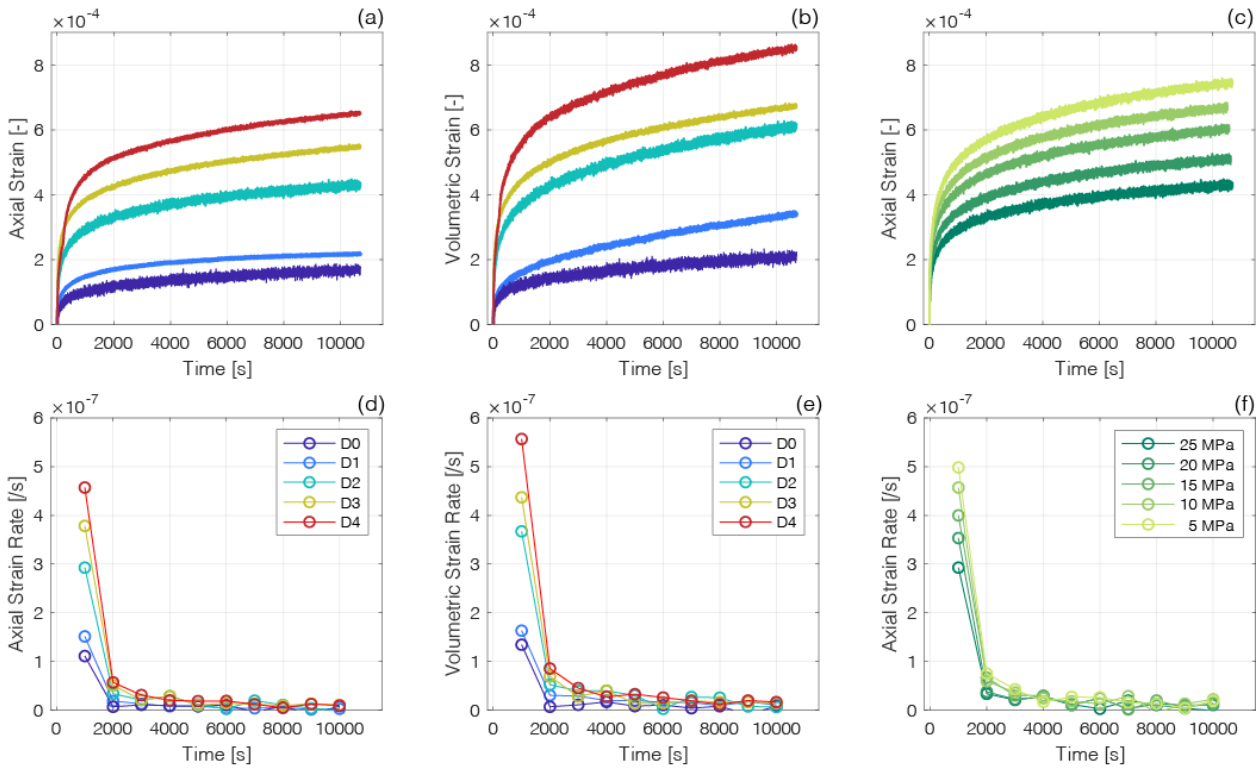

Figure 4.4. Creep strain and creep strain rate dependence on degree of damage and differential stress magnitudes for Siltstone specimens. (a) Axial and (b) volumetric creep strain during the

20 MPa hold stage. (c) Axial creep strain of D2 Siltstone specimen at various differential stress magnitudes. Creep strain rate calculated from (d) Axial strain and (e) volumetric strain for various degrees of damage. (f) Dependence of differential stress on axial strain rate magnitude.

We observe differential stress dependence on creep. With increasing differential stress, the magnitude of creep deformation declines (Figure 4.4c). This indicates less time-dependent compaction and limited crack sliding at higher differential stress magnitudes. Less compaction at higher differential stress reflects the fact that fracture volume has declined by the time stress magnitudes are high at a later stage in the experiment. These observations suggest that creep strain rate is a function of the amount of remaining fracture pore volume, which is an important observation that constrains the form of the appropriate viscoplastic constitutive law to use.

4.3.3 Microstructural Characterization

4.3.3.1. Scanning Electron Microscope Observations after creep

Following the creep experiments, we observe the microstructural characteristics of the circular cross-section of each sample using a scanning electron microscope (SEM). We impregnated fractures with epoxy to ensure that the samples remained intact during preparation of samples for imaging. We cut the samples mid-length, perpendicular to the longitudinal axis of each sample.

Elementary Dispersive Spectroscopy (EDS) suggests that the sandy siltstone specimens contain quartz, feldspar, and clay. Clay minerals are abundant in the matrix surrounding quartz and feldspar grains. This explains the considerable creep deformation observed in the intact siltstone sample (blue data in Figure 4a, b). Approximately 1/3rd of each sample consists of clay, also evident from XRD analysis of TCDP siltstones by Kuo et al. (2009). The primary clay minerals present in the rock are chlorite, illite, kaolinite and smectite, among others.

SEM images highlight the nature and orientation of fractures in these rocks. The grain boundaries of the intact D0 sample are not as clear as those of the damaged sample (Figure 4.5a, b, c). D2 sample shows regions of localized deformation along grain boundaries, which appear as dark lines along the grains (Figure 4.5b), indicated as IF (Inter-granular fractures). The grain boundaries are even more clear in the D4 sample because of the presence of large-aperture cracks along grain boundaries. In D4, the grain boundary cracks combine to form one single fracture. Fractures may also be present in the matrix but are difficult to identify because of fine texture defined by the fine-grained clay minerals in the matrix.

D2 and D4 samples show some fractured grains, indicated as FG in Figures 4.5d, f. These intragranular fractures are easily identifiable in D4 because of the wider fracture apertures in D4 than D2. Figures 4.5g-i highlight the presence of open fractures (OF) in these specimens. Figure 4.5g shows that a high density of intragranular fractures coalesce to create distributed pore space expansion in D4. Certain regions of such fracture coalescence are also characterized by small grain size, indicated by CG (crushed grains) in Figure 4.5g. These fine grain size regions appear like crushed grains with some larger grains floating inside the powdery material.

We note that while grain boundary fractures and fractured grains co-exist in these specimens, fractures are predominantly present along grain boundaries.

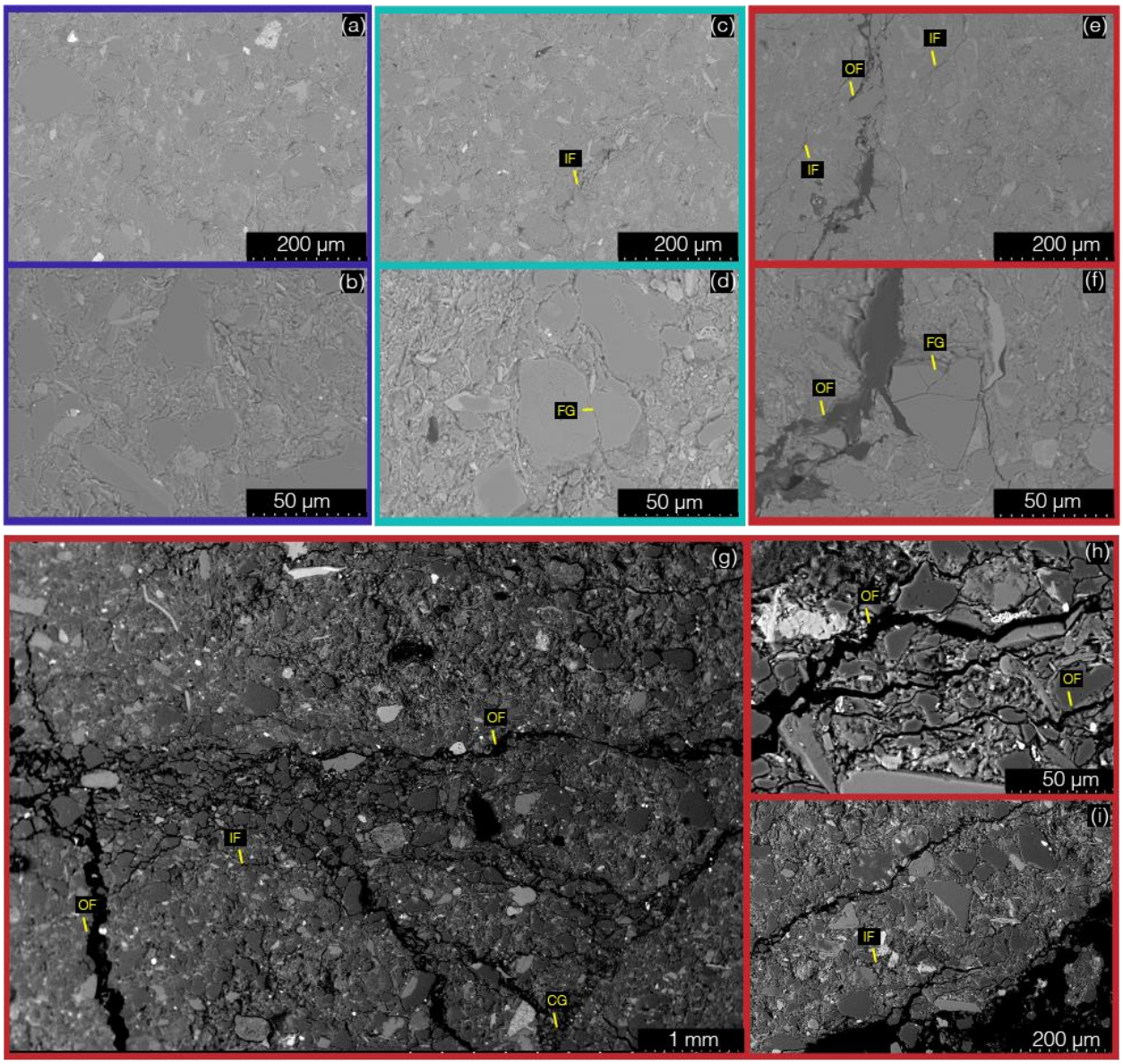

Figure 4.5. Back-scattered scanning electron microscope images of sandy siltstone specimens. (a, b) D0, (c,d) D2, (e, f) D4. (g, h, i) 3-D back-scattered electron images of D4 sandy siltstone. IF: Inter-granular fractures, FG: Fractured grains, OF: Open fractures, CG: Crushed grains.

4.3.3.2. Micro-CT Observations before and after creep

CT scan slices of the samples show the fractures formed due to SHPB experiments (Figures 4.6a-d). Since the voxel size of the CT scan is 14µm, the fractures observed are larger than 14µm.

Although CT scans could not reach the high resolution observed with the SEM, we conducted CT scans to make semi-quantitative comparison of samples before and after the creep experiments while the samples were jacketed and held within the endcaps (Figure 4.2a). CT scan volumetric reconstruction of sandy siltstone samples shows that at low strain rates, most fractures created were longitudinal opening fractures that formed parallel to the direction of loading (Figure 4.2b-d). At higher strain rates, however, the proportion of oblique shear fracture increased relative to the longitudinal opening fractures. We interpret that the viscoelasctic nature of the polyolefin jacket prevents the jacket from expanding at higher strain rates which results in more confinement pressure at high strain rate. Higher confinement by the jacket may suppress longitudinal opening fractures and promote oblique shear fractures.

CT scan slices of sandy siltstone specimens show that fracture density in the specimens increased with increasing strain rate of impact (Figure 4.6a-d). Fracture apertures increase with increasing damage is also observed (Figures 4.6b-d). D3 and D4 samples show fine-grained regions at the intersections of the fractures, where intense fracturing occurs. These fragments fill fracture pore spaces in the highly damaged specimens. In summary, increasing fracture density, fracture aperture, and fragmentation in damaged specimens result in pore volume increase with increasing strain rate of impact (Figures 4.6a-d).

Images of the healed samples, or samples after creep experiments, sliced at the same height are shown in the bottom row (Figures 4.6e-h). At the scale of observation, D1 sample shows no change in characteristics as it cannot resolve the micron scale fractures observed in SEM images. Healed D2 sample shows a decrease in fracture aperture because of compaction and sliding along crack surfaces, indicated as FC/ Fracture Closure in Figure 4.6f. Decrease in fracture aperture and total closure of fractures (TC) are observed in D3 and D4 samples (Figures

4.6g, h). Fractures which are filled up with crushed grains (CG) also compact and heal more quickly than unfilled fracture apertures (Figure 4.6h). Such decrease in fracture aperture correspond to the permanent strain caused by the instantaneous and time-dependent plastic strain as seen by the comparison between the pre- and post-creep samples at unloaded state.

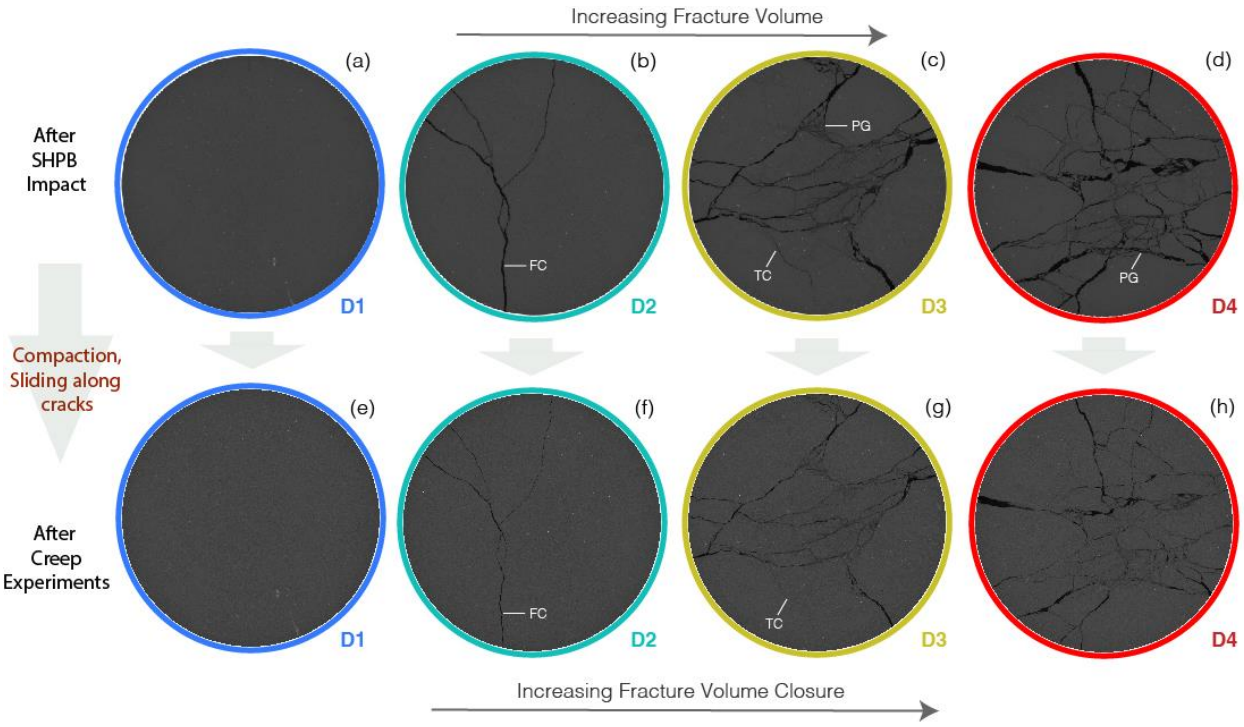

Figure 4.6. Computed Tomography images for Sandy siltstone specimens. (a-d) Mid-height CT scan slice of D1, D2, D3 and D4 sample, respectively after damage creation using SHPB. (e-h) Mid-height CT scan slices of D1-D4 after creep experiments. FC: Fracture aperture closure, TC: Total fracture closure, CG: Crushed Grains.

We estimate the porosity of each sample before and after creep experiments with the help of pixel values. Siltstone pixel values show a bimodal distribution: i) mode with a lower pixel value for fractures as they appear as dark spots in the figure and ii) mode with a higher pixel value for the matrix. To quantify the fracture and matrix porosity of the sample, we separate the bimodal distribution by setting a pixel threshold. The pixel threshold is chosen to be the average

of the two modes. The ratio of number of pixels below the threshold to the total number of pixels gives an estimate of the porosity of the samples. Figure 4.7 shows the corresponding porosity obtained by this approach. After SHPB impact, the porosity of the sample increased with increasing damage intensity from 3 to 17% (Figure 4.7a to 4.7d). When compared with porosity values of the post-impact samples estimated from helium porosimetry and caliper measurements in Table 4.1, the before-creep sample porosities shown here agree within 2%, which confirms the first order accuracy of the semi-quantitative estimates based on the CT scan images.

Histograms of pixel values of the healed images are overlaid on top of pixel histogram before creep. The healed histograms have a higher average value and plot towards the right because they have lower porosity. We note that the measured porosity is not a quantitative estimate but a semi-qualitative evaluation of porosity before and after creep experiments.

A comparison of mode with high pixel value (representing matrix) before and after creep also shows that post-creep histogram mode is higher than the pre-creep mode. This indicates closure of invisible fractures in the matrix, that the thresholding criterion cannot capture but the absolute pixel value magnitude can.

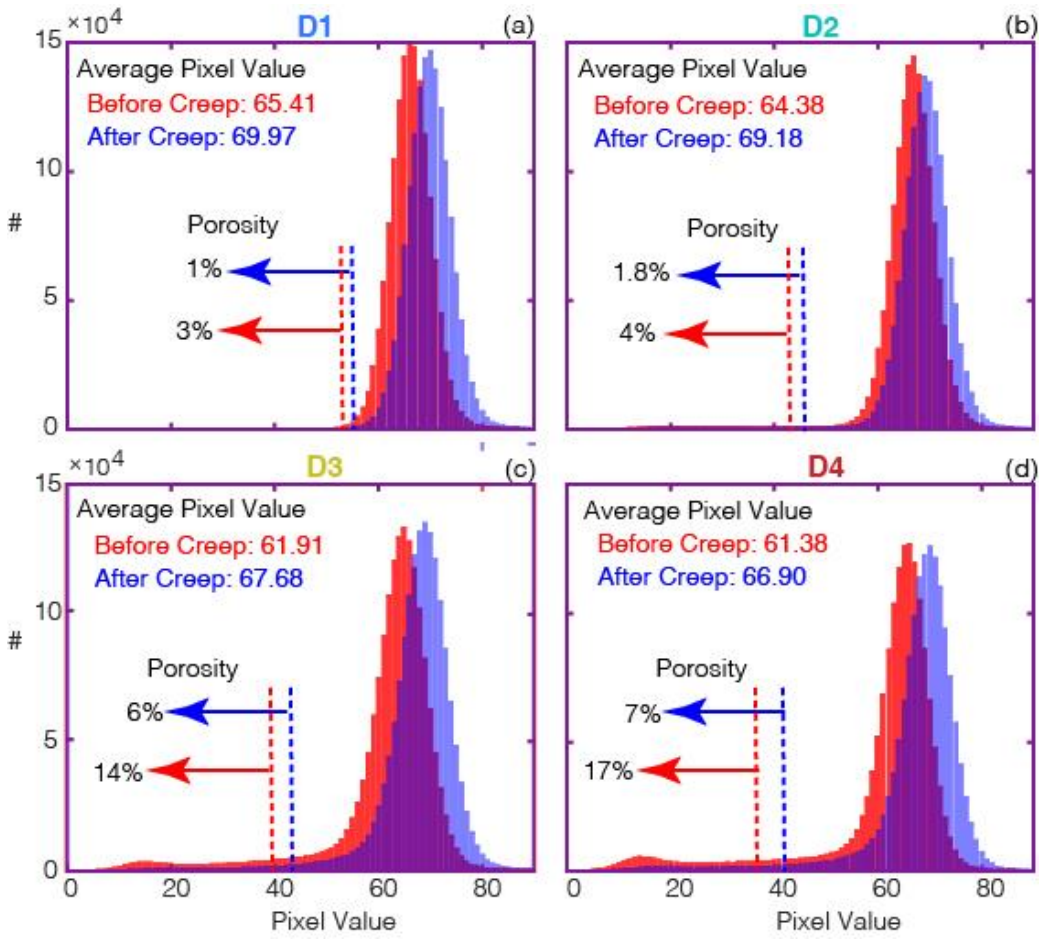

Figure 4.7. Pixel value histograms of D1, D2, D3, and D4 sandy siltstone specimens. The porosity of the sample is quantified by taking the average of the two bimodal distributions. (a) D1 histogram before and after creep experiments. (b) D2, (c) D3 and (d) D4 sample histograms before and after creep experiments. The average pixel value of the entire distribution is mentioned in each figure, which decreases with damage. For each sample, the average pixel value increases in healed specimens. Vertical dotted lines show the averages of each bimodal distribution. Porosity is calculated as the average of total number of pixels in the first modal distribution on the left of the vertical line to the total number of pixels in the entire image. The calculated porosity before and after each creep experiments is indicated in each figure.

4.3.4 Sandstone Creep Behavior and Microstructural Observations

Unlike siltstone specimens, sandstone specimens do not show monotonic increase in creep strain with increase in strain rate of impact. We observe more creep deformation in intact sandstone specimens than in samples impacted at lower strain rates: D1 and D2 (Figure 4.8a, b).

Creep strain decreased from D0 to D1 to D2. Conversely, the creep strains of D3 and D4 samples are higher than the creep strain of D0 (Figures 4.8a, b). In summary, creep decreases from D0-D1-D2 as (helium-based) porosity decreases but increases from D2-D3-D4 as damage increases. Axial and volumetric strain data show similar trends. Figure 4.8c shows that the creep strain diminishes with increase in differential stress. Creep strain is higher at 5 MPa differential stress than at 10 MPa differential stress. This behavior is analogous to the pressure dependent stiffening of siltstone.

Sandstone samples show a unimodal distribution of pixel numbers (Figure 4.8d, e, f, g); therefore, it is difficult to capture the fracture and matrix porosity by pixel thresholding. Instead, we qualitatively compare the porosity of the sample before and after creep by taking the average of the pixel values of the entire image. Since the pixel values correlate with the density of the material within the pixel, larger average pixel value represents lower porosity of the sample.

Average pixel value before creep is higher in D2 (51.74) than in D0 (51.17) and D4 (49.0) samples, implying lowest porosity of D2 sample. Lower average pixel value of D0 compared to D2 indicates higher porosity of D0, consistent with helium porosimeter measurements and creep observations which show more creep deformation in D0 than D2 (Figure 4.8b, e). D4 has lowest pixel value indicating more fracture volume creation at high strain rate of impact. Figures 4.8f and 4.8g also show the histograms of the healed D2 and D4 samples. The difference in average pixel value of the damaged and healed D2 (1.3) and D4 (3.2) samples is indicative of the porosity loss during the experiments. We observe that the difference in pixel values in D2 is lower than in D4, indicating more pore compaction in D4 sample.

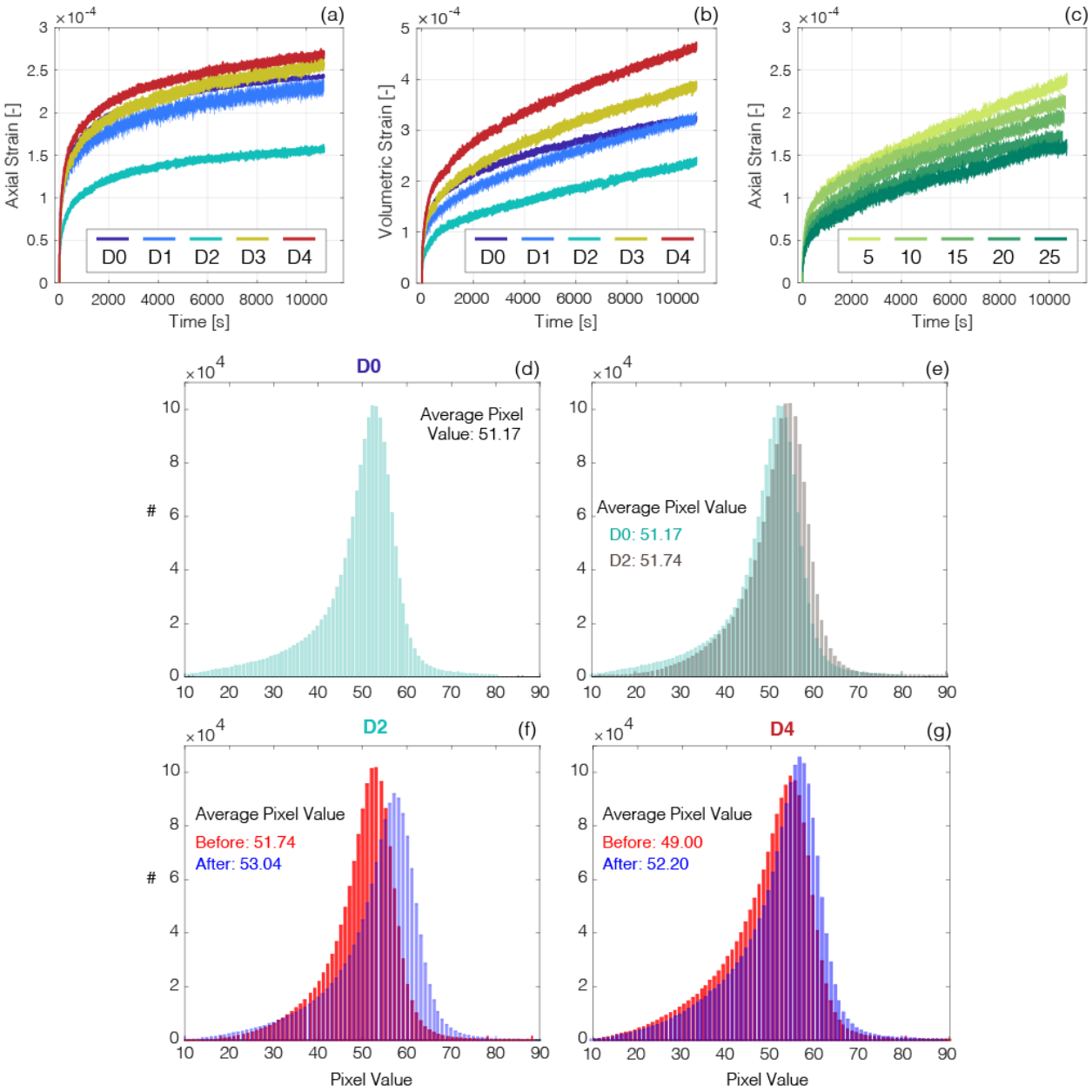

Figure 4.8. Summary of sandstone strain data and Micro-CT pixel values. (a) Axial creep strain and (b) Volumetric creep strain history for D0-D4 samples at 20 MPa differential stress magnitude. (c) Dependence of creep strain magnitude on differential stress magnitude. (d) Histogram of pixel values for a D0 sandstone CT slice. (e) Comparison of D0 and D2 pixel value histograms. (f) Comparison of D2 pixel histograms before and after creep experiments. (g) Comparison of D4 pixel histograms before and after creep experiments.

SEM images of D0, D2 and D4 sandstone specimens show that the grains are larger in size in sandstone compared to the sandy siltstone samples (Figure 4.9). We first compare the porosity and grain size of D0 (Figure 4.9a, b, c) and D2 samples (Figure 4.9d, e, f). D0 sample shows more void spaces (VS) between grains than D2. Comparison of grain contact (GC) between the larger grains in Figures 4.9b and 4.9e shows that the D0 sample has more contacts that are supported by small contact areas, whereas such contacts are not present in D2 due to the presence of crushed material. Although D2 samples also have spaces between the larger grains, those spaces are filled with crushed grains created by impact and reduce the porosity of the specimen. These observations explain why porosity decreases from D0 to D1/D2 samples despite the enhanced deformation due to the SHPB impact. At the low strain rates in the D1/D2 impacts, compaction occurs first to fill the large open pore spaces.

Next, we compare between D2 (Figure 4.9d, e, f) and D4 (Figure 4.9g, h, i). D2 and D4 samples have similar grain sizes with crushed grains filling the space between grains in both samples. However, the larger grains in D4 samples have more intragranular fractures than D2 contributing to the larger porosity (indicated as FG in Figure 4.9g, h, i). The fractured grains in D4 maintain the original grain boundary and rock fabric, like pulverized rock (Blenkinsop, 1991; Scholz, 2009). In summary, these SEM observations signify a transition from pore volume reduction by crushing of large-grain contacts during impact at low strain rates, to intragranular fracture volume creation at high strain rates that outweighs the compaction from contact crushing, consistent with the trends seen in the creep and micro-CT data.

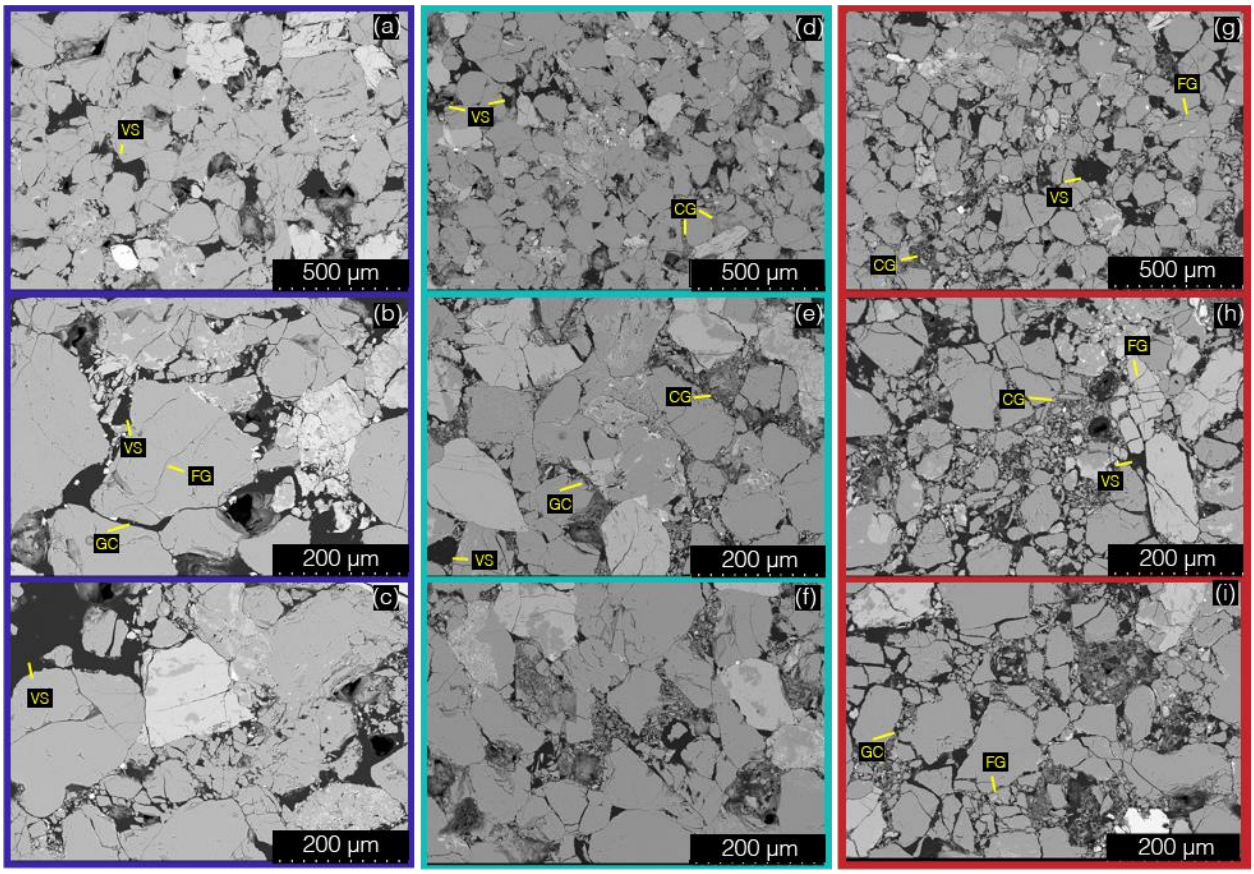

Figure 4.9. Scanning Electron Microscope images of sandstone specimens. (a, b, c) Sandstone D0, (d, e, f) Sandstone D2 and (g, h, i) Sandstone D4 samples. VS: Void space, FG: Fractured grains, GC: Grain contact, CG: Crushed grains.

4.4 Viscoplastic Modeling

4.4.1 Viscoplastic Model

We use the viscoplastic constitutive law proposed by Haghighat et al. (2020) which combines the Modified Cam Clay model (Wood, 1990) and Perzyna viscoplastcity (Perzyna, 1966) to analyze the elastic, inelastic, and creep behavior observed in the experimental data. The modified Cam-Clay model is an elasto-plastic strain hardening model that captures the essential aspects of soil behavior: strength, dilatancy, compaction and critical state. In the critical state of a material, the material can undergo distortion without any changes in stress or volume. Physically,

the critical state line is the boundary that separates brittle localized failure from distributed deformation. The critical state line is a straight line in the pressure-deviatoric stress plane, which passes through the origin and has a characteristic slope η, η being a material property (Figure 4.10a). η is comparable to friction in rock mechanics experiments and there exists a relationship between η and Mohr-Coulomb frictional angle ϑ (Chan and Zoback, 2002; Zoback, 2010).

$$\eta = \frac{6\sin\vartheta}{3-\sin\vartheta} \qquad (4.2)$$

While the critical state line separates distributed deformation from localized deformation, The modified Cam Clay (MCC) yield criterion delineates the elastic and plastic part of the deformation. The MCC yield surface is an ellipse in the pressure p- deviatoric stress q space (Figure 4.10). The size of the yield surface is dependent on the yield stress of the material (Schofield and Wroth, 1968). Strain hardening is when an increasing stress is required for additional plastic deformation to accumulate. When the material is compacted by increasing stress, as in strain hardening, the MCC yield envelope increases in size, i.e., more stress is required for a compacted material to reach the yield envelope (Figure 4.10b). The yield envelope which expands or shrinks in the *p*-*q* space can be written mathematically as:

$$F = \frac{q^2}{\eta^2} + p(p - p_y) \qquad (4.3)$$

In the above equation, F is the yield function and p_y is the yield stress. When F becomes positive, the yield envelope expands, as p_y also increases, but otherwise neither expands nor contracts if F is zero or negative.

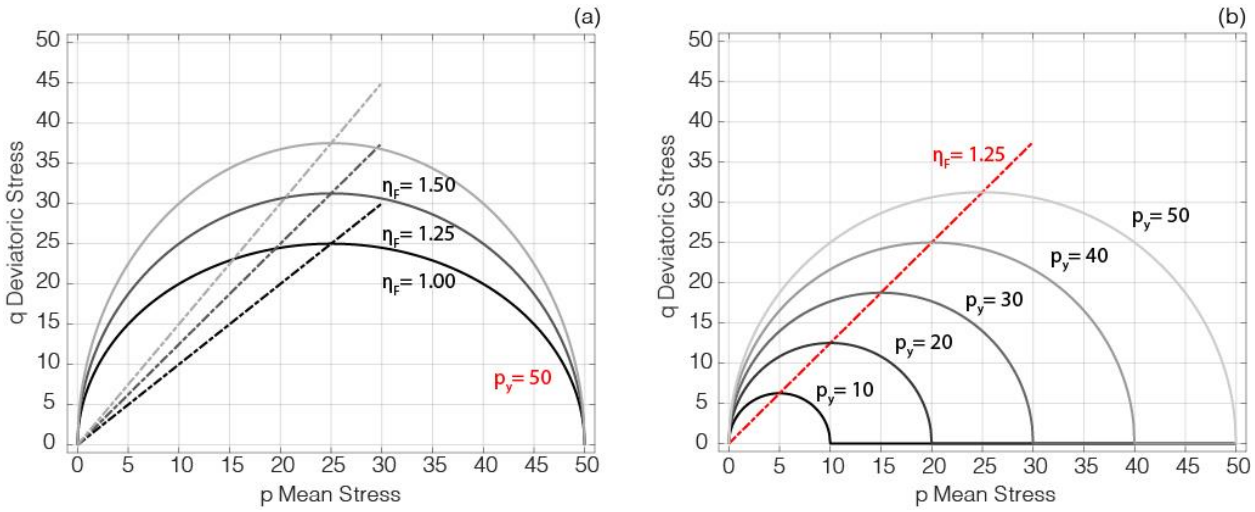

Figure 4.10. (a) Yield envelope in the p-q space for various slopes of critical state line at constant yield stress magnitude (p_y) of 50 MPa. (b) Change in yield envelope with change in magnitude of p_y at constant η.

Since we aim to observe pore volume change due to creep compaction, pore volume change is another important aspect of this model. One way to quantify pore volume in porous and low cohesion materials is by using void ratio, the ratio of pore volume to material volume. During soil mechanics experiments of compression and swelling, it is observed that void ratio has a linear relationship with logarithm of the pressure during loading and unloading (Wood, 1990). Since loading involves both elastic and plastic deformation, the slope of the straight line in void ratio-log mean stress plot is different than that of the slope of the unloading line in the void ratio-log mean stress plot, where deformation is elastic (Figure 4.12a). The loading line and unloading lines in the void ratio-log pressure space are widely known in the soil mechanics literature as the isotropic compression line and swelling line, respectively, given by:

$$\mathrm{d}e = -\lambda\, \mathrm{d}(\ln p) \tag{4.4}$$

$$\mathrm{d}e^{e} = -\kappa\, \mathrm{d}(\ln p) \tag{4.5}$$

Where e is the void ratio and e^e is the elastic portion of void ratio. The loading and unloading slopes are denoted as λ and κ, respectively. The negative sign in front of λ and κ in Equation 4.4 and 4.5 indicates that void ratio decreases with increase in applied pressure. Figure 4.12a shows typical soil behavior during loading and unloading. Isotropic compression lines (solid lines) at various λ values show that with increasing λ, void ratio change is more for the same change in pressure. Similarly, the swelling lines (dashed lines) show more void ratio change with increase in κ value.

Assuming total strain to be the sum of the elastic and plastic portions of the deformation, we can use Eq. 4.4 and 4.5 to write yield stress as a function of volumetric plastic strain (ε_v^p), λ and κ.

$$\mathrm{p_y} = \mathrm{p_{y0}} \exp\left(\frac{1+\mathrm{e_0}}{\lambda-\kappa}\,\varepsilon_\mathrm{v}^\mathrm{p}\right) \qquad (4.6)$$

p_{y0} describes the pre-consolidation stress of the material, or the maximum stress that the sample has undergone, whereas e_0 is the initial void ratio. Figure 4.11a shows how p_{y0} determines the initial yield stress magnitude above which plastic strain develops. With increase in p_{y0}, not only does the initial yield stress increase but the rate of increase in yield stress with plastic strain is also higher.

According to this model, at constant p_{y0} and e_0, the difference between λ and κ also determines the rate of increase in yield stress (Figure 4.11b). Rate of change in yield stress with plastic strain increases with decrease in $(\lambda - \kappa)$. On the other hand, with increasing initial void ratio, the rate of change in yield stress with plastic strain increases (Figure 4.11c). Therefore, a combination of these parameters determines the yield stress of the material, which in turn determines the size of the MCC yield envelope, as shown in Figure 4.10b.

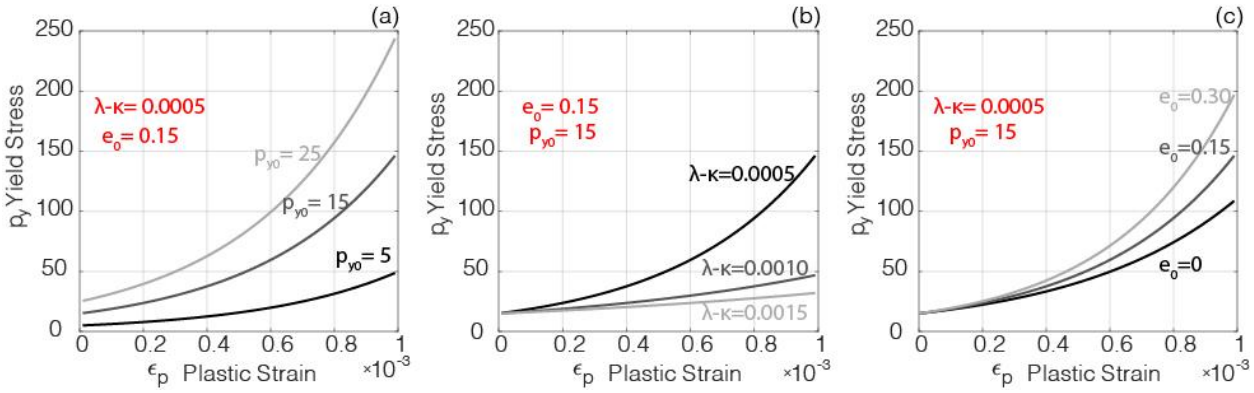

Figure 4.11. Influence of various parameters on yield stress-plastic strain relationship. Influence of (a) p_{y0}, (b) λ and κ, and (c) initial void ratio e_0 on yield stress magnitude.

Once we define the yield envelope with respect to the current state of stress, we can define the elastic and plastic strain. The elastic response of the material is described by combining the equation for swelling line (Eq. 4.4) with the definition of strain in large deformation in terms of deformation gradient. To express the non-linear elastic part of the deformation, pressure dependent bulk modulus is expressed in terms of void ratio and κ (Haghighat et al., 2020).

$$\mathrm{K} = \frac{1+\mathrm{e}}{\kappa}\mathrm{p} \qquad (4.7)$$

Where K is the pressure dependent bulk modulus and indicates pressure dependent stiffening of the material. κ is inversely proportional to K because higher κ indicates a more compliant material (Figure 4.12a)

An energy-based definition of strain hardening, and softening was proposed by Drucker, also called the Drucker Inequality (Drucker, 1950). The Drucker Inequality states that for a single stress component, the conjugate plastic strain rate satisfies $\dot{\sigma}\dot{\varepsilon^p} \geq 0$ for work hardening material. The inequality is unchanged if the stress and strain rates are multiplied by an infinitesimal time to get the same forms as $d\sigma d\varepsilon^p \geq 0$ for work hardening material. This product has the dimensions

of work per unit volume. Since the elastic component of strain can never be zero or negative for work hardening materials, we can write the work hardening equations as $d\sigma d\varepsilon > 0$ and $d\sigma d\varepsilon^p \geq 0$. These two inequalities also work for perfectly plastic material where $d\sigma = 0$. They become $d\sigma d\varepsilon^p = 0$; but $d\sigma d\varepsilon > 0$. For work softening materials, since $d\sigma < 0$, and $d\varepsilon^p < 0$; $d\sigma d\varepsilon^p \geq 0$ holds. This common inequality $d\sigma d\varepsilon^p \geq 0$ for work hardening, work softening, and perfectly plastic materials suggests that the work done due to plastic deformation is always non-negative, also the basis for the postulate of maximum plastic dissipation (Simo and Hughes, 2006). Solving the principle of maximum plastic dissipation for a viscosity (μ) based Perzyna formulation, the equation for plastic strain rate is obtained.

$$\dot{\varepsilon}_v^p = \frac{1}{\mu}\frac{1}{p}\left(\frac{q^2}{\eta^2} + p(p - p_y)\right)(2p - p_y) \qquad (4.8)$$

Where $\frac{1}{p}\left(\frac{q^2}{\eta^2} + p(p - p_y)\right)(2p - p_y)$ is overstress and μ is viscosity.

Viscosity μ is the only unknown parameter in the above formulation. Here we assume viscosity as an exponential function of volumetric plastic strain (Haghighat et al., 2020).

$$\mu = \mu_0 \exp(\zeta\, \varepsilon_v^p) \qquad (4.9)$$

Where μ_0 and ζ are material constants. μ_0 indicates the reference viscosity of the specimen, i.e., the viscosity of the sample at zero plastic strain or the viscosity at time step 0 of the analysis, whereas ζ is the rate of change in viscosity with change in plastic strain. We evaluate the effect of change in μ_0 and ζ on μ with Figures 4.12b and 4.12c. At constant ζ, increase in μ_0 not only increases the initial viscosity but also increases the rate of viscosity increase with plastic strain

(Figure 4.12b). Figure 4.12c shows that at constant μ_0, ζ determines the rate of increase in viscosity.

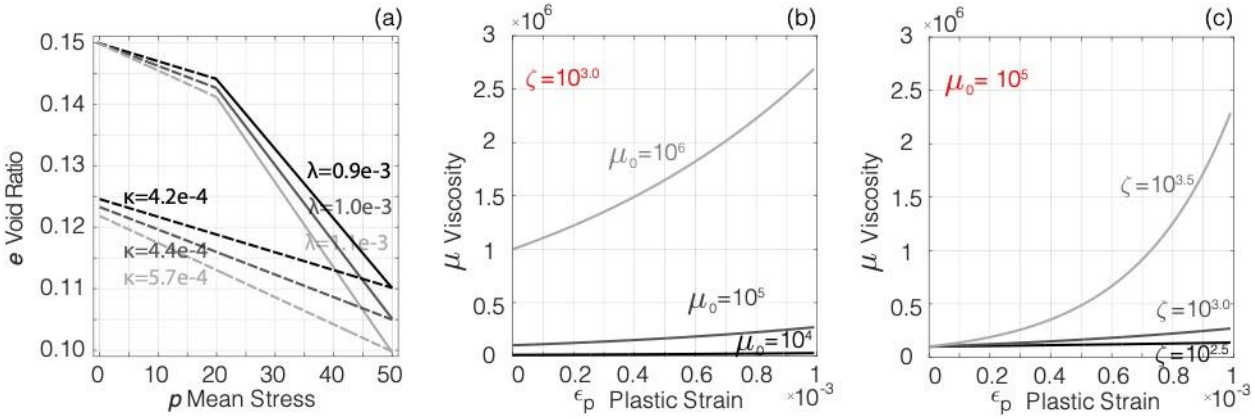

Figure 4.12. (a) Change in void ratio with mean stress for various isotropic compression and swelling lines. Compliant materials have higher λ and κ. (b) Viscosity evolution with plastic strain with changing reference viscosity μ_0. (c) Viscosity evolution with plastic strain with changing viscosity rate ζ.

We make one modification to the viscoplastic formulation proposed by Haghighat et al. (2020). We find from regression of the experimental data using the original formulation that it fits the experimental data to some extent but fails to reproduce the rapidly diminishing plastic strain rate towards the beginning of the creep stage. To this end, we introduce a power *n* to the plastic strain rate equation (Equation 4.8) to allow higher strain rates at the beginning of the creep stage (Figure 4.4d-f). The modified form of plastic strain rate in terms of viscosity is:

$$\dot{\varepsilon}_v^p = \frac{1}{\mu}\left[\frac{1}{p}\left(\frac{q^2}{\eta^2} + p(p - p_y)\right)(2p - p_y)\right]^n = \frac{\text{overstress}^n}{\mu} \qquad (4.10)$$

The overstress exponent modifies the unit of viscosity from MPa.s to MPa^n.s. An *n* value greater than 1 signifies higher plastic strain rate at same overstress magnitude. '*n*' or overstress exponent is motivated from dislocation and diffusion creep mechanism dependent stress exponents

(Scholz, 1968; Tsenn and Carter, 1987).

4.4.2 Obtaining viscoplastic parameters from lab data

We use a finite difference method to model the triaxial stage of the experiment. Plastic strain is calculated at each time step by multiplying the plastic strain rate (calculated from Eq. 4.10) by a finite time difference followed by adding the plastic strain calculated at previous time steps. For this calculation, plastic strain is assumed to be zero at the beginning of the experiment for simplicity. The plastic strain obtained at each time step is added to the elastic strain (calculated from Eq. 4.4) to calculate the total strain. For a set of input λ, κ, μ_0, ζ, e_0, p_{y0}, η, and n we can calculate the strain and strain rate magnitudes using the above formulation.

We constrain the initial void ratio e_0 from the initial porosity of the sample. Details of porosity calculation are discussed in Section 4.2.4. We also constrain η from Equation 4.1 by assuming the coefficient of internal friction to be 0.6 for all the samples. Haghighat et al. (2020) shows that changing η value does not have a significant effect on the results, therefore, we do not vary η or coefficient of internal friction to reduce the degree of freedom in the regression analysis. We also have better physical understanding of this parameter from the literature compared to other parameters in the model.

The other parameters λ, κ, μ_0, ζ, p_{y0} and n are constrained by fitting the total model volumetric strain to the experimental volumetric strain data. The fitting is done by minimizing the cost function ϕ:

$$\phi = \sqrt{\frac{\sum_{i=1}^{N}(\varepsilon_i^{model} - \varepsilon_i^{data})^2}{T}} \qquad (4.11)$$

The cost function is defined as the square root of the average of the residual squared, where ε_i^{model} and ε_i^{data} are the modeled strain and experimental strain data at time step i, respectively. N is the number of data points. We take the root mean square of the residual such that the unit of cost function is maintained in units of strain. Further details on cost function calculation are discussed in Section 4.7.2.

To study the effect of time step size on the finite difference approach, we run the forward model at different time steps of 0.01, 0.05, 0.1, 0.5, and 1 second. We take the root mean square difference between each of the time step results as compared to the 1 sec timestep result. The root mean square difference of 0.01, 0.05, 0.1, and 0.5 timestep results from 1 second timestep result are 0.4, 0.35, 0.29, and 0.056%, respectively, of the total strain magnitude. These results suggest that the results converge asymptotically as the time step becomes finer in logarithmic scale, and the difference with the 1 second result is less than 1% of the strain value. Thus, we consider the time step of 1 second to be appropriate to investigate how the optimized constitutive parameters vary between laboratory results.

4.4.3 Range of optimized parameters

We evaluate the convergence of the cost function by varying the initial guesses of the parameters in a gridded pattern. The result is considered to be converged when it meets the limiting criterion (See section 4.7.1 for details). For different initial parameters, the converged cost function value varied. The optimized parameters also varied: λ, κ and p_{y0} show less variation compared to μ_0, ζ and n. Histograms of converged parameters show the range of magnitudes of optimized parameters for a siltstone specimen (Figure 4.13). Such variation in cost function and optimized parameters indicates that the solution is non-unique and various combinations of visco-plastic parameters can fit the stress-strain and strain-time plots. Thus, we

study the tradeoff between the optimized parameters in the subsequent section to constrain some of the parameters. The experimental and simulated results for minimum cost function are shown in Figures 4.14 and 4.15.

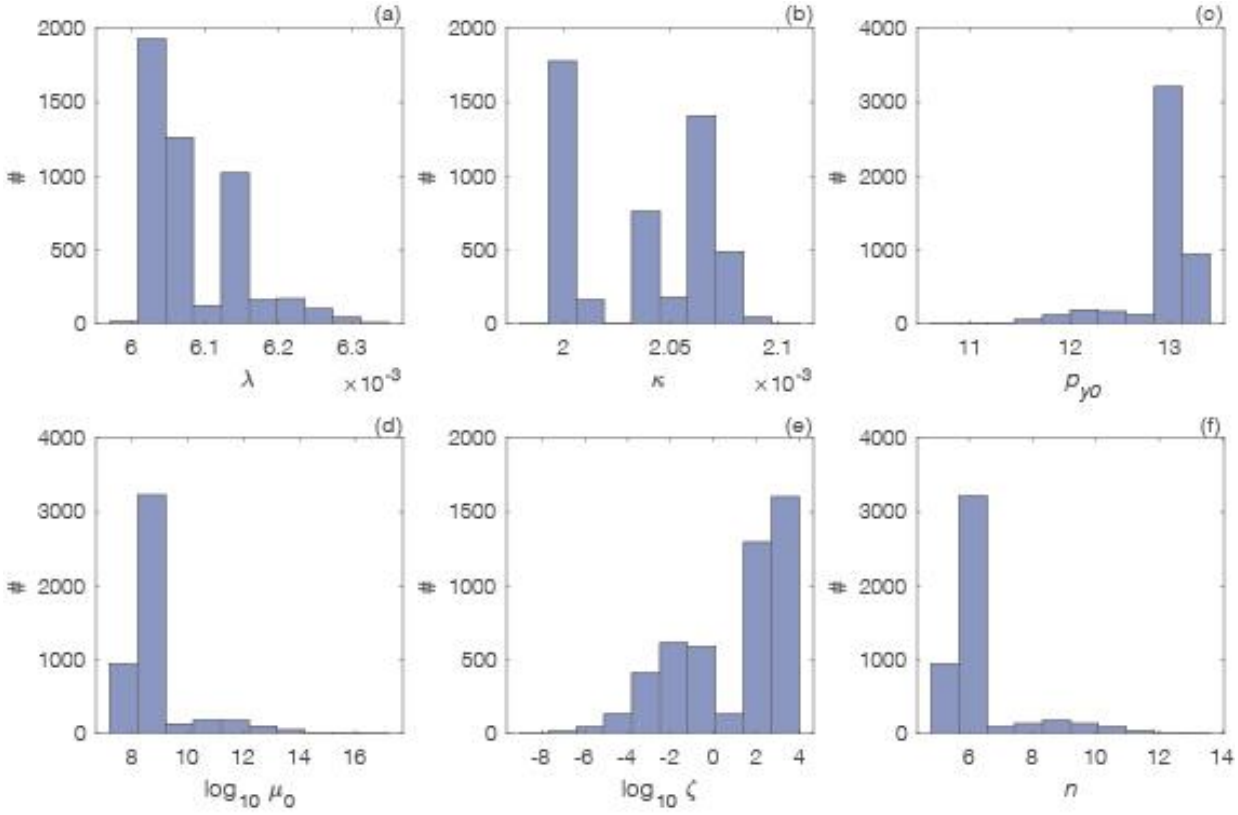

Figure 4.13. Optimized parameter histograms for (a) λ, (b) κ, (c) p_{y0}, (d) log 10 μ_0,(e) log 10 ζ and (f) n.

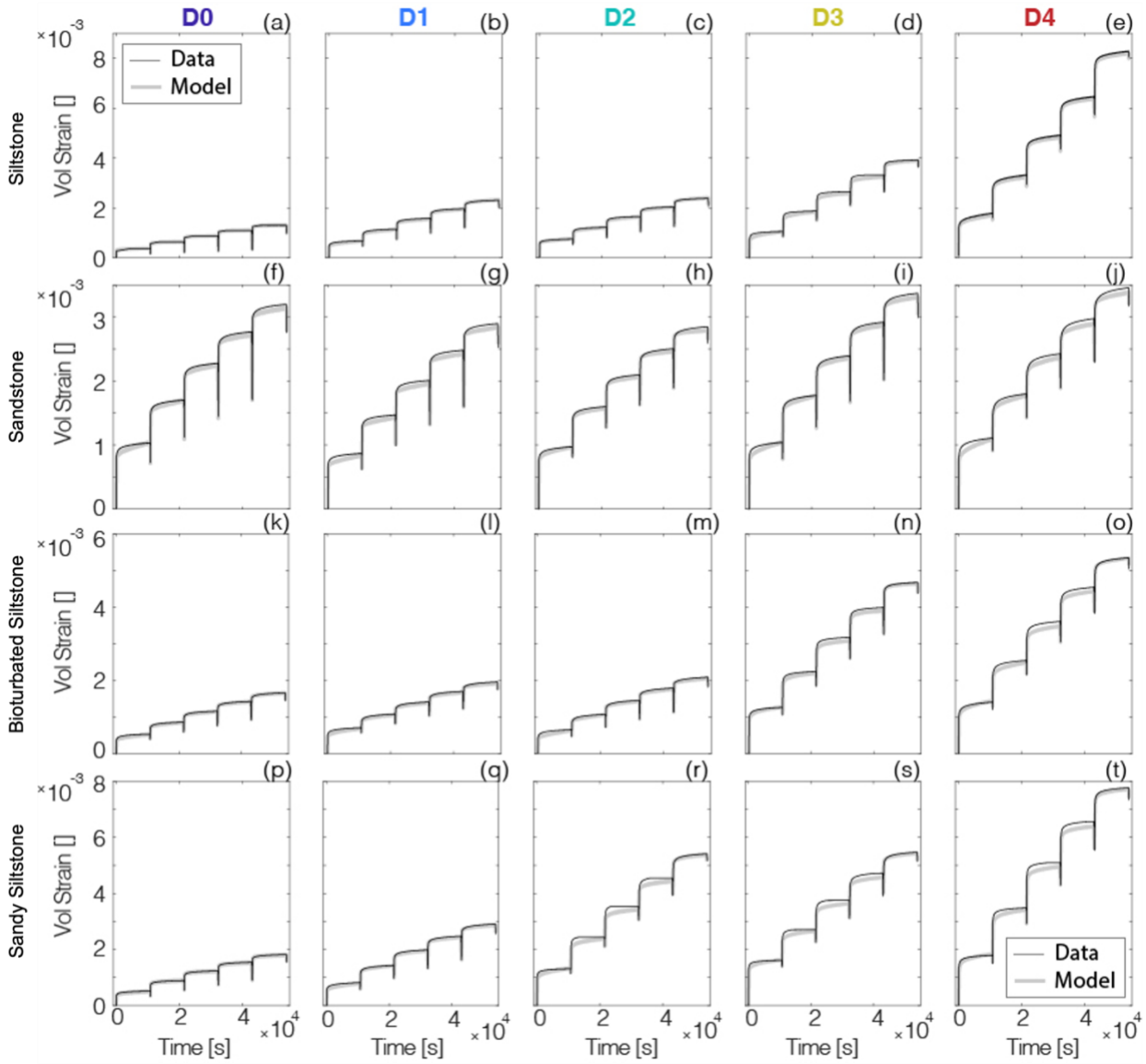

Figure 4.14. Time- volumetric strain plots for comparison of experimental data and viscoplastic model results. (a-e) Siltstone, (f-j) Sandstone, (k-o) Bioturbated siltstone and (p-t) Sandy siltstone samples. Gray is the experimental data and black is the modeled data.

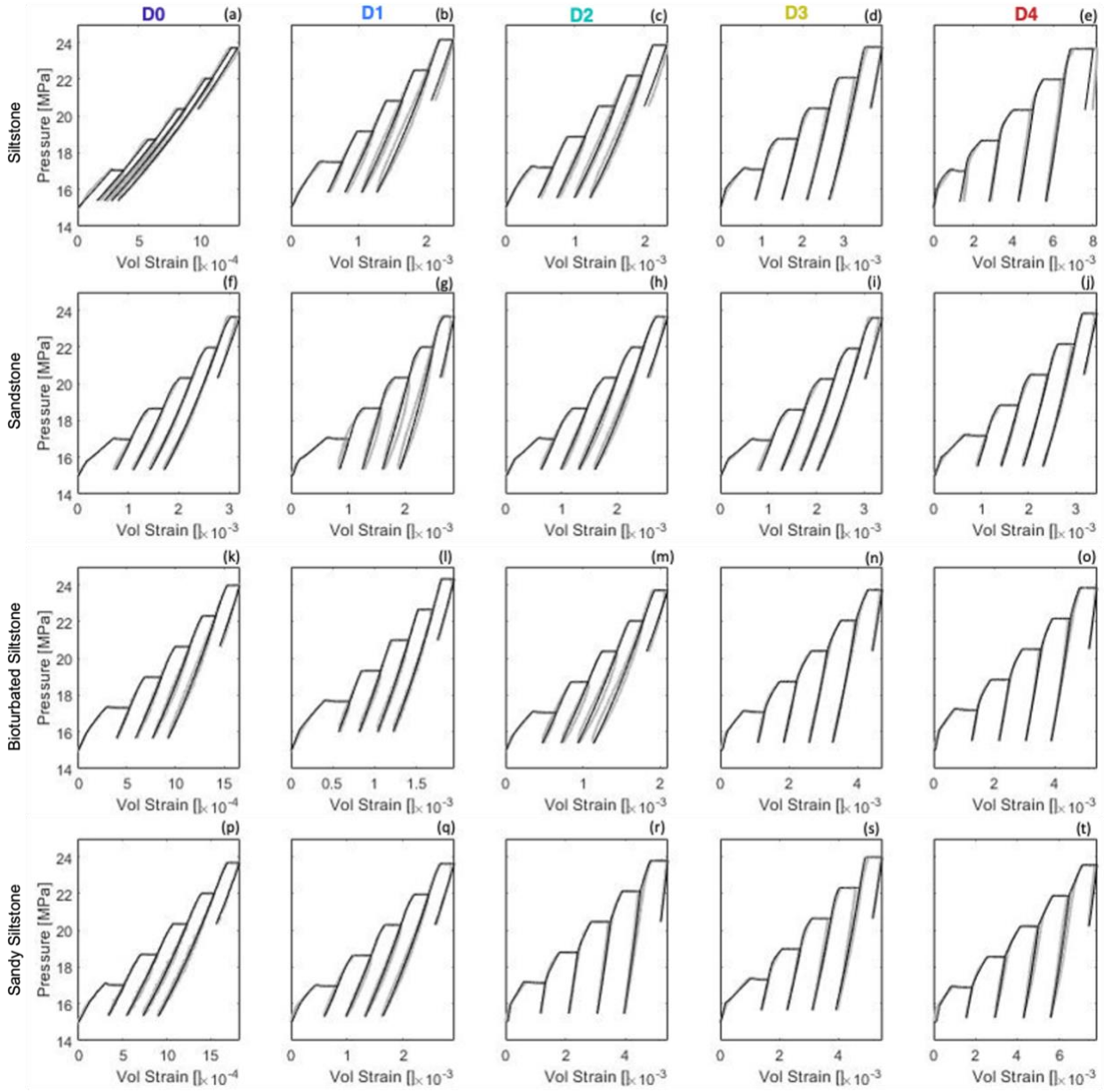

Figure 4.15. Volumetric strain- pressure plot for comparison of experimental data and viscoplastic model results. (a-e) Siltstone, (f-j) Sandstone, (k-o) Bioturbated siltstone and (p-t) Sandy siltstone samples. Gray is the experimental data and black is the modeled data.

4.4.4 Tradeoff between parameters

The lack of convergence into a unique model is primarily due to the tradeoff between parameters.

4.4.4.1 Tradeoff between $\boldsymbol{\zeta}$ and $\boldsymbol{n}$

Increasing the power law exponent, *n*, increases the rate of creep deformation per overstress, as can be seen by Equation 4.10. Increasing n also promotes, in a relative sense, more creep at high overstress (i.e., at the end of loading and initial part of the creep deformation) compared to when overstress is low. To keep the magnitude of the modeled plastic creep strain at the observed level, increase in *n* is compensated by the increase in viscosity to suppress the magnitude of creep. Therefore, n and rate of viscosity change ζ have a positive tradeoff. Since ζ and μ_0 has a positive correlation for $\zeta \geq 10^2$ (Section 4.4.4.2), μ_0 in turn has a positive correlation with n (Figure 4.16c).

4.4.4.2 Tradeoff between $\boldsymbol{\mu_0}$ and $\boldsymbol{\zeta}$

There is a tradeoff between reference viscosity μ_0 and rate of viscosity change ζ (Figure 4.16a). At ζ value less than 10^2, μ_0 is independent of ζ. At higher ζ values, μ_0 has a positive correlation with ζ. Figure 4.16a shows this tradeoff for a D3 siltstone specimen.

Creep strain magnitude observed in these rocks at the end of the experiment is in the order of 10^{-3} (Figure 4.4). Therefore, the magnitude of $exp(\zeta \varepsilon_v^p)$ at the end of the experiment is approximately equal to 1 for $\zeta \leq 10^2$ (Equation 4.9). When $exp(\zeta \varepsilon_v^p)$ is approximately equal to 1, viscosity evolution is negligible. This shows why the reference viscosity μ_0 is constant at ζ values below 10^2; hardly any viscosity change is occurring, thus the viscosity throughout the experiment is governed by μ_0 and insensitive to ζ. Conversely when $\zeta \geq 10^2$, there is appreciable increase in viscosity during the experiment and the value of $exp(\zeta\ \varepsilon_v^p)$ increases significantly with increasing ζ. When $exp(\zeta \varepsilon_v^p)$ increases, μ_0 increases simultaneously to fit the creep part of the deformation. Or in other words if μ_0 is high, ζ increases at a faster rate to

increase $exp(\zeta \varepsilon_v^p)$ and fit the creep part of the deformation. This explains the positive tradeoff of μ_0 and ζ when $\zeta \geq 10^2$.

4.4.4.3 Tradeoff between $\boldsymbol{\mu_0}$ and $(\boldsymbol{\lambda - \kappa})$ as well as between $\boldsymbol{\mu_0}$ and $(\boldsymbol{\lambda - \kappa})$

We observe a negative correlation between μ_0 and p_{y0} magnitude but a positive correlation between μ_0 and $(\lambda - \kappa)$ in Figures 4.16b and 4.16d, respectively. To maintain the same plastic strain rate with increasing μ in Equation 4.10, the magnitude of $[overstress^n]$ must increase. The magnitude of $[\frac{1}{p}\left(\frac{q^2}{\eta^2} + p(p - p_y)\right)(2p - p_y)]^n$ can increase by increasing n or by decreasing the yield stress p_y. In Equation 4.11, a decrease in p_y can be achieved by a decrease in p_{y0} and/or an increase in $(\lambda - \kappa)$, as also shown in Figure 4.11. Therefore, we notice a tradeoff between μ_0 with p_{y0} and $(\lambda - \kappa)$.

4.4.4.4 Function value

In section 4.4.5.1, we describe how the tradeoff between μ_0 and ζ is dependent on whether the magnitude of ζ is above 10^2 or below 10^2. Plots of μ_0 and ζ color coded by ϕ show that the magnitude of ϕ is lower at at high zeta values as compared to low zeta values (Figure 4.16a). The results at low ζ are termed Type 1 results, whereas the results at high ζ values are termed Type 2 results and discussed further in 4.5.2.

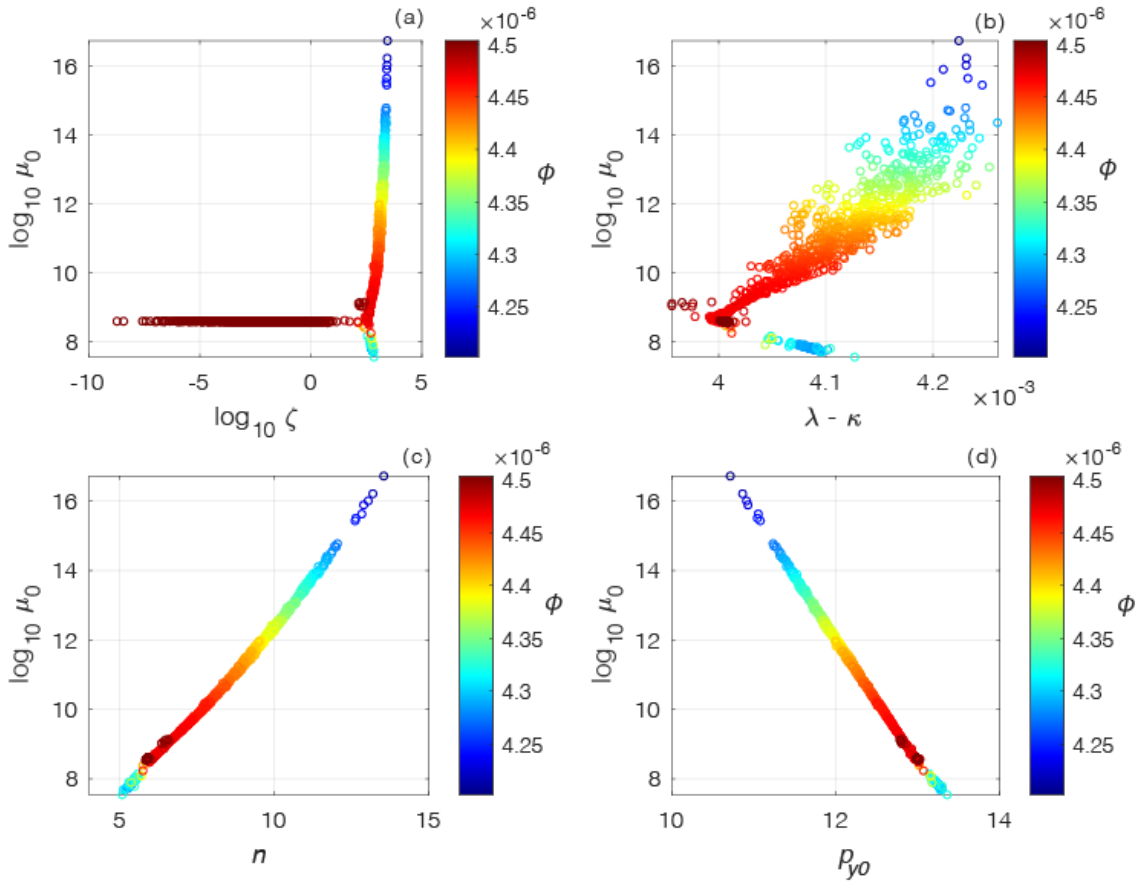

Figure 4.16. Tradeoff between parameters for a D3 siltstone specimen. a) μ_0 and ζ color coded by cost function ϕ, b) μ_0 and $(\lambda - \kappa)$ color coded by ϕ, c) μ_0 and n color coded by ϕ, d) μ_0 and p_{y0} color coded by ϕ.

4.4.5 Results for constant $\boldsymbol{n}$ and constant $\boldsymbol{p_{y0}}$

n contributes to the relative distribution of plastic strain during high overstress periods (i.e., loading and the initial part of creep deformation) to low overstress periods, but because of the tradeoff between μ_0 and n, we are unable to find unique values of μ_0 and n. Hence, we apply bounds on overstress exponent n to facilitate comparison of parameters between samples. We limit n to integers 1-6. Although the exact creep mechanism is unknown to us, the stress exponent observed from creep tests on various rock types range from 1-6 (Carter and Tsenn,

1987; Table 4.2), caused by grain boundary migration, grain boundary sliding, dislocation creep and/ or sub-grain formation.

Since the maximum stress that the sample undergoes during the confining pressure stage is 15 MPa, we expect the p_{y0} magnitude to be ≤15. Thus, we also fix p_{y0} to 12 MPa for the subsequent optimization.

At constant n and p_{y0}, the function value converges to a single number, irrespective of the initial parameter guesses of the other parameters. Unlike section 4.4.3, the optimized visco-plastic parameters also do not show a range of values, implying better convergence of the model. The optimization fits the intact sample data at an n value of 1 but fails to fit the damaged specimens. With increasing n, all samples including the most damaged sample are fitted better. The value of ϕ also decreased with increase in n. Therefore, we show the optimized results for n value of 6 in Table 4.2 to allow comparison of the optimized results between different samples. We note that at n=6, the cost function value is higher than when n is allowed to vary. Nonetheless, because of the better convergence of the results at constant n and p_{y0}, we use these results for further interpretation.

Table 4.2. List of optimized parameters for constant p_{y0} *of 12 MPa and constant* n *of 6.*

Damage	**λ**	**κ**	**μ_0**	**ζ**
Siltstone				
D0	0.0028	0.0014	10.3195	4.0633
D1	0.0032	0.0014	10.0269	3.9958
D2	0.0052	0.0018	9.9404	3.0580
D3	0.0060	0.0021	9.9562	3.0428
D4	0.0070	0.0022	9.3161	2.9087

Bioturbated Siltstone				
D0	0.0031	0.0018	10.3518	3.9837
D1	0.0049	0.0023	9.9840	3.7695
D2	0.0072	0.0021	10.0900	2.9019
D3	0.0080	0.0024	9.9114	2.8202
D4	0.0100	0.0032	9.4265	-9.27
Sandy Siltstone				
D0	0.0027	0.0021	11.2962	4.5658
D1	0.0039	0.0022	10.8847	3.8902
D2	0.0038	0.0021	10.6478	3.8187
D3	0.0053	0.0026	10.3318	2.9938
D4	0.0120	0.0033	10.1896	2.6653
Sandstone				
D0	0.0059	0.0029	8.3752	3.9498
D1	0.0046	0.0025	8.7881	3.7896
D2	0.0053	0.0017	8.2390	3.9336
D3	0.0059	0.0025	8.6620	3.8296
D4	0.0050	0.0019	8.9107	3.6034

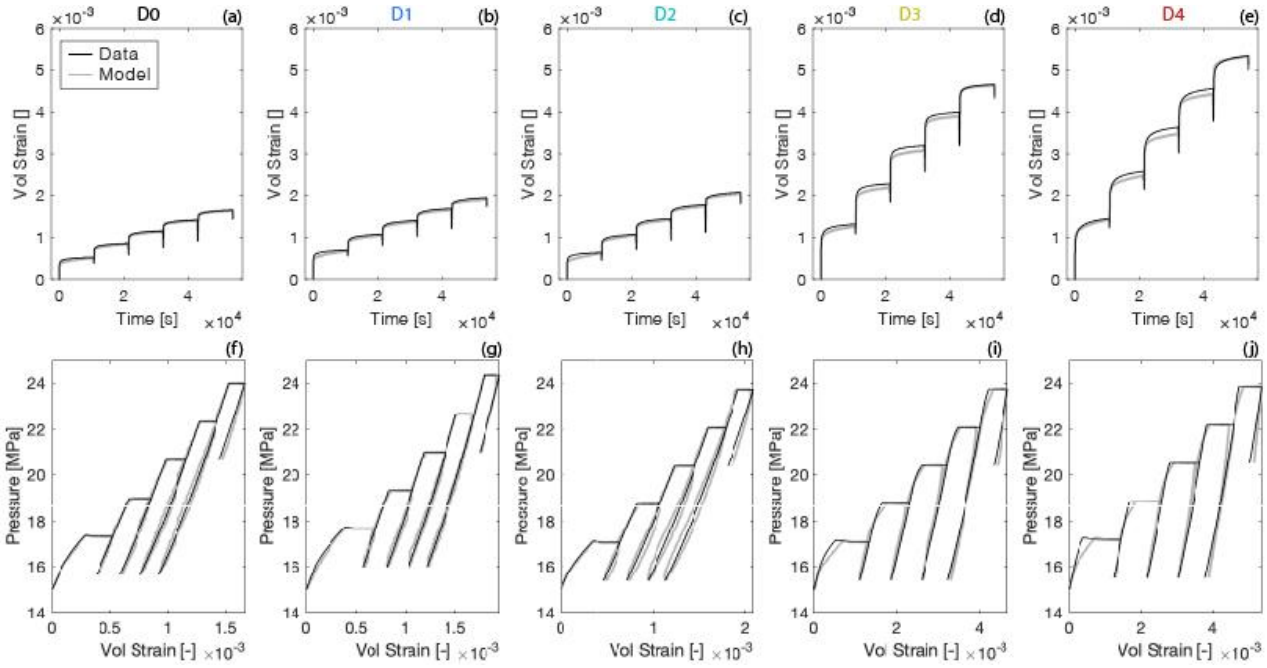

Figure 4.17. (a-e) Pressure-Volumetric Strain and (f-j) Strain history of damaged siltstone specimens at constant n and p_{y0}.

4.4.6 Viscoplastic parameters with damage

The slope of the isotropic compression line and swelling line (i.e., λ and κ) increases with damage. λ increases when there is more void ratio change with the same change in pressure. Thus, λ increases with damage as the damaged samples show more void volume loss relative to undamaged samples. Siltstone, bioturbated siltstone and sandy siltstone varieties in Figure 4.18a show that trend. Optimization results also show that κ is higher in damaged specimens, because they deform more elastically than undamaged specimens with the same change in pressure (Figure 4.18b).

On the other hand, the magnitudes of μ_0 and ζ decrease with damage (Figure 4.18c, d). What is believed to facilitate the plastic creep strain is the sliding and/or closing of microcracks. Undamaged samples and less damaged samples strain more slowly because there are not many

fracture planes that can accommodate the rock deformation, hence μ_0 is higher. A damaged sample, however, has many microfractures that enhances the creep strain rate per applied stress, hence lower μ_0.

We do not observe a monotonic trend in the sandstone specimens. This may be due to the complicated nature of sandstone damage where compaction dominates at low strain rate and dilatant damage creation at high strain rate.

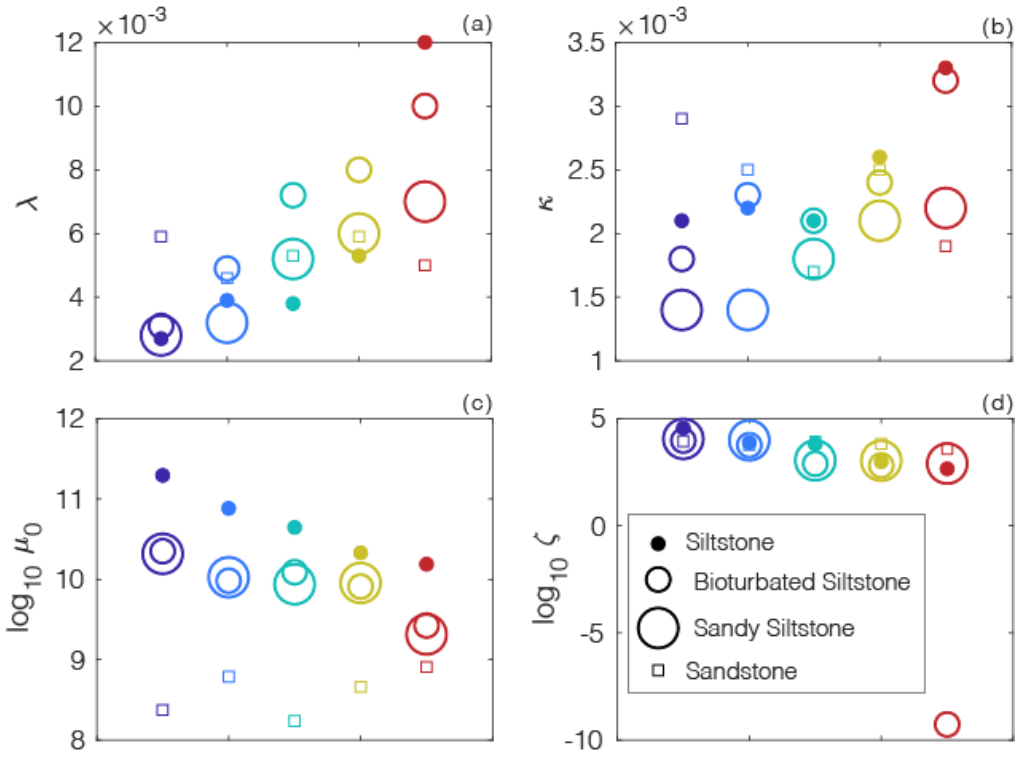

Figure 4.18. Optimized parameters plotted with damage a) λ, b) κ, c) μ_0, and d) ζ.

4.5 Discussion

4.5.1 Fracture closure at all scales

The microstructures of samples show fractures at various scales. The macroscopic fractures present in the sample are visible in the hand-specimen scale and in micro-CT

observations. The micro-CT images before and after creep experiments show closure of fractures during the experiment which pass through the entire sample (i.e. 1 inch in length) to fractures which are 10-100s of microns in extent (Figure 4.6).

SEM images (Figure 4.9h, i) show regions of grain-size reduction (Figure 4.6c, d), indicative of crushing of grains at all scales. The SEM images also show the presence intragranular fractures, grain-boundary, and matrix fractures as well as long inter-granular fractures which coalesce to form regions of deformation. Although we do not have SEM images before and after creep experiments, similar observations in post-creep SEM and micro-CT images suggest that crack closure occurs at all scales. The volumetric deformation is accommodated by closure of fractures of all sizes.

4.5.2 Type 1 and Type 2 results

Based on the Perzyna-MCC model with a varying exponent of overstress, viscosity evolves differently for Type 1 and Type 2 results. For Type 1, the initial apparent viscosity is low and there is hardly any viscosity change during the experiment (Figure 4.19a). Conversely, in Type 2, the initial apparent viscosity is high, and the range of viscosity change spans several orders of magnitude (Figure 4.19b). Because of these variations in viscosity, the Perzyna-MCC model yields different overstress histories to produce the same amount of creep strain.

As shown in figure 4.16, Type 2 results generally yield smaller ϕ values, thus indicative of being a better representation of the constitutive behavior. The difference in ϕ between the Type 1 and Type 2 results are small, less than about 5%. Thus Type 1 and Type 2 results may both be plausible descriptions of constitutive behavior, although the model cannot clearly distinguish which behavior is a better physical representation. Figures 4.19a and b show that creep deformation will continue at a specified stress longer in Type 2 as compared to Type 1 as

overstress is consumed at a slower rate in Type 2. According to Type 2 results, μ_0 and overstress magnitude increase at high stress magnitude, therefore the sample can undergo significant creep deformation beyond the 3 hours hold stage. The time duration of creep remains an active field of research and many experiments have compared short-term and long-term creep of same rock type (Rassouli and Zoback, 2018) to understand permanent plastic strain after the hold stages. Our experiments are however limited to only 3-hour creep and cannot capture the long-term trend.

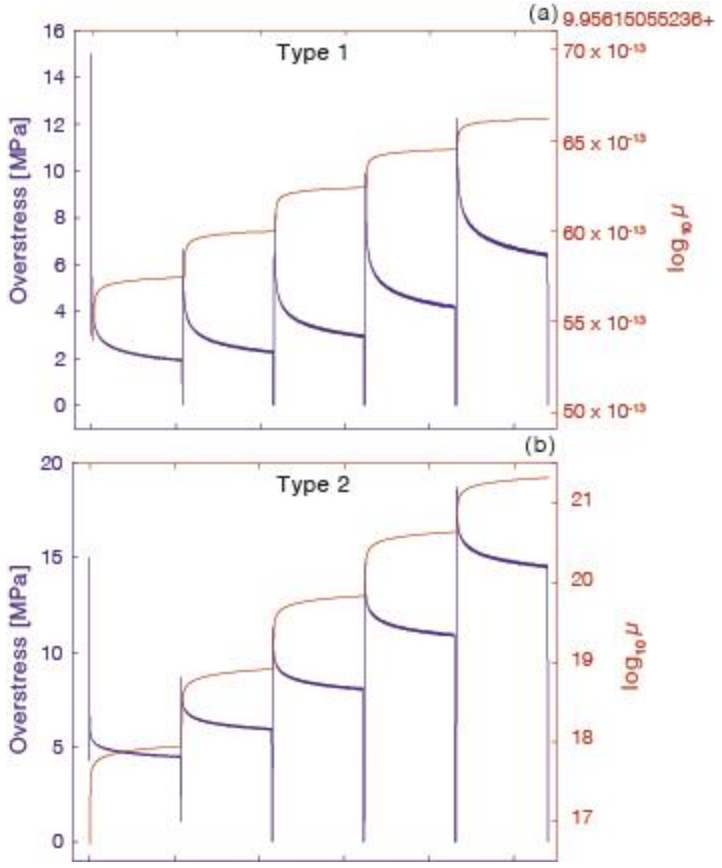

Figure 4.19. Comparison of overstress and viscosity evolution for a) Type 1, and b) Type 2 constant n and constant p_{y0}.

4.5.3 Damage induced changes in overstress and viscosity history

From the Perzyna-MCC law at constant n and p_{y0},we obtain the overstress, viscosity, yield stress and modulus evolution during the experiment. The evolution of these parameters is plotted in Figure 4.20 for all bioturbated siltstone specimens to compare between various degrees of damage. The overstress history shows that at the beginning of the triaxial stage, every sample reached the same overstress magnitude of ~15 MPa (Figure 4.20a). This is because the applied confining pressure at the beginning of the triaxial stage is 15 MPa (stress history in Figure 4.1a). During the hold stage, overstress decreases at a slower rate in an intact sample than in a damaged sample (Figure 4.20a) to fit the higher creep deformation in a damage sample. Overstress magnitude $[\frac{1}{p}\left(\frac{q^2}{\eta^2}+p(p-p_y)\right)(2p-p_y)]^n$ can decrease by decreasing n or by increasing the yield stress p_y. Since n is constant, the reduction in overstress is controlled by the yield stress. In Figure 4.9c, we observe that the yield stress evolves at a faster rate during the creep stages in damaged specimens. Higher yield stress change rate in the damaged specimen is intuitive because higher porosity damaged samples deform volumetrically at a higher rate.

Changes in viscosity during experiments indicate changes in resistance to flow of the material. Fracture interfaces accommodate deformation in the form of sliding along crack surfaces and as reduction in fracture aperture. Since fracture surfaces can deform easily, the resistance to flow is low near the fracture. On that account, a sample with many microfractures has less resistance to flow, so the change in viscosity is less (Figure 4.20b). The rate of viscosity increase is lower in an intact rock as there are fewer microfractures along which deformation occur during the experiment.

The pressure dependent bulk modulus K obtained from equation 4.7 is plotted in Figure 4.20d. The bulk modulus of the intact sample (blue D0 data) is higher because the intact sample

is elastically stiffer than the damaged specimen. These viscoplastic parameter evolution paths highlight the higher elastic, inelastic and plastic deformation of damaged specimens.

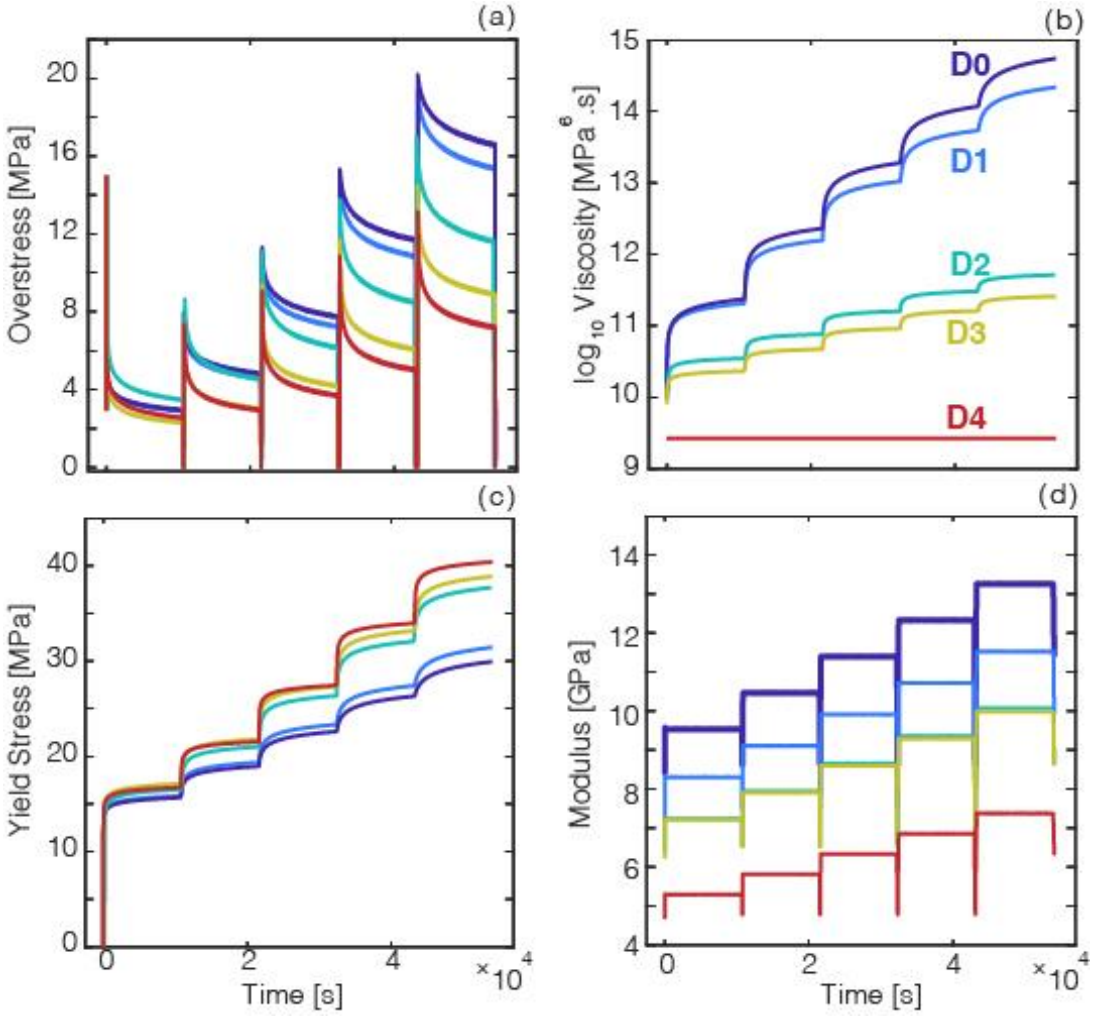

Figure 4.20. Evolution of a) Overstress, b) Apparent viscosity, c) Yield Stress, and d) Modulus with time for various degrees of damage for Bioturbated Siltstone specimens.

4.6 Conclusions

In this study, we characterized the time-dependent deformation of artificially fractured rocks from creep experiments, microstructural observations and visco-plastic modeling. Siltstone, bioturbated siltstone and sandy siltstone experimental data show that time-dependent

creep deformation is enhanced with damage. This time-dependent creep deformation has an unrecoverable portion or is plastic deformation, which we observe in Micro-CT and Scanning electron microscope images as reduction in fracture volume. With increasing differential stress magnitude, this creep deformation diminishes because there is less fracture volume remaining.

Our modeling results characterize the yield stress, viscosity, and overstress accumulation during these experiments to show that samples which are highly damaged have low viscosity because fractures reduce resistance to flow. In addition to high fracture density of fractured samples, the fractured samples have higher pore volume to accommodate deformation. Therefore, the yield stress evolves at a faster rate in a damaged specimen compared to a sample with less fracture volume. Due to the presence of high void volume, damaged samples are elastically and inelastically more compliant, which alludes to increase in both swelling and compression index.

Sandstone results are different from siltstone varieties. Sandstone porosity is reduced at low strain rate of impact due to compaction and crushed materials filling in the pore spaces. Due to low porosity, sandstones impacted at low strain rates show low creep strain. At high strain rates, grains are pulverized and void spaces form, therefore sandstone impacted at high strain rate shows more creep deformation. The trend of viscoplastic parameters with damage is not clear in sandstone due to the presence of this transition from pore volume loss to pore volume gain during impact.

The regression analysis shows that the Perzyna-MCC model can fit the experimental strain data and contains the basic components necessary to capture the viscoplastic behavior of fault damage zone rocks. However, lack of clear convergence into a set of constitutive parameters that describe the lab results indicate that additional knowledge about the physics

governing the micromechanics is necessary to establish complete understanding of the constitutive behavior. Further studies are needed to define what the physical meaning of apparent viscosity and overstress are in relation to the micromechanical phenomenon occurring at the grain scale. Such advances will lead to better understanding of how stress accumulate around compliant damage zones.

Acknowledgements

This study was supported by National Science Foundation Award No. EAR1727661. We thank Dr. Jessica Maisano and Dr. Matthew W. Colbert for their help and support in conducting CT scans at the University of Texas CT facility. Split Hopkinson Pressure bar experiments conducted at Ohio State University could not have been possible without the help of Dr. Ashley W Griffith, Dr. Michael Braunagel and Mr. Zachary Smith.

References

Aben, F. M., Doan, M.-L., Mitchell, T. M., Toussaint, R., Reuschlé, T., Fondriest, M., et al. (2016). Dynamic fracturing by successive coseismic loadings leads to pulverization in active fault zones. *Journal of Geophysical Research: Solid Earth*, *121*(4), 2338–2360.

Ben-Zion, Y., and Sammis, C. (2009). Mechanics, structure and evolution of fault zones. In *Mechanics, Structure and Evolution of Fault Zones* (pp. 1533–1536). Springer.

Blenkinsop, T. G. (1991). Cataclasis and processes of particle size reduction. *Pure and Applied Geophysics*, *136*(1), 59–86.

Chaboche, J.-L. (1986). Time-independent constitutive theories for cyclic plasticity. *International Journal of Plasticity*, *2*(2), 149–188.

Chang, Carl, Moos, D., and Zoback, M. D. (1997). Anelasticity and dispersion in dry unconsolidated sands. *International Journal of Rock Mechanics and Mining Sciences*, *34*(3–4), 48--e1.

Chang, Chandong, and Zoback, M. D. (2009). Viscous creep in room-dried unconsolidated Gulf of Mexico shale (I): Experimental results. *Journal of Petroleum Science and Engineering*, *69*(3–4), 239–246.

Chang, Chandong, and Zoback, M. D. (2010). Viscous creep in room-dried unconsolidated Gulf of Mexico shale (II): Development of a viscoplasticity model. *Journal of Petroleum Science and Engineering*, *72*(1–2), 50–55.

Chen, W. W., and Song, B. (2010). *Split Hopkinson (Kolsky) bar: design, testing and applications*. Springer Science \and Business Media.

Cheng, X., Tang, C., and Zhuang, D. (2022). A finite-strain viscoelastic-damage numerical model for time-dependent failure and instability of rocks. *Computers and Geotechnics*, *143*, 104596.

Cogan, J. (1976). Triaxial creep tests of Opohonga limestone and Ophir shale. In *International journal of rock mechanics and mining sciences \and geomechanics abstracts* (Vol. 13, pp. 1–10).

Dai, F., Huang, S., Xia, K., and Tan, Z. (2010). Some fundamental issues in dynamic compression and tension tests of rocks using split Hopkinson pressure bar. *Rock Mechanics and Rock Engineering*, *43*(6), 657–666.

Ding, X., Zhang, G., Zhao, B., and Wang, Y. (2017). Unexpected viscoelastic deformation of

tight sandstone: Insights and predictions from the fractional Maxwell model. *Scientific Reports*, *7*(1), 1–11.

Doan, M.-L., and Billi, A. (2011). High strain rate damage of Carrara marble. *Geophysical Research Letters*, *38*(19).

Doan, M.-L., and d'Hour, V. (2012). Effect of initial damage on rock pulverization along faults. *Journal of Structural Geology*, *45*, 113–124.

Doan, M.-L., and Gary, G. (2009). Rock pulverization at high strain rate near the San Andreas fault. *Nature Geoscience*, *2*(10), 709–712.

Drucker, D. C. (1950). Some implications of work hardening and ideal plasticity. *Quarterly of Applied Mathematics*, *7*(4), 411–418.

Dudley, J. W., Myers, M. T., Shew, R. D., and Arasteh, M. M. (1998). Measuring compaction and compressibilities in unconsolidated reservoir materials by time-scaling creep. *SPE Reservoir Evaluation \and Engineering*, *1*(05), 430–437.

Eslami Andargoli, M. B., Shahriar, K., Ramezanzadeh, A., and Goshtasbi, K. (2019). The analysis of dates obtained from long-term creep tests to determine creep coefficients of rock salt. *Bulletin of Engineering Geology and the Environment*, *78*(3), 1617–1629.

Haghighat, E., Rassouli, F. S., Zoback, M. D., and Juanes, R. (2020). A viscoplastic model of creep in shale. *Geophysics*, *85*(3), MR155--MR166.

Hagin, P. N., and Zoback, M. D. (2004a). Viscous deformation of unconsolidated reservoir sands—Part 1: Time-dependent deformation, frequency dispersion, and attenuation. *Geophysics*, *69*(3), 731–741.

Hagin, P. N., and Zoback, M. D. (2004b). Viscous deformation of unconsolidated reservoir sands—Part 2: Linear viscoelastic models. *Geophysics*, *69*(3), 742–751.

Healy, D. (2008). Damage patterns, stress rotations and pore fluid pressures in strike-slip fault zones. *Journal of Geophysical Research: Solid Earth*, *113*(B12).

Holzer, T. L., Höeg, K., and Arulanandan, K. (1973). Excess pore pressures during undrained clay creep. *Canadian Geotechnical Journal*, *10*(1), 12–24.

Hornby, B. E. (1998). Experimental laboratory determination of the dynamic elastic properties of wet, drained shales. *Journal of Geophysical Research: Solid Earth*, *103*(B12), 29945–29964.

Jones, L. E. A., and Wang, H. F. (1981). Ultrasonic velocities in Cretaceous shales from the Williston basin. *Geophysics*, *46*(3), 288–297.

Kao, H., and Chen, W.-P. (2000). The Chi-Chi earthquake sequence: Active, out-of-sequence thrust faulting in Taiwan. *Science*, *288*(5475), 2346–2349.

Kim, Y.-S., Peacock, D. C. P., and Sanderson, D. J. (2004). Fault damage zones. *Journal of Structural Geology*, *26*(3), 503–517.

Kolsky, H. (1949). An investigation of the mechanical properties of materials at very high rates of loading. *Proceedings of the Physical Society. Section B*, *62*(11), 676.

Kosloff, D., Scott, R. F., and Scranton, J. (1980). Finite element simulation of Wilmington oil field subsidence: I. Linear modelling. *Tectonophysics*, *65*(3–4), 339–368.

Kuo, L.-W., Song, S.-R., Yeh, E.-C., and Chen, H.-F. (2009). Clay mineral anomalies in the fault zone of the Chelungpu Fault, Taiwan, and their implications. *Geophysical Research Letters*,

36(18).

Ma, K.-F., Tanaka, H., Song, S.-R., Wang, C.-Y., Hung, J.-H., Tsai, Y.-B., et al. (2006). Slip zone and energetics of a large earthquake from the Taiwan Chelungpu-fault Drilling Project. *Nature*, *444*(7118), 473–476.

Mitchell, T. M., Ben-Zion, Y., and Shimamoto, T. (2011). Pulverized fault rocks and damage asymmetry along the Arima-Takatsuki Tectonic Line, Japan. *Earth and Planetary Science Letters*, *308*(3–4), 284–297.

Nadimi, S., and Shahriar, K. (2014). Experimental creep tests and prediction of long-term creep behavior of grouting material. *Arabian Journal of Geosciences*, *7*(8), 3251–3257.

Ostermeier, R. M. (1995). Deepwater Gulf of Mexico turbidites-compaction effects on porosity and permeability. *SPE Formation Evaluation*, *10*(02), 79–85.

Perzyna, P. (1966). Fundamental problems in viscoplasticity. In *Advances in applied mechanics* (Vol. 9, pp. 243–377). Elsevier.

Puig, F., Schenk, L., and Maraven, S. A. (1984). Analysis of the performance of the M-6 area of the Tia Juana Field, Venezuela, under primary, steam-soak, and steamdrive conditions. In *SPE Enhanced Oil Recovery Symposium*.

Rassouli, F. S., and Zoback, M. D. (2018). Comparison of short-term and long-term creep experiments in shales and carbonates from unconventional gas reservoirs. *Rock Mechanics and Rock Engineering*, *51*(7), 1995–2014.

Schofield, A., and Wroth, P. (1968). *Critical state soil mechanics*. McGraw-hill.

Scholz, C. H. (2019). *The mechanics of earthquakes and faulting*. Cambridge university press.

Simo, J. C., and Hughes, T. J. R. (2006). *Computational inelasticity* (Vol. 7). Springer Science \and Business Media.

Sone, H., and Uchide, T. (2016). Spatiotemporal evolution of a fault shear stress patch due to viscoelastic interseismic fault zone rheology. *Tectonophysics*. https://doi.org/10.1016/j.tecto.2016.04.017

Sone, H., and Zoback, M. D. (2013). Mechanical properties of shale-gas reservoir rocks — Part 2: Ductile creep, brittle strength, and their relation to the elastic modulus. *GEOPHYSICS*. https://doi.org/10.1190/geo2013-0051.1

Sone, H., and Zoback, M. D. (2014a). Time-dependent deformation of shale gas reservoir rocks and its long-term effect on the in situ state of stress. *International Journal of Rock Mechanics and Mining Sciences*. https://doi.org/10.1016/j.ijrmms.2014.04.002

Sone, H., and Zoback, M. D. (2014b). Viscous relaxation model for predicting least principal stress magnitudes in sedimentary rocks. *Journal of Petroleum Science and Engineering*. https://doi.org/10.1016/j.petrol.2014.09.022

Song, H., Liang, Z., Chen, Z., and Rahman, S. S. (2021). Numerical modelling of hydraulic fracture propagation in poro-viscoelastic formation. *Journal of Petroleum Science and Engineering*, *196*, 107640.

Talukdar, M., Sone, H., and Kuo, L.-W. (2022). Lithology and Fault-Related Stress Variations Along the TCDP Boreholes: The Stress State Before and After the 1999 Chi-Chi Earthquake. *Journal of Geophysical Research: Solid Earth*, *127*(2), e2021JB023290.

Trzeciak, M., Sone, H., and Dabrowski, M. (2018). Long-term creep tests and viscoelastic

constitutive modeling of lower Paleozoic shales from the Baltic Basin, N Poland. *International Journal of Rock Mechanics and Mining Sciences*, *112*, 139–157.

Wang, J., Wang, T., Song, Z., Zhang, Y., and Zhang, Q. (2021). Improved Maxwell Model Describing the Whole Creep Process of Salt Rock and its Programming. *International Journal of Applied Mechanics*, *13*(10), 2150113.

Wang, W.-M., Zhao, L.-F., Li, J., and Yao, Z.-X. (2005). Rupture process of the Chi-Chi (Taiwan) earthquake in 1999. *Chinese Journal of Geophysics*, *48*(1), 143–159.

Wood, D. M. (1990). *Soil behaviour and critical state soil mechanics*. Cambridge university press.

Wu, F., Liu, J. F., and Wang, J. (2015). An improved Maxwell creep model for rock based on variable-order fractional derivatives. *Environmental Earth Sciences*, *73*(11), 6965–6971.

Xia, K., Nasseri, M. H. B., Mohanty, B., Lu, F., Chen, R., and Luo, S. N. (2008). Effects of microstructures on dynamic compression of Barre granite. *International Journal of Rock Mechanics and Mining Sciences*, *45*(6), 879–887.

Yuan, F., Prakash, V., and Tullis, T. (2011). Origin of pulverized rocks during earthquake fault rupture. *Journal of Geophysical Research: Solid Earth*, *116*(B6).

Yue, L.-F., Suppe, J., and Hung, J.-H. (2005). Structural geology of a classic thrust belt earthquake: the 1999 Chi-Chi earthquake Taiwan (Mw= 7.6). *Journal of Structural Geology*, *27*(11), 2058–2083.

Zoback, M. D. (2010). *Reservoir geomechanics*. Cambridge University Press.}

4.7 Appendix

4.7.1 Limiting conditions in Optimization

We set some limiting conditions in the optimization to determine if the cost function is minimized. While running the inverse problem to obtain the visco-plastic parameters, if the difference in cost function between subsequent evaluations ($\partial\phi$) is below 10^{-14}, the optimization stops and the corresponding cost function is considered to have been minimized. We also set the maximum number of evaluations to be 3000, such that if the cost function difference between subsequent evaluations is above 10^{-14} till the 3000^{th} evaluation, we terminate the optimization. The solutions which reached 3000 iterations are considered non-converged; therefore, we discard these results.

4.7.2 Weighting the loading and creep part of the deformation

The stress and strain histories in Figures 4.1 and 4.2 show that the creep stages of the experiments are longer (3 hours) than the loading and unloading stages of the experiment. During the loading and unloading stages, the samples are loaded at 10 MPa/ minute. Since the frequency of data collection is 1 sec, the number of data points for a 10 MPa loading is 60, which is less than the number of data points during a creep stage, i.e., (((3 hours) x 60 minutes) x 60 sec) = 10800 data points. Due to large number of data points during the creep stage of the deformation, fitting the visco-plastic model will be heavily biased towards fitting the creep stage and not the loading and unloading stages which reflects the λ and κ values. The majority of the creep deformation also occurs at the beginning of the creep. Therefore, we introduce a weighting function which de-emphasizes the contribution of the residuals of the later data points in the creep. During loading and unloading, the weighting function c is maintained at 1; whereas, during the creep stages

$$c = \frac{1}{(t_{creep})^{w}} \qquad (4.12)$$

Where t_{creep} is time elapsed since beginning of the creep stage, and w determines how much greater emphasis is put on the beginning of the creep as compared to the later data points. A w value of 0 indicates that the entire creep stage has a weight of 1, which is equivalent to no weighting. With increasing w, the beginning of the creep stage is weighted more than the long-term creep trend. Therefore, our modified cost function is:

$$\phi = \sqrt{\frac{\sum_{i=1}^{T}(c_i\varepsilon_i^{model} - c_i\varepsilon_i^{data})^2}{T}} \qquad (4.13)$$

Where c_i is the weighting function at time step i. We test results for various w values of 0.1, 0.3, 0.5, and 1. A comparison of the weighting function is shown in Figure 4.S1 in the supplementary material. With increasing w, loading-unloading and initial part of the creep stage is fitted better than the long-term creep trend. A w value of 0.5 is chosen as it produced optimal results.

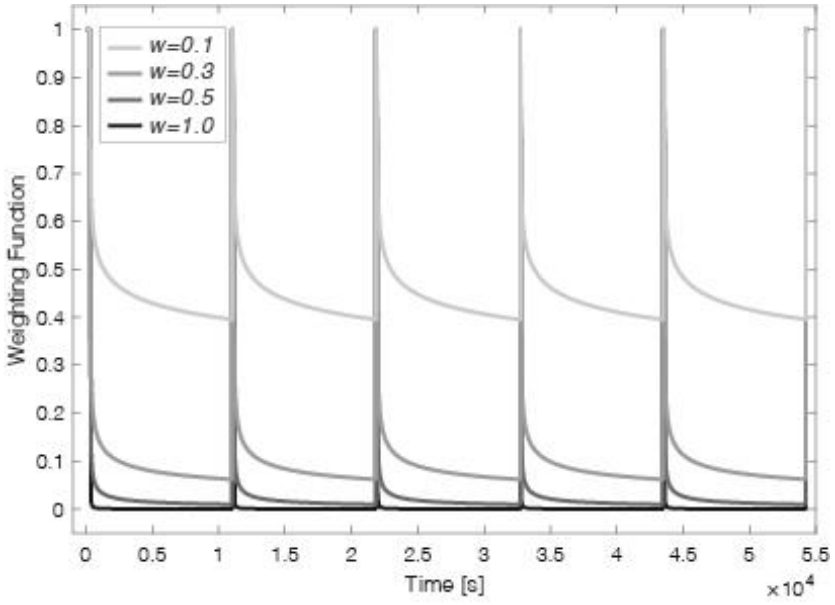

Figure 4.S1. Comparison of the weighting function c when w value is 0.1, 0.3, 0.5 and 1. During the loading and unloading stages, the weighting function is equal to 0, whereas, during the creep stages Equation 4.12 is used to calculate weighting function.

CHAPTER 5

Time-dependent velocity recovery of synthetically damaged rocks and comparison with field scale velocity recovery

Abstract

Fault damage zones surrounding the primary slip plane are characterized by the presence of fractures, which are either open, healed or sealed. Open fractures are created by stress concentrations that develop during fault slip, then heal by a variety of processes including

mechanical compaction facilitated by grain and fracture sliding that occur between fault slip. Signatures of fracture closure have been observed by repeated seismic surveys after large earthquakes, which show progressive seismic velocity increase (or recovery) after each earthquake. However, the quantitative link between field scale seismic observations of healing and the physical process of healing has not been established. In this study, we conducted creep experiments on artificially damaged rocks to study the time-dependent velocity increase associated with compaction of the fracture volume and to evaluate the potential magnitude of seismic velocity recovery that could be caused in the field by such mechanical healing. To study the time-dependent evolution of the fracture volume of damaged rocks, we used rock cores recovered from the Taiwan Chelungpu-fault Drilling Project (TCDP) and impacted with a Split Hopkinson Pressure Bar to create a range of fracture volumes (resembling fracture intensities at various distances from the fault core). The damaged rocks were then subjected to pressure hold stages in a triaxial apparatus. We observed that more highly damaged specimens showed greater velocity recovery. The time-dependent velocity recovery can be fit by a logarithmic function against time, consistent with previous observations of logarithmic increases in seismic velocity in natural settings. Experimental data extrapolated over 6 years with the logarithmic fit is slightly lower than field studies in the Chelungpu fault area by Chen et al. (2015), possibly due to other healing mechanisms. A comparison of the velocity with porosity data reveals that creep-induced strengthening of the junctions of fracture interfaces increases the stiffness of the material at a faster rate than pore compaction during the hold stages.

5.1 Introduction

Following an earthquake or the passage of seismic waves, multiple transient processes are active in the earth's crust, especially in the near-surface damage zone of a fault. These

transient processes include decreasing seismic velocity (Olivier et al., 2015; Rubinstein and Beroza, 2004), and increasing permeability (Manga et al., 2012). Seismic velocity decrease is followed by velocity increase over a period of days to months or years after an earthquake (Illien et al., 2022), as observed by variety of methods like active seismic surveys (Li et al., 2003), passive tomography using microseismicity (Froment et al., 2014), ambient noise cross-correlation (Hobiger et al., 2014; Liu et al., 2018; Taira et al., 2015), spectral ratio analyses (Karabulut and Bouchon, 2007), joint inversion of travel time data (Pei et al., 2019) and waveform deconvolution in boreholes (Sawazaki et al., 2009; Wu et al., 2010). Understanding such co-seismic velocity reduction and subsequent recovery in epicentral areas of large earthquakes is crucial to understanding the rate at which a fault regains its strength after an earthquake. Thus, characterizing this time-dependent change is important in studying the evolution of fault systems in the past, present and future.

This temporal increase in seismic velocity has been attributed to the reduction in crack density. Quantitative estimates of change in velocity due to change in density of cracks was first discussed by Garbin and Knopoff (1973). Using this theory, repeated seismic surveys after the 1992 Mw 7.5 Landers earthquake indicate a decrease in crack density of ~1% from 1994 to 1996 (Li et al., 1998). Vidale and Li, (2003) reported a crack density decrease after the Landers Earthquake of 1.8% between 1994 and 1996 and 1.1% between 1996 and 1998 from seismic velocity measurements. A similar study after the 1999 Mw 7.4 Hector Mine Earthquake shows an increase in P and S wave magnitude by 0.7-1.4 % and 0.5-1%, respectively, from 2000- 2001 (Li et al., 2003) corresponding to an apparent crack density decrease of 1.5% within the rupture zone. A dense seismic array installed after the 2004 Mw 6.0 Parkfield earthquake showed an increase in S wave velocity by ~1% in a period of three months after the earthquake due to

apparent crack density decrease of 0.016 (Li et al., 2006). These studies suggest some transient pore volume loss happening in the damage zone after the main event, which led to healing of the fracture damage and stiffening of the rocks.

Temporal permeability increase in the damage zone has also been observed in fault damage zones. For example, injection experiments in three boreholes drilled after the 1995 M3 7.3 Hyogoken-Nanbu earthquake in the Nojima fault zone, conducted in 1997, 2000 and 2003 showed a continued reduction in permeability (Kitagawa et al., 2007). Likewise, after the Wenchuan earthquake in 2008, Wenchuan earthquake Scientific Fault Drilling Project (WFSD) constructed multiple boreholes which penetrated the primary slip plane. The first borehole WSFD-1 encountered the fault core and was open to fluid flow to record permeability changes in the surrounding damage zone over time (Xue et al., 2013). Permeability calculated in this area from water level response to tidal forcing shows an increase upon the passage of teleseismic waves from a distant event and temporal permeability decrease between these events. After the 2014 South Napa earthquake, a similar timescale of 50 days between seismic velocity recovery (Taira et al., 2015) and duration of stream discharge increase (Wang and Manga, 2015) suggests that seismic velocity and hydrological changes were closely linked in the fault zone. This link suggest that time-dependent crack closure and permeability reduction are interrelated processes in the damage zone.

Such fracture healing has implications for increase in strength of fault zones. Brenguier et al., (2008) observed time-dependent velocity increase after the Parkfield earthquake and correlated it to the tremor-rate of aftershocks. The tremor rate of aftershocks decays with time, following the trend of Omori decay (Utsu et al., 1995). Since aftershocks are believed to occur by slip along pre-existing fracture surfaces, decay in tremor rate after large earthquakes has been

attributed to time-dependent healing of cracks in the damage zone, hindering further slip. Therefore, it is important to understand how long it takes for the fractures to heal in the damage zone as it affects the probability of another earthquake in a fault zone.

This study aims to compare the time-dependent increase in velocity observed in field scale seismic studies to laboratory observed ultrasonic velocity recovery. Such a study will help to understand the physical processes associated with the time-dependent material stiffening in damage zones of large fault systems, provide insights into the various factors which affect damage healing after earthquakes, and its mechanical significance in the earthquake cycle. The chapter is organized such that we first present the methodology of obtaining ultrasonic waves during the experiment (Section 5.2). In the results section, we present velocity history during the triaxial stage of the experiment and obtain fitting parameters to extrapolate the data to larger time scale (Section 5.3). Then, we compare the laboratory-observed velocity recovery to field observations of post-seismic velocity recovery (Section 5.4). The discussion section explores the various physical mechanisms which may be active in the healing process observed in the laboratory and compare with processes at the field scale.

5.2 Methodology

In this study, we used core samples from several lithologies (siltstone, bioturbated siltstone, sandy siltstone, sandstone) acquired from the Taiwan Chelungpu-fault Drilling Project (TCDP). These core samples were impacted with a Split Hopkinson Pressure bar to create fractures within the specimen in a way that it disrupts strain localization and fosters pervasive damage. SHPB is used to create pervasive damage because strain rates achieved by SHPB is in the order of strain rates observed in the damage zone during a sub-shear to super shear rupture (Doan and Gary, 2009). Cylindrical samples, 25.4 mm in diameter were impacted using various

projectile velocities to create samples with a ranging degree of damage. D0 denotes undamaged samples and degree of damage increase from D1 to D4 samples. Details of sample preparation and dimensions are described in Chapter 4 (Section 4.2.3).

Creep deformation of the damaged specimens were tested at various confining pressure and axial differential stress stages to simulate stress conditions analogous up to 1 km depth, the approximate depth of the TCDP core samples. We loaded the specimens to 5, 10, and 15 MPa confining pressures, between which the pressure was held constant for 3 hours to observed time-dependent creep deformation under constant stress (Figure 5.1). Confining pressure was unloaded and reloaded after each creep before moving to the next step to observe the post-creep static modulus. After the hydrostatic creep stages, samples were subjected to axial differential stress steps up to 5, 10, 15, 20 and 25 MPa, between which the stress was again held constant to observed creep deformation (Figure 5.1). Axial differential stress was again unloaded and reloaded after each creep to observe the post-creep static modulus.

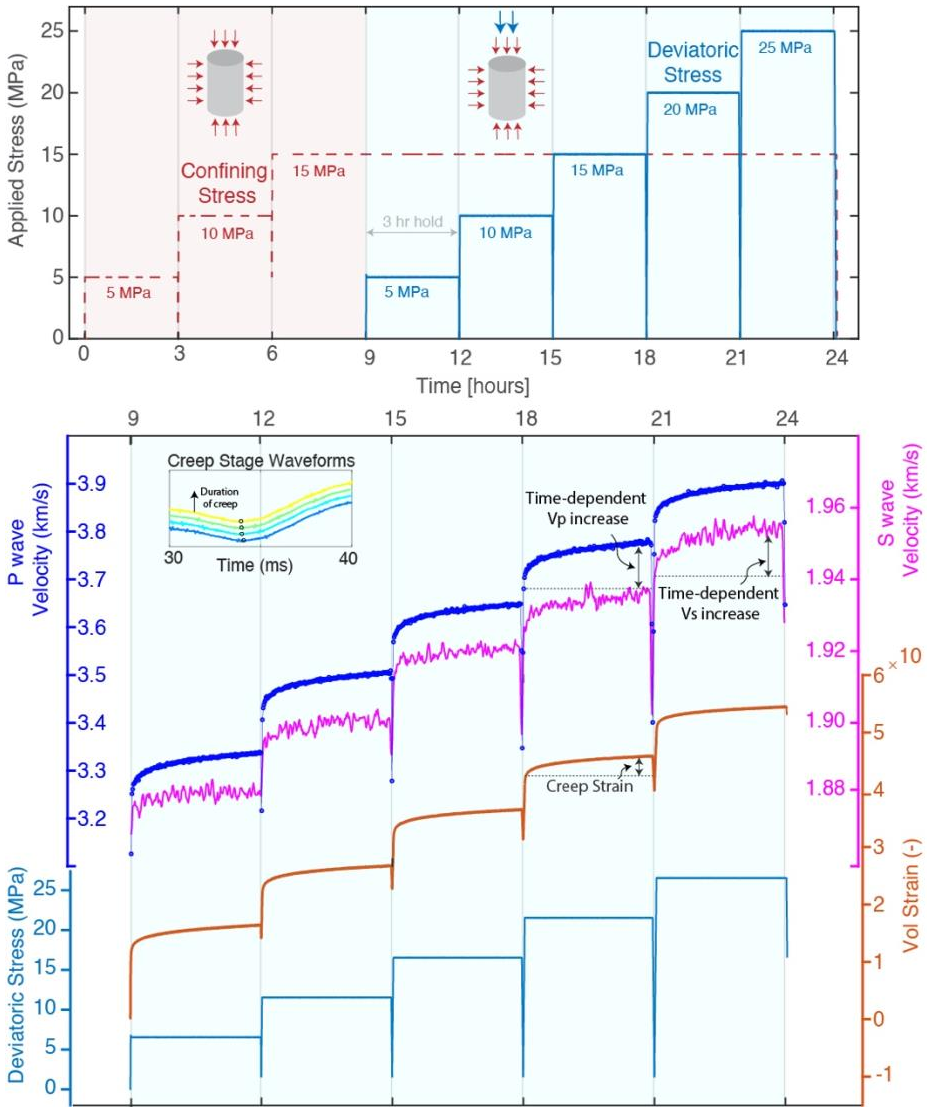

Figure 5.1. (a) Confining pressure and deviatoric stress magnitude history during each experiment. The constant stress stages are for 3-hour stages. (b) Input deviatoric stress history and corresponding output history of creep strain, S wave velocity and P wave velocity (from top to bottom) during the triaxial stage. The plot shows time-dependent creep strain, increase in S and P wave velocity at constant deviatoric stress.

Piezoelectric crystals are placed on the top and bottom platens to record ultrasonic waves during the experiment. A high viscosity bonding medium was used to bond the platens to the samples. We simultaneously collect P and S waves every 1 minute to observe the changes in ultrasonic velocities. Ultrasonic waves collected during the experiment are used to calculate the velocity of the sample (Figure 5.1b). Once an arrival time is manually picked for a representative

waveform, the arrival times of the remaining waves are picked using cross correlation. The length of the sample is divided by the difference between the travel time and the face-to-face time (i.e., travel time between piezoelectric transducers without the sample) to calculate both P and S wave velocities (one such example is shown in Figure 5.1b).

5.3 Results

5.3.1 Time-dependent trends

The velocity histories of bioturbated siltstone and sandstone specimens are shown in Figure 5.2. Figures 5.2a and 5.2b show the absolute P-wave velocity for bioturbated siltstone and sandstone, respectively, whereas Figures 5.2c and 5.2d illustrate the absolute S wave velocity histories for bioturbated siltstone and sandstone, respectively.

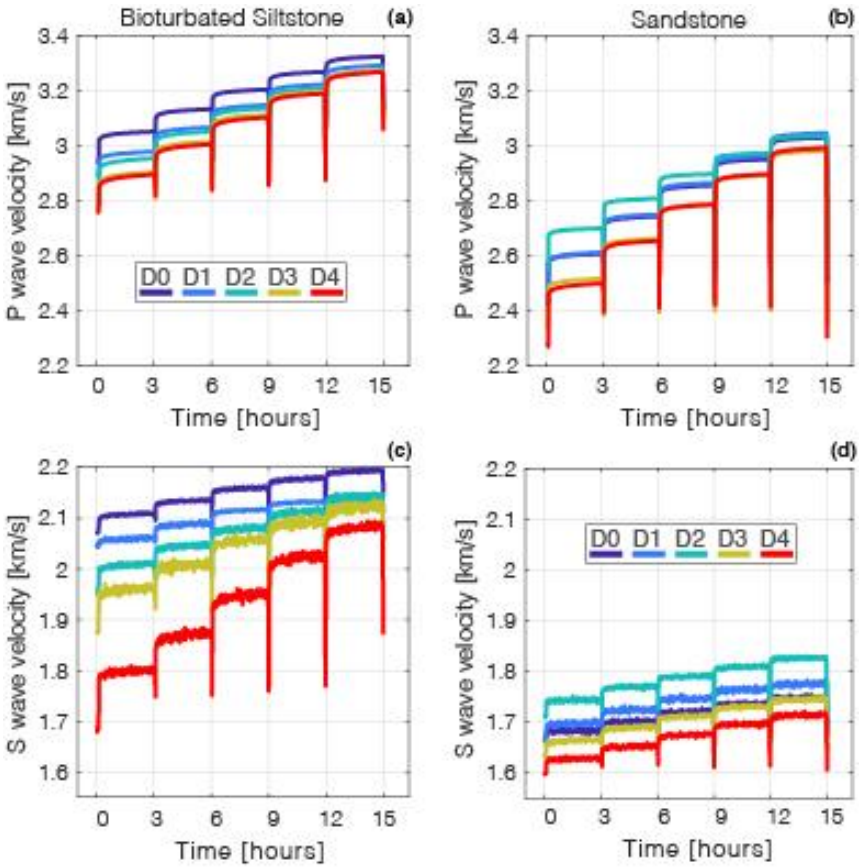

Figure 5.2. P and S wave velocity for bioturbated siltstone and sandstone specimens. (a) P wave velocity for bioturbated siltstone, (b) P wave velocity for sandstone, (c) S wave velocity for bioturbated siltstone, (d) S wave velocity for bioturated siltstone.

Velocity increases during loading due to fracture closure and increase in elastic stiffness of the rock, as observed in the stage before the creep stages in Figure 5.2. During unloading, the sample experiences expansion, and the fracture volume increases. Fracture volume increase reduces the sample velocity (Figure 5.2), as observed by the reduction in velocity during unloading after every creep stage. During each creep stage, both P and S waves show a time-dependent increase, indicative of fracture closure and contact stiffening also occurring as a function of time.

The bioturbated siltstone data are representative of all siltstone varieties, (i.e., bioturbated siltstone, siltstone, and sandy siltstone) therefore, we show only the bioturbated siltstone results in Figure 5.2. We observe that samples with more damage have lower initial P-wave velocity (Figure 5.2a). However, velocity recovery following creep is greater in samples with more damage. Therefore, the difference between the final velocities of the samples is smaller after the fifth creep stage. S wave results for Bioturbated siltstone (Figure 5.2c) also show that the D4 sample has the slowest initial velocity but higher recovery during the experiments.

Velocity recovery in sandstone specimens follow the same trend observed in strain data in Chapter 4. An increase in initial velocity is observed from D0 to D2 due to decrease in porosity and decrease in velocity from D2 to D4 due to increase in fracture porosity. D2 has the least porosity before the creep experiments and shows highest initial P and S wave velocity because D2 has fewer fractures remaining to close, decelerating the rate of creep (Figure 5.2b). Low porosity and lower rate of of D1 and D2 samples are discussed in Section 4.3.

The healing process in these experiments manifests as a decrease in pore volume of the rock, and a corresponding increase in velocity as the fracture surfaces come in contact with each other. We summarize the velocity increase during the triaxial stages of the experiment, and the corresponding porosity decrease during the hold stages which collectively forms C-shaped curves as shown in Figure 5.3. We observe from the C-shaped curves that the highly damaged specimens show more velocity increase and porosity decrease than an undamaged specimen. Comparison of porosity and velocity change at low differential stress magnitude with high differential stress magnitude show that the opening of the C-shaped curve reduces due to lower pore volume remaining to compact (Figure 5.3). The porosity-velocity comparisons are further discussed in Section 5.4.1.

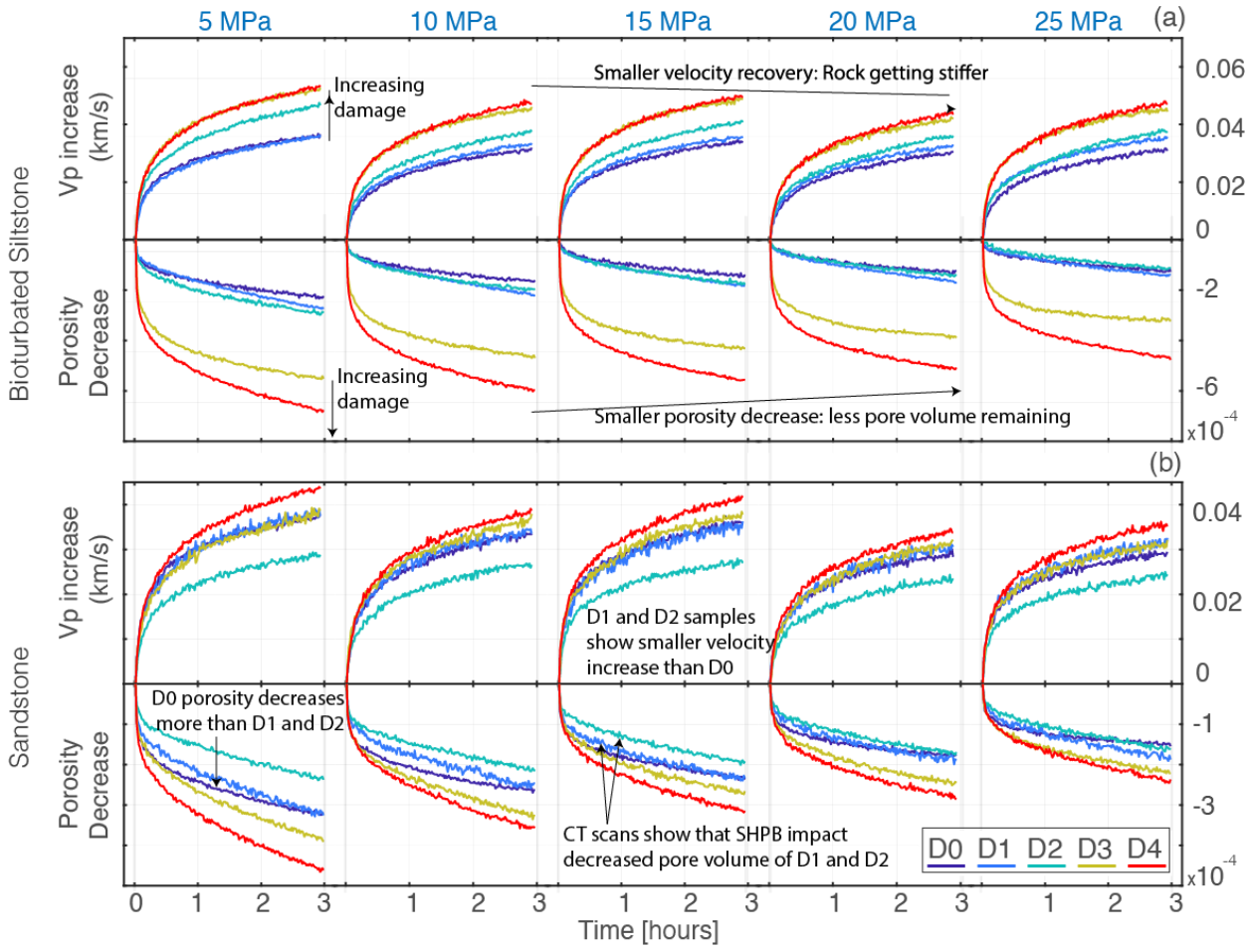

Figure 5.3. Relative velocity and porosity evolution during the creep stages of the experiment for (a) bioturbated siltstone and (b) sandstone, respectively.

5.3.2 Regression of logarithmic trend

Next, we quantify the abovementioned description of initial velocity and velocity increase with the help of a fitting function. We use a logarithmic function of time (t) to fit the velocity recovery during the hold stages of the experiment:

$$V = V_o\{1 + \alpha \log_{10}(t + 1)\} \qquad (5.1)$$

where V_o is the reference velocity of the material for a single creep stage, i.e., the velocity of the material before creep deformation, and α is a dimensionless constant that determines the magnitude and rate of velocity recovery during a hold stage. The argument of the logarithmic function is *(t+1)* to avoid singularity at *t=0*.

Equation 5.1 is motivated by the time-dependent increase in frictional coefficient observed by Dieterich (1972). Direct shear friction experiments on sandstone, graywacke, red granite and quartzite show that for intervals of greater than 1 sec, rock friction data are fit by the function $\mu = \mu_o +$ a $log_{10}(t)$. Dieterich (1972, 1978) attributed this behavior to 'time-dependent plastic flow' at the junctions that increases the strength of contacts, or compaction of gouge separating the slip surfaces. We hypothesize that similar processes are active in our specimens, leading to the stiffening of grain contacts. Therefore, we use Equation 5.1 to fit the time-dependency of velocity history, although the mechanical correlation between frictional strength recovery and contact stiffness is not justified here.

Regression of the logarithmic velocity-time relationship is shown in Figure 5.4 for all bioturbated siltstone samples. P and S wave velocities from all creep stages are plotted from left to right with lines indicating the fit and open circles indicating the data. Every 10th data point is plotted for visual clarity. The regression shows that equation 5.1 captures the velocity increase trend well, with R^2 values always exceeding R^2=0.99.

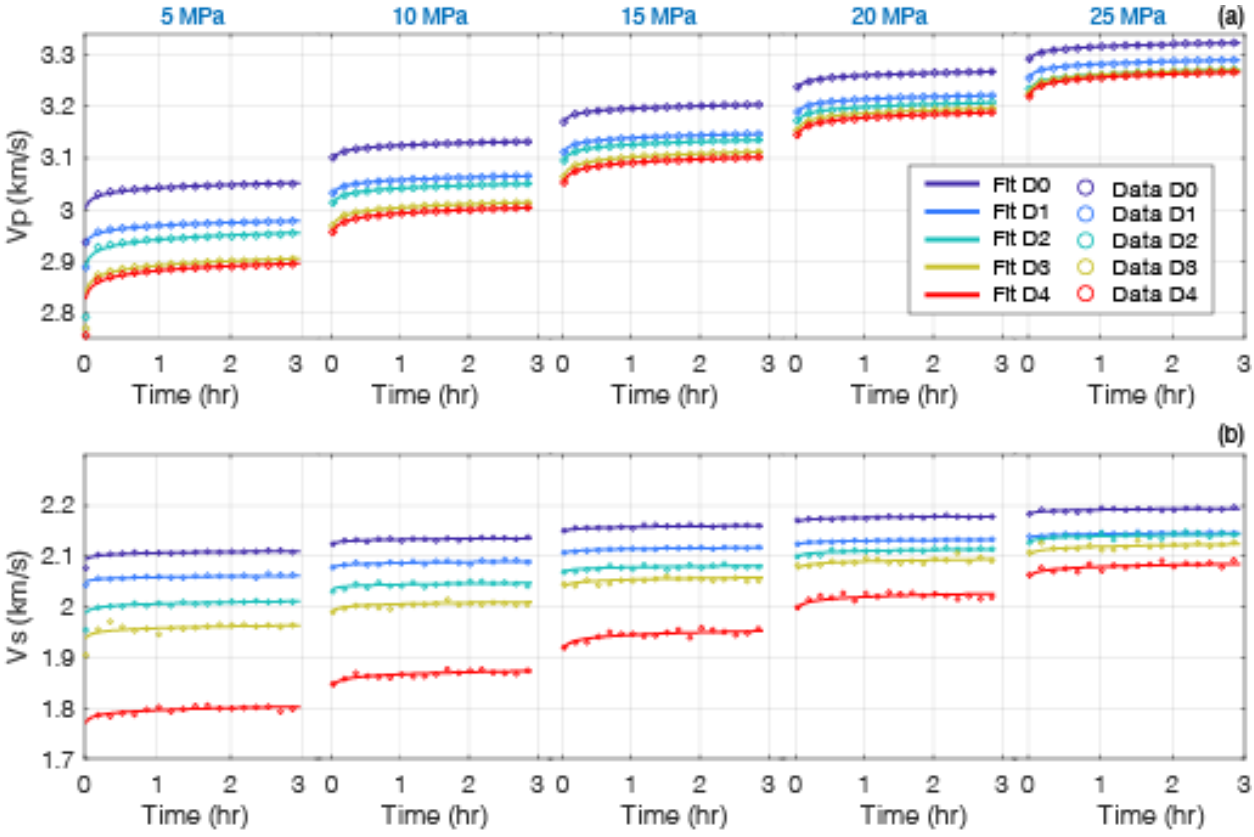

Figure 5.4. Velocity data with logarithmic fit for bioturbated siltstone specimens (a) P wave velocity data, and (b) S wave velocity data.

The resulting optimized parameters, V_0 and α, for all rock types and differential stress magnitudes are shown in Figure 5.5. For a specific rock type and damage density, the reference velocity V_o of the rocks increases with increasing differential stress magnitude (Figure 5.5a). This is because the material stiffens progressively during the experiment as the applied axial

differential stress increases. On the other hand, the magnitude of recovery, α is higher at the beginning of an experiment as there are more open cracks as compared to a later stage of the experiment, when fewer cracks are open. Since velocity recovery diminishes with crack closure, α decreases with increasing differential stress magnitude (Figure 5.5c, d).

Highly damaged specimens show lower initial velocity V_o because porosity is higher and pore stiffness is lower in damaged specimens compared to an intact rock (observed in Figures 5.2, 5.4). The magnitude and rate of velocity increase is higher in a damaged specimen (D4) than an intact rock (D0), therefore α increases with damage (Figure 5.5c, d). In sandstone, because of the non-monotonic change in pore volume with damage, V_o increases from D0-D2 and decreases from D2-D4. Accordingly, the parameter α also decrease from D0-D2 and then increase from D2-D4. Parameters V_o and α from the S wave velocity data generally show the same trend as the P wave velocity (Figures 5.5b and 5.5d), although few exceptions are found such as the monotonic increase in α with damage observed in sandstones.

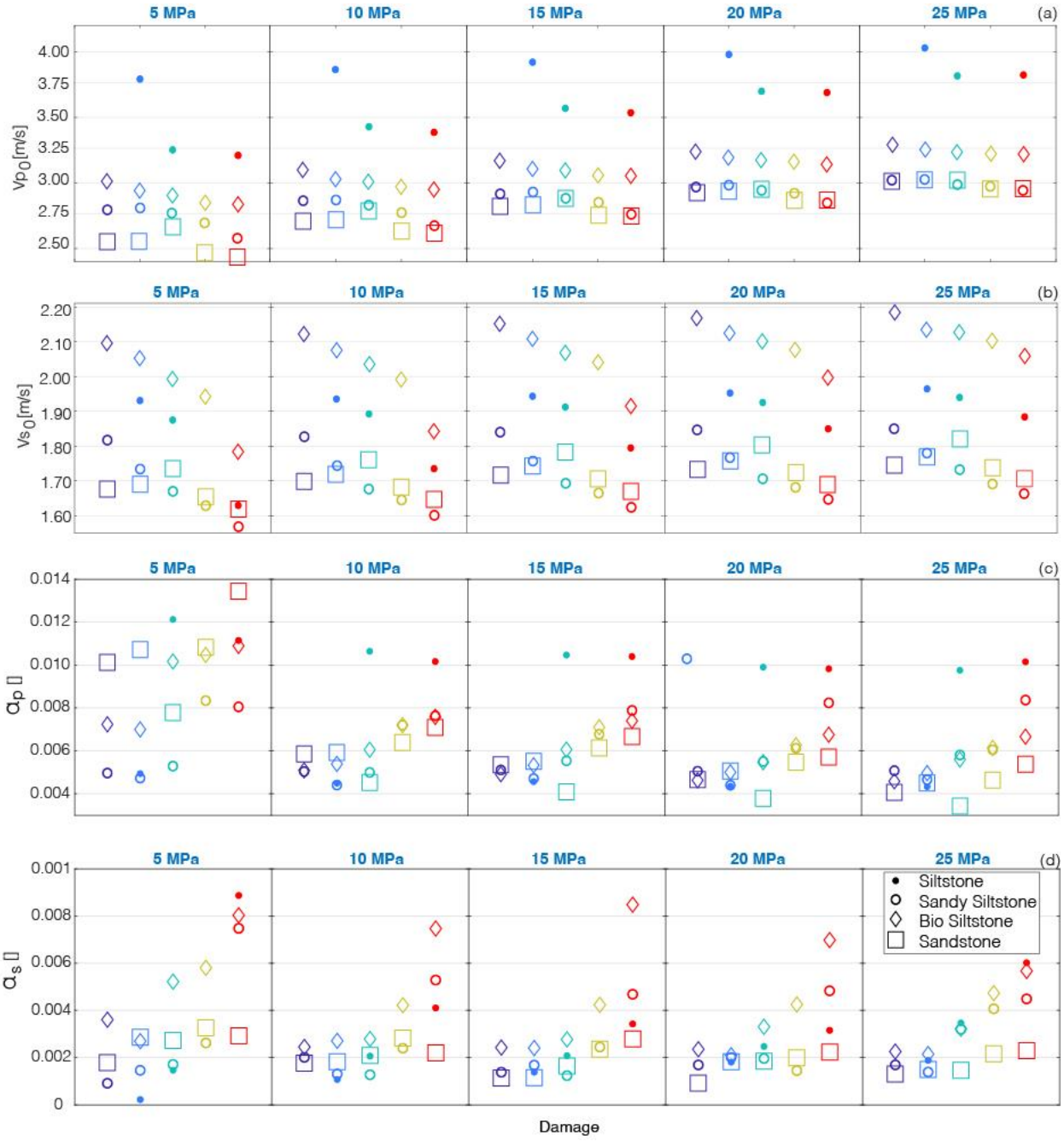

Figure 5.5. V_o and α for all rock types. V_o for (a) P- and (b) S-wave velocity data, respectively. α for (c) P- and (d) S-wave velocity data, respectively. The figures show an overall increase in α with damage and decrease in α with differential stress magnitude.

5.3.3 Extrapolation of healing trends

With the assumption that the logarithmic trend would continue beyond the laboratory observation time scale, the optimized parameter α can be used to estimate the velocity increase of the damaged rocks at longer time scales. Results of such extrapolation of P-wave data for the bioturbated siltstone specimens at 10 MPa deviatoric stress hold stage are shown in Figure 5.6a. With increasing time duration of creep, the difference between the D0 and D4 bioturbated siltstone velocity diminishes. Vertical lines corresponding to 1 hour, 1 day and 1, 2 and 6 years are plotted to easily visualize the log-time scale in the x-axis of the plot. We show the results up to 6 years to compare with similar time frames in Section 5.4.1.

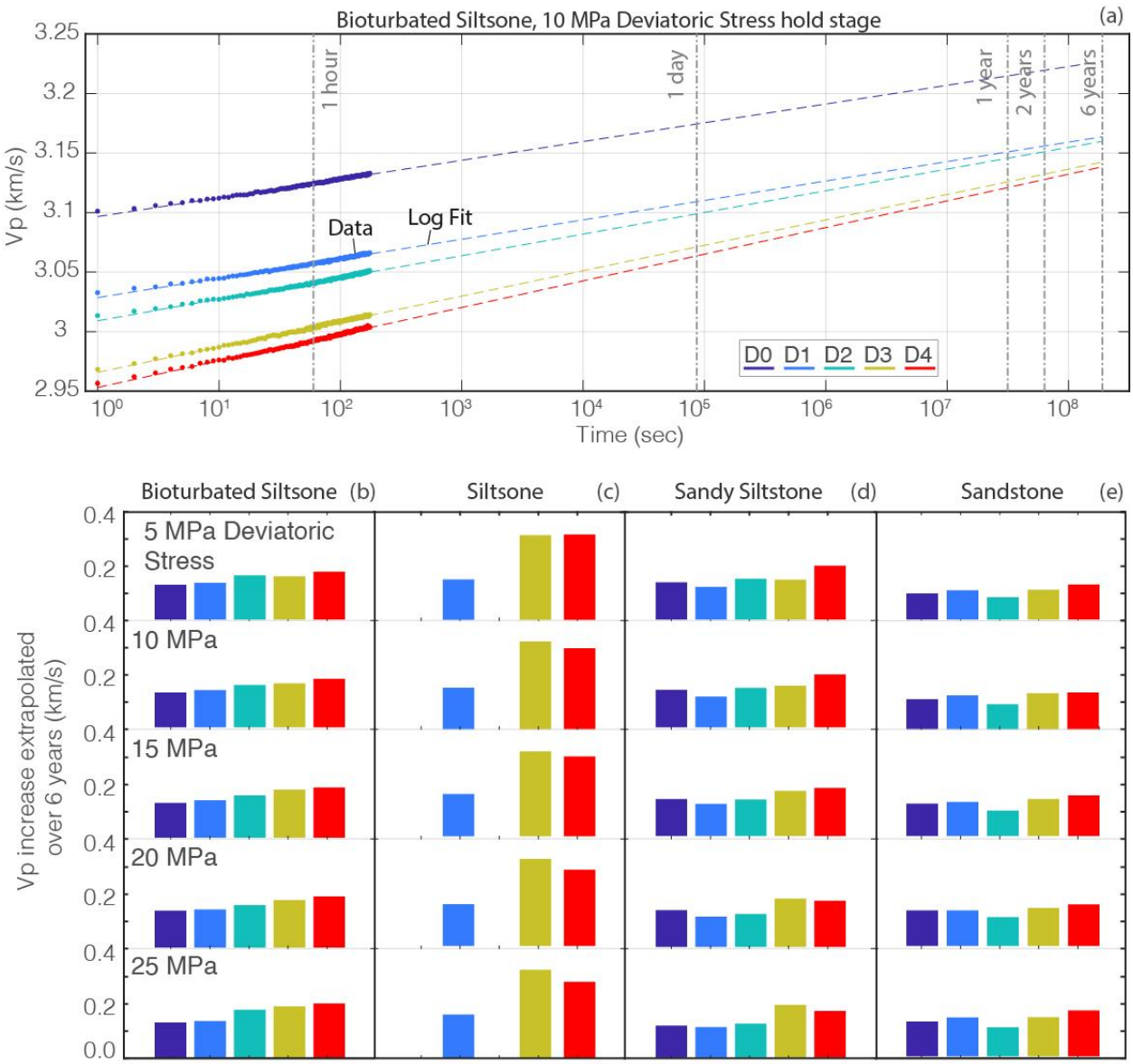

Figure 5.6. (a) Extrapolation of data to longer time scales. (b-d) Bar graph of P wave velocity increase over 6 years for bioturbated siltstone, siltstone, sandy siltstone and sandstone, respectively.

Extrapolated results for all the rock types over a period of six years are shown in Figure 5.6b-d. The bar graphs summarize percent increase in velocity due to recovery. The bar charts show that the magnitude of velocity increase ranges from ~0.1 km/s for D0 samples to > 0.2 km/s for D3 and D4 samples over six years. The bioturbated siltstone, siltstone and sandy

siltstone samples show a greater increase in velocity with increasing damage of the specimen. However, the sandstone variety shows that velocity increase in D0 is higher than D1 and D2. This is primarily due to the lower porosity of the D1 and D2 sample as compared to the D0 sample. D3 and D4 show more velocity recovery than D2 because fractures were created in D3 and D4 samples during SHPB impact, which in turn facilitates fracture volume closure during the hold stages of the experiments. (Section 4.3).

Temporal velocity increase observed in a damaged rock, is a superposition of the velocity recovery of intact rock D0 and velocity recovery due to healing of cracks formed by SHPB. The intact rock D0 shows a time-dependent velocity increase as the rock matrix is compacted to its initial in-situ state during the experiments. This process is the reverse process of anelastic strain recovery where a sample undergoes time-dependent expansion once in-situ stresses are released (Matsuki and Takeuchi, 1993; Teufel, 1983). Similarly, ‘re-compaction’ is likely a time-dependent process, as observed by the creep and velocity curves of D0 (Figure 4.2, Figure 5.2, 5.3). To distinguish this re-compaction and crack healing process in a damaged sample, we subtract the velocity change of the intact sample from the velocity change of the damaged sample to focus solely on the crack healing processes in the upcoming section. This calculation is essential for comparison with field studies because velocity recovery in the field is observed in high crack density areas of the damage zone and not in the intact host rock, whereas time-dependent re-compaction induced velocity recovery of intact rock D0 is an artifact of our experiment. In the following sections, we report *adjusted* velocity, which is defined as the extrapolated velocity of the sample minus the extrapolated velocity of the intact sample of the same rock type.

5.4 Discussion

5.4.1 Comparison with field observations

From experimental results, we observe that the most damaged specimens show greater velocity recovery than samples which are less damaged (Figure 5.2). Similar observations have been made by Vidale ad Li (2003) from seismometers placed in the same boreholes in 1994, 1996, 1997, 1998, 2000 and 2001 to record seismic velocity change at various distances from the Hector mine earthquake primary slip plane. This spatial variation in velocity recovery is attributed to higher damage density near to the fault core and lower damage density away from the fault core. Highly damaged samples show an increasing rate of damage recovery because more cracks close in an inherently high crack density material.

5.4.1.1 Magnitude comparison

We compare the percent increase in velocity observed in laboratory creep experiments, extrapolated over a period of six years to field measurements. Although the rocks acquired for this study belong to the Chelungpu fault system, we compare the velocity history with the Longmenshan fault owing to the continuous temporal extent of the field data in this area, facilitating comparison. Figures 5.7 show comparison of the D1 and D4 adjusted velocity (velocity after subtracting D0 contribution) with field observations. Adjusted velocity increase for D1 bioturbated siltstone is ~0.5 % over a course of six years. D4 bioturbated siltstone specimens show adjusted velocity increase of 2%. Figure 5.7 shows that field-observed velocity recovery prior to the Lushan earthquake (LSEQ) in May 2013 matches the experimental data (Figure 5.7). Laboratory observed time-dependent velocity recovery cannot explain the coseismic velocity increase during the Lushan earthquake, therefore comparison of velocity recovery is only valid till the Lushan earthquake.

The 0.5-2% velocity increase estimated by extrapolating the laboratory data is lower than the 2-7% velocity recovery reported in the damage zone of the Chi-Chi earthquake (Chen et al., 2015). Seismic survey by Vidale and Li (2003) reported an increase in P-wave velocity of 2.5% over a period of six years following the Landers earthquake, also higher than the 0.5-2% laboratory observed velocity recovery. Lower velocity recovery observed from laboratory extrapolation (especially in the Chelungpu fault system) may indicate that there are other velocity recovery mechanisms in natural fault systems, which the experiments are unable to capture.

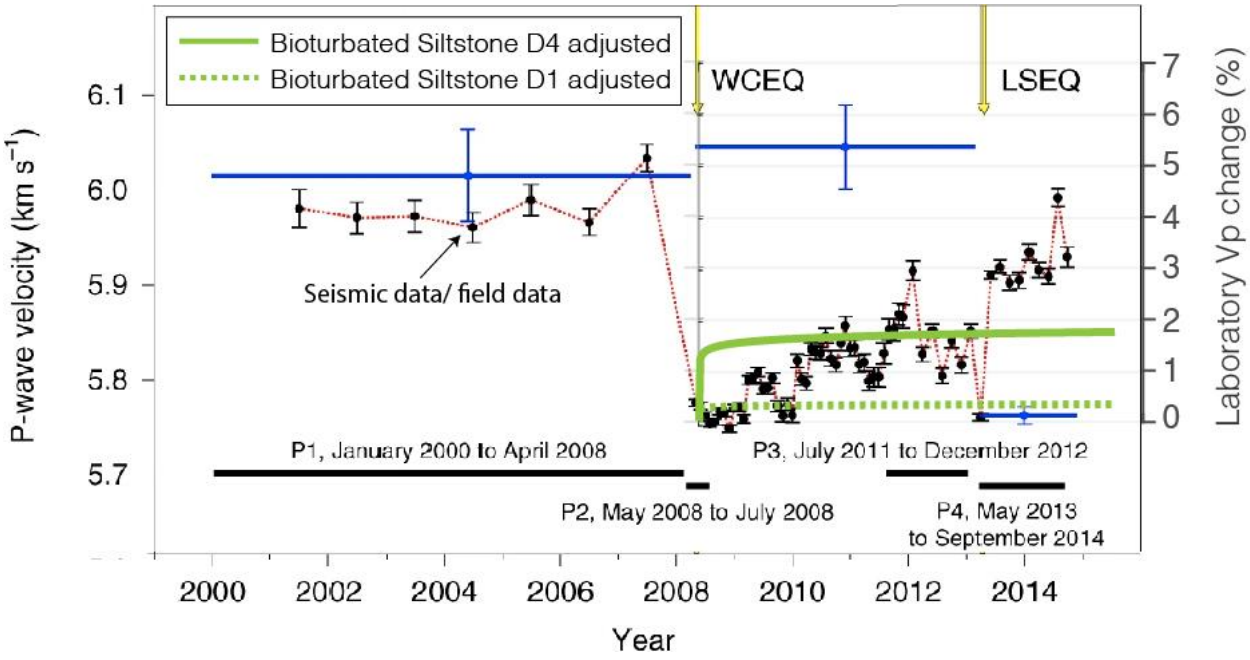

Figure 5.7. The average velocities in the Longmenshan and Lushan areas are shown by blue and black dots, respectively (Pei et al., 2019). The absolute magnitude of P wave velocity before the Wenchuan earthquake is used to calculate the percent change in P wave velocity between the Wenchuan earthquake (WCEQ) and Lushan earthquake (LSEQ) (y-axis to the right). The experimental results of velocity recovery are overlaid on top of the field data.

5.4.1.2 Rate comparison

Logarithmic recovery of seismic velocity has also been suggested by various authors from a combination of field and experimental observations. Logarithmic post-seismic recovery has been observed after the 1984 Mw 6.2 Morgan Hill Earthquake, 1989 Mw 6.9 Loma Preita earthquake (Rubinstein and Beroza, 2004; Schaff and Beroza, 2004), 1990 Mw 5.4 Chittenden earthquake (Rubinstein and Beroza, 2005) as well as the 1999 Mw 7.4 Izmit and Mw 7.1 Duzce earthquakes (Peng and Ben-Zion, 2006; Wu et al., 2009). Laboratory experiments have also observed a logarithmic recovery of material properties with time in earth and granular micro-composite materials (TenCate, 2011; Tremblay et al., 2010). Creep experiments conducted by Meyer et al. (2021) on Carrara marble show that wave speed increases logarithmically with time during the hold stages of triaxially loaded samples. This linear relationship of wave speed recovery with logarithm of time can last anywhere from a few seconds (Shokouhi et al., 2017) to several years (Brenguier et al., 2008; Gassenmeier et al., 2016). We observe similar relation between velocity and time in our experiments, suggesting that similar physical processes may be active. This log-time behavior also indicates that velocity recovery occurs at multiple timescales.

Velocity recovery is not logarithmic in every fault setting following an earthquake. For example, in the Longmenshan area, the increase in velocity between the Wenchuan and Lushan earthquakes is linear in the first two to three years, unlike the laboratory observed log-time recovery (Figure 5.7). A comparison of percent velocity recovery observed after the Parkfield earthquake to laboratory data for the first one to two years show that the velocity recovers more steadily after the Parkfield earthquake as compared to laboratory data (Figure 5.8). As shown in Figure 5.8, the laboratory observed recovery in velocity trend is rather closer to the Omori decay, which occurs faster rate than the seismic velocity recovery (Brenguier et al., 2008). Implications

of such comparison, however, are unknown and requires further comparison with continuous field data.

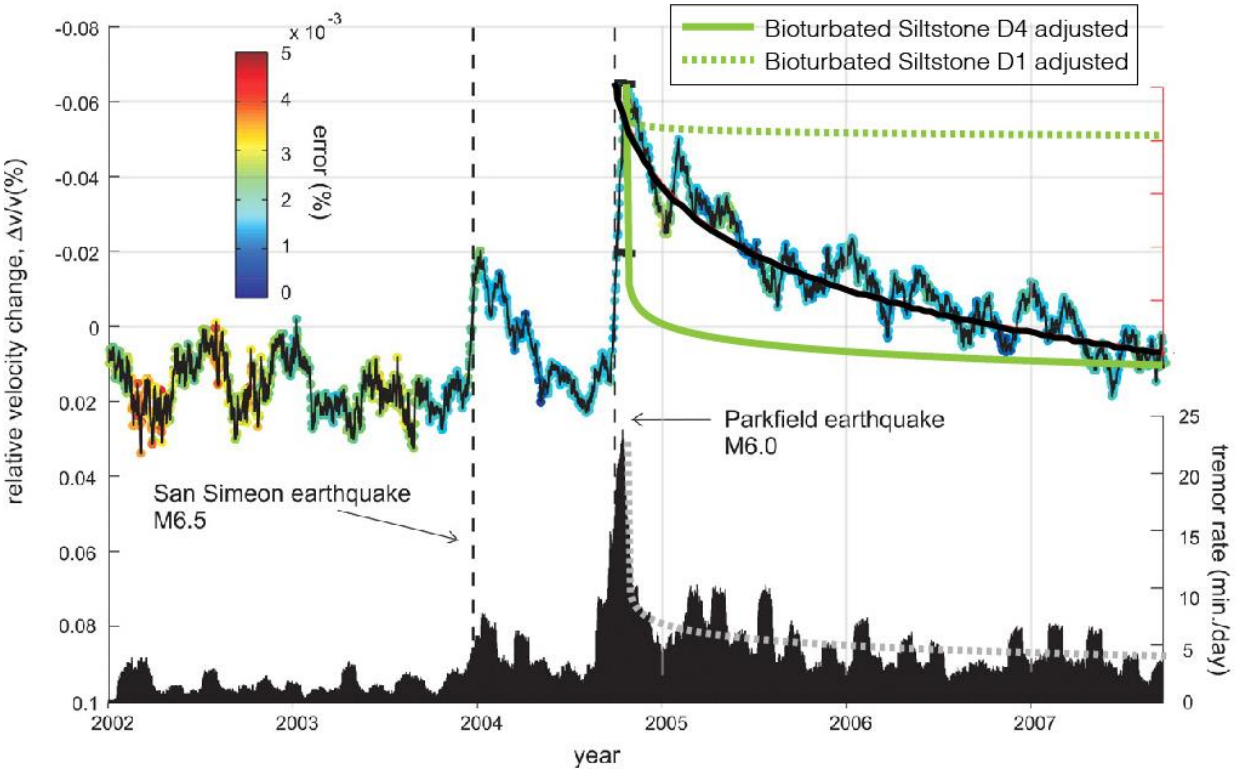

Figure 5.8. Tremor rate activity, seismic velocity, and GPS displacement near Parkfield, all shown in black. Extrapolated velocity history is overlaid on top of the ambient seismic noise field data.

5.4.2 Discrepancy between damage creation and healing trends

We cross plot porosity and velocity to observe the rate of change in velocity with porosity in Figure 5.9. The healing process can be indicated by a line joining the creep stages of the experiment in a porosity-velocity plot (shown by filled circles in Figure 5.9). It is also indicated by an upwards arrow in Figure 5.9. The black line joining initial data point of the experiments from D0-D4 is the trend of damage creation by SHPB. In this plot, we observe that (1) Slope of porosity velocity lines during the healing process decreases from D0 to D4 (colored arrows in Figure 5.9a get steeper from right to left). Or in other words, there is more velocity

change in an intact rock than a damaged rock for the same change in porosity. (2) $\frac{\Delta V}{\Delta \emptyset}$ during damage creation by SHPB (dotted black line in Figure 5.9) is lower than $\frac{\Delta V}{\Delta \emptyset}$ during healing. We discuss the implications of these observations.

The ultrasonic wave velocity is affected by stiffness and density of the rock. The density is assumed constant during the experiments, so the stiffness primarily affects the velocity of the rocks. Rock stiffness or bulk modulus can be described as

$$\frac{1}{\mathrm{K}} = \frac{1}{\mathrm{K_{min}}} + \frac{\emptyset}{\widetilde{\mathrm{K}}_{\emptyset}} \tag{5.2}$$

$$\widetilde{\mathrm{K}}_{\emptyset} = \mathrm{K}_{\emptyset} + \frac{\mathrm{K_{min}K_{fluid}}}{\mathrm{K_{min}} - \mathrm{K_{fluid}}} \tag{5.3}$$

Where K is the bulk modulus of the rock, K_{min} is the mineral bulk modulus, $\widetilde{K}_{\emptyset}$ is the pore space stiffness, and $\emptyset$ is the porosity of the rock. Pore space stiffness $\widetilde{K}_{\emptyset}$ is a function of pore space stiffness of the dry rock $K_{\emptyset}$, K_{min}, and the bulk modulus of the pore fluid, K_{fluid} (Mavko et al., 2020). So, velocity is a function of K, which in turn is a function of K_{min}, $K_{\emptyset}$, K_{fluid} and $\emptyset$. During the damage and healing processes, K_{min} and K_{fluid} stay constant because there is no change in mineral and fluid type in the rock. Therefore, K is a function of $K_{\emptyset}$ and $\emptyset$. K increases with increase in $K_{\emptyset}$ and/or decrease in $\emptyset$.

The pore space stiffness, $K_{\emptyset}$, here relates to the stiffness of the fracture pore volume because we consider that the pore volume change is happening primarily due to change in fracture volume. Thus, what governs the pore space stiffness is the stiffness of the asperity contacts between the mated rough fracture faces. We only discuss the bulk modulus here, but

shear modulus of the rock also influences the rock velocity. However, the discussion below is believed to apply also to the shear modulus.

We observe that in bioturbated siltstone there is:

(1) Higher $\frac{\Delta V}{\Delta \emptyset}$ in intact samples than the damaged specimens during healing: Higher $\frac{\Delta V}{\Delta \emptyset}$ in an intact sample indicates that the contact stiffening, caused by increase in asperity contact surface area, is faster. This also suggests that contact stiffening is dominant over porosity reduction in an intact rock during healing.

(2) Higher $\frac{\Delta V}{\Delta \emptyset}$ during healing than during damage creation: Higher $\frac{\Delta V}{\Delta \emptyset}$ during healing indicates increase in pore space stiffness of the rock, or the increase in asperity contact stiffness, possibly due to increase in contact surface area. The larger $\frac{\Delta V}{\Delta \emptyset}$ slope of the healing trends also suggests that such contact stiffening is a dominating mechanism over pore volume compaction (i.e., reduction in $\emptyset$) during healing. Conversely, damage creation trend shows smaller $\frac{\Delta V}{\Delta \emptyset}$ slope because pore volume creation during damage creation is a more dominant mechanism over contact stiffness change.

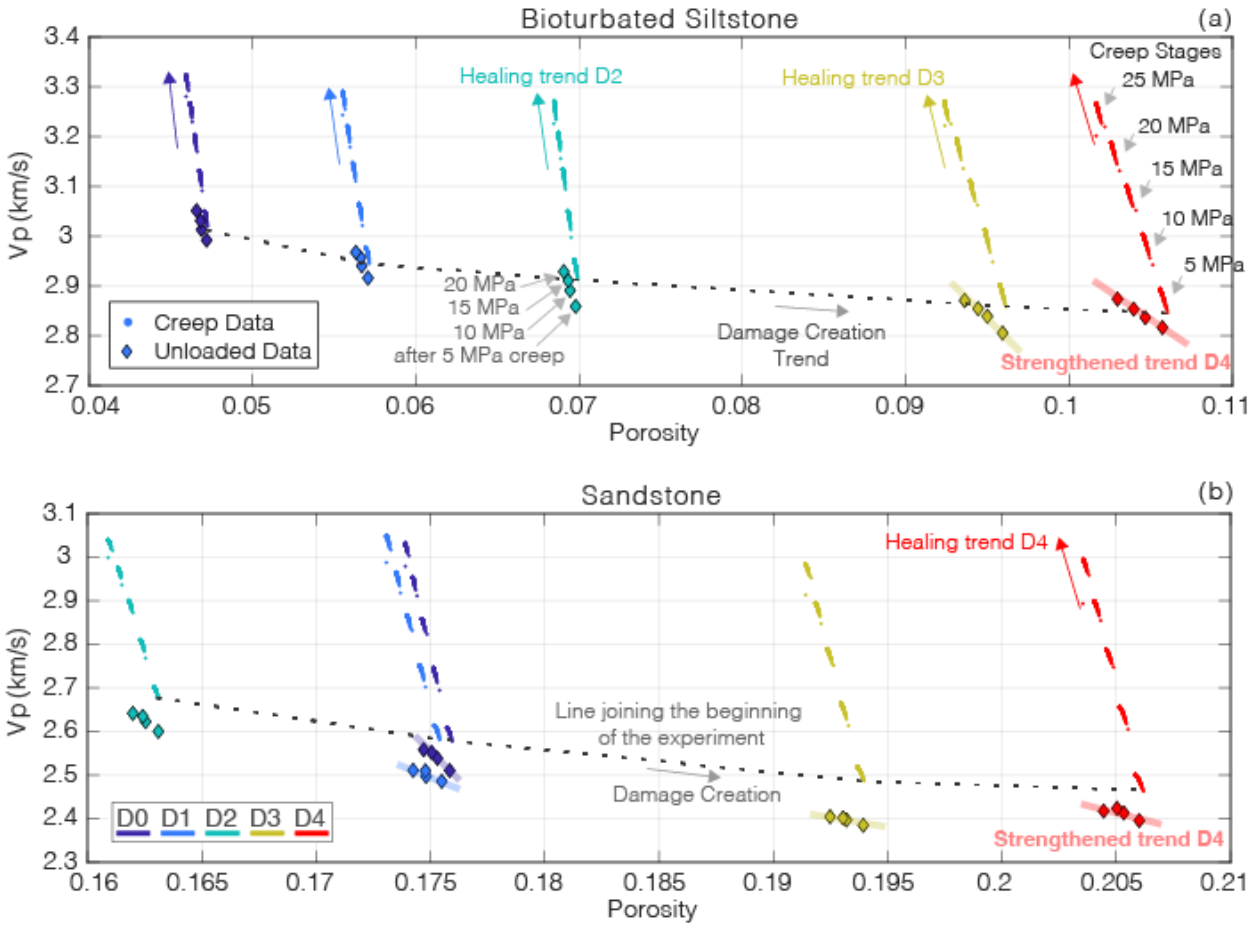

Figure 5.9. Cross-plot of porosity vs velocity for (a) bioturbated siltstone and (b) siltstone. The filled circles indicate the creep stage of the deformation, whereas the diamonds are the unloaded points. The upward arrows indicate the trend of creep deformation and the thick transparent lines joining unloaded points. The black dotted line is the trend of damage creation, defined by joining the initial state of all the samples.

5.4.3 Creep induced strengthening

Creep induced porosity decrease leads to velocity increase or increase in elastic moduli of the rock (Figure 5.9). This creep induced strengthening could be observed in the diamond shaped data points in Figure 5.9, which are data points collected after each unloading. The diamond markers for Bioturbated siltstone D2 specimen are labeled to clarify the differential stress magnitude of the hold stage before unloading. We observe that velocity increases considerably after each creep stage, suggesting creep induced strengthening. On comparing the unloaded data

points for various degrees of damage, we observe that there is more creep induced strengthening in a damaged rock, leading to more changes in velocity and porosity in the damaged specimen.

The ‘strengthened’ state after time-dependent deformation is shown by thick semi-transparent lines in Figure 5.9. Slope of the ‘strengthened’ trend is intermediate to the slope of damage creation and healing, indicating that the 3-hour healing process was not complete enough to bring the rock back to its initial condition (i.e., the damage creation trend). There could also be other healing mechanisms apart from fracture volume compaction and creep induced strengthening that these experiments are unable to capture which would allow for additional healing. We discuss these mechanisms in the next section.

5.4.4 Factors affecting comparison

Lower experimental velocity recovery by healing (~0.5-2%) compared to field observations in the Chelungpu fault system (2-7%) (by Chen et al. (2015)) can be due to several factors that the experimental setting does not simulate. The experiments are conducted at room temperature and dry conditions where the primary mechanism is mechanical compaction and increase in pore space stiffness. In contrast, the postseismic and interseismic healing that take place in a natural damage zone involve a complex interplay between mechanical, hydrological, and chemical processes.

Hydro-chemical processes can heal and seal fractures. For example, since water is chemically active, it allows dissolution of minerals followed by precipitation in another region. Beeler and Hickman (2004) has shown that such dissolution-precipitation promotes time-dependent creep and leads to closure of micro-cracks. Stress also causes local scale differences in solubility of the mineral driving such local dissolution and precipitation, a process known as pressure solution, which can progressively seal fractures. Elevated temperatures below the earth

surface also play an important role in enhancing dissolution-precipitation. Experimental studies of fracture behavior under high temperature conditions shows that in the presence of fluids, hydrothermal conditions accelerate crack closure by increasing rate of dissolution and precipitation of minerals (Aharonov et al., 1998; Tenthorey et al., 1998). For instance, permeability of Westerly granite at 300-500° C is significantly lower than in experiments conducted at room temperature (Moore et al., 1994) owing to the increasing pore closure rate by dissolution-precipitation at high temperatures.

Other studies have indicated that fluids like water also enhance diffusion processes, which can also lead to time-dependent healing and sealing of microcracks (Brantley, 1992; Brantley et al., 1990; Hickman and Evans, 1987; Smith and Evans, 1984; Tenthorey and Gerald, 2006). Such diffusion processes are primarily driven by mass transfer from high surface energy sites to low surface energy sites (Gratier et al., 2014; Kingery, 1976), sometimes called self-healing (Aben et al., 2017).

In the presence of pore fluids, reduction in pore pressure can also lead to crack closure in rocks. Poroelasticity driven pore pressure increase during loading can subsequently dissipate into the surrounding with time during the creep stage. This time-dependent pore pressure dissipation increases effective stress, resulting in time-dependent closure of cracks and pores.

The discrepancy between damage creation and healing trends (Section 5.4.2) and the mismatch between strengthened and damage creation trends (Section 5.4.3) may suggest that the above-mentioned mechanisms of time-dependent deformation reduce porosity in natural settings. Adding contributions of these creep deformation mechanisms may reduce porosity substantially, thereby decreasing $\frac{\Delta V}{\Delta \emptyset}$ of the healing trend to match the damage creation trend.

Apart from creep mechanisms, the discrepancy can be due to differences in the nature of damage. The size, shape, and orientation of cracks in an artificial damage zone is different from natural damage zones although we simulated identical strain rates achieved during natural earthquakes. For instance, it is well-known that rock strengths and stiffness decreases with sample size due to larger-scale defects being present in larger rock masses. During artificial damage creation, lack of radial confinement in the SHPB samples allowed formation of longitudinal cracks in the rocks, however, in a natural setting, high lateral confinement will hinder such crack formation. Furthermore, the velocity recovery observed in natural damage zones by seismic and geodetic studies are also spatially averaged over damage zones of various damage sizes and intensities. Synthetic damage rocks may not replicate such damage heterogeneity.

5.5 Conclusion

This study characterizes the time-dependent velocity recovery of damaged rocks in the laboratory, compares the lab results with field observations of seismic velocity and discuss mechanisms for time-dependent velocity increase in intact and damaged rocks. We observe that fractured rocks show time-dependent velocity recovery at constant stress because of temporal porosity reduction and increase in contact stiffness of the fracture surfaces. These mechanisms are more active in a damaged specimen; therefore, we observe an increase in velocity recovery with increasing damage. We also found that velocity increases linearly with logarithm of time. This logarithmic relationship is used to extrapolate the velocity data to larger time scales and compare with field scale observations.

Velocity recovery in the Chelungpu fault system observed from seismic studies have observed a 2-7% increase in velocity over a period of 7 years, substantially higher than laboratory extrapolated velocity magnitudes (0.5-2%). Although the laboratory observed velocity magnitude is in the same order as postseismic velocity recovery after 6-7 years, not all studies show a logarithmic increase in velocity. The factors affecting the magnitude of recovery may include differences in pressure, temperature, lithology, and fluid conditions as well as variability in fracture size, distribution, and extent of the damage zone. These factors may promote chemical, hydrological and thermal processes that may be active in a natural setting. It is also difficult to compare natural and field scale to the lab scale because the spatially averaged nature of the field data hinders proper understanding of healing mechanisms in a natural damage zone. Nonetheless, this study provided insights on the dominant mechanisms behind velocity recovery. A comparison of healing and damage creation processes suggests that creep induced asperity stiffening is a more active process than fracture volume compaction during the hold stages of the experiment.

Acknowledgement

This study was supported by National Science Foundation Award No. EAR1727661 and EAR2045259.

References

Aben, F. M., Doan, M.-L., Gratier, J.-P., and Renard, F. (2017). Experimental postseismic recovery of fractured rocks assisted by calcite sealing. *Geophysical Research Letters*, *44*(14), 7228–7238.

Aharonov, E., Tenthorey, E., and Scholz, C. H. (1998). Precipitation sealing and diagenesis: 2.

Theoretical analysis. *Journal of Geophysical Research: Solid Earth*, *103*(B10), 23969–23981.

Beeler, N. M., and Hickman, S. H. (2004). Stress-induced, time-dependent fracture closure at hydrothermal conditions. *Journal of Geophysical Research: Solid Earth*, *109*(B2).

Brantley, S. L. (1992). The effect of fluid chemistry on quartz microcrack lifetimes. *Earth and Planetary Science Letters*, *113*(1–2), 145–156.

Brantley, S. L., Evans, B., Hickman, S. H., and Crerar, D. A. (1990). Healing of microcracks in quartz: Implications for fluid flow. *Geology*, *18*(2), 136–139.

Brenguier, F., Campillo, M., Hadziioannou, C., Shapiro, N. M., Nadeau, R. M., and Larose, É. (2008). Postseismic relaxation along the San Andreas fault at Parkfield from continuous seismological observations. *Science*, *321*(5895), 1478–1481.

Chen, K. H., Furumura, T., and Rubinstein, J. (2015). Near-surface versus fault zone damage following the 1999 Chi-Chi earthquake: Observation and simulation of repeating earthquakes. *Journal of Geophysical Research: Solid Earth*, *120*(4), 2426–2445.

Dieterich, J. H. (1972). Time-dependent friction in rocks. *Journal of Geophysical Research*, *77*(20), 3690–3697.

Dieterich, J. H. (1978). Time-dependent friction and the mechanics of stick-slip. In *Rock friction and earthquake prediction* (pp. 790–806). Springer.

Doan, M.-L., and Gary, G. (2009). Rock pulverization at high strain rate near the San Andreas fault. *Nature Geoscience*, *2*(10), 709–712.

Fjær, E. (2009). Static and dynamic moduli of a weak sandstone. *Geophysics*, *74*(2), WA103--

WA112.

Froment, B., McGuire, J. J., van der Hilst, R. D., Gouédard, P., Roland, E. C., Zhang, H., and Collins, J. A. (2014). Imaging along-strike variations in mechanical properties of the Gofar transform fault, East Pacific Rise. *Journal of Geophysical Research: Solid Earth*, *119*(9), 7175–7194.

Gassenmeier, M., Sens-Schönfelder, C., Eulenfeld, T., Bartsch, M., Victor, P., Tilmann, F., and Korn, M. (2016). Field observations of seismic velocity changes caused by shaking-induced damage and healing due to mesoscopic nonlinearity. *Geophysical Journal International*, *204*(3), 1490–1502.

Gratier, J. P., Renard, F., and Vial, B. (2014). Postseismic pressure solution creep: Evidence and time-dependent change from dynamic indenting experiments. *Journal of Geophysical Research: Solid Earth*, *119*(4), 2764–2779.

Hickman, S. H., and Evans, B. (1987). Influence of geometry upon crack healing rate in calcite. *Physics and Chemistry of Minerals*, *15*(1), 91–102.

Hobiger, M., Wegler, U., Shiomi, K., and Nakahara, H. (2014). Single-station cross-correlation analysis of ambient seismic noise: application to stations in the surroundings of the 2008 Iwate-Miyagi Nairiku earthquake. *Geophysical Journal International*, *198*(1), 90–109.

Illien, L., Sens-Schönfelder, C., Andermann, C., Marc, O., Cook, K. L., Adhikari, L. B., and Hovius, N. (2022). Seismic velocity recovery in the subsurface: transient damage and groundwater drainage following the 2015 Gorkha earthquake, Nepal. *Journal of Geophysical Research: Solid Earth*, *127*(2), e2021JB023402.

Jizba, D., and Nur, A. (1990). Static and dynamic moduli of tight gas sandstones and their

relation to formation properties. In *SPWLA 31st annual logging symposium*.

Karabulut, H., and Bouchon, M. (2007). Spatial variability and non-linearity of strong ground motion near a fault. *Geophysical Journal International*, *170*(1), 262–274.

Kingery, W. D. (1976). Introduction to Ceramics, Chpt. III subchapter 8.8. *Glass-Ceramic Materials*, 368–374.

Kitagawa, Y., Fujimori, K., and Koizumi, N. (2007). Temporal change in permeability of the Nojima fault zone by repeated water injection experiments. *Tectonophysics*, *443*(3–4), 183–192.

Li, Y.-G., Vidale, J. E., Aki, K., Xu, F., and Burdette, T. (1998). Evidence of shallow fault zone strengthening after the 1992 M 7.5 Landers, California, earthquake. *Science*, *279*(5348), 217–219.

Li, Y.-G., Vidale, J. E., Day, S. M., Oglesby, D. D., and Cochran, E. (2003). Postseismic Fault Healing on the Rupture Zone of the 1999 M 7.1 Hector Mine, California, Earthquake. *Bulletin of the Seismological Society of America*, *93*(2), 854–869. https://doi.org/10.1785/0120020131

Li, Y.-G., Chen, P., Cochran, E. S., Vidale, J. E., and Burdette, T. (2006). Seismic Evidence for Rock Damage and Healing on the San Andreas Fault Associated with the 2004 M 6.0 Parkfield Earthquake. *Bulletin of the Seismological Society of America*, *96*(4B), S349–S363. https://doi.org/10.1785/0120050803

Liu, Z., Huang, J., He, P., and Qi, J. (2018). Ambient noise monitoring of seismic velocity around the Longmenshan fault zone from 10 years of continuous observation. *Journal of Geophysical Research: Solid Earth*, *123*(10), 8979–8994.

Manga, M., Beresnev, I., Brodsky, E. E., Elkhoury, J. E., Elsworth, D., Ingebritsen, S. E., et al. (2012). Changes in permeability caused by transient stresses: Field observations, experiments, and mechanisms. *Reviews of Geophysics*, *50*(2).

Matsuki, K., and Takeuchi, K. (1993). Three-dimensional in-situ stress determination by anelastic strain recovery of a rock core. In *The 34th US Symposium on Rock Mechanics (USRMS)*.

Mavko, G., Mukerji, T., and Dvorkin, J. (2020). *The rock physics handbook*. Cambridge university press.

Meyer, G. G., Brantut, N., Mitchell, T. M., Meredith, P. G., and Plümper, O. (2021). Time dependent mechanical crack closure as a potential rapid source of post-seismic wave speed recovery: Insights from experiments in Carrara Marble. *Journal of Geophysical Research: Solid Earth*, *126*(4), e2020JB021301.

Moore, D. E., Lockner, D. A., and Byerlee, J. D. (1994). Reduction of permeability in granite at elevated temperatures. *Science*, *265*(5178), 1558–1561.

Olivier, G., Brenguier, F., Campillo, M., Roux, P., Shapiro, N. M., and Lynch, R. (2015). Investigation of coseismic and postseismic processes using in situ measurements of seismic velocity variations in an underground mine. *Geophysical Research Letters*, *42*(21), 9261–9269.

Pei, S., Niu, F., Ben-Zion, Y., Sun, Q., Liu, Y., Xue, X., et al. (2019). Seismic velocity reduction and accelerated recovery due to earthquakes on the Longmenshan fault. *Nature Geoscience*, *12*(5), 387–392.

Peng, Z., and Ben-Zion, Y. (2006). Temporal changes of shallow seismic velocity around the

Karadere-Düzce branch of the north Anatolian fault and strong ground motion. *Pure and Applied Geophysics*, *163*(2), 567–600.

Rubinstein, J. L., and Beroza, G. C. (2004). Evidence for widespread nonlinear strong ground motion in the Mw 6.9 Loma Prieta earthquake. *Bulletin of the Seismological Society of America*, *94*(5), 1595–1608.

Rubinstein, J. L., and Beroza, G. C. (2005). Depth constraints on nonlinear strong ground motion from the 2004 Parkfield earthquake. *Geophysical Research Letters*, *32*(14).

Sawazaki, K., Sato, H., Nakahara, H., and Nishimura, T. (2009). Time-lapse changes of seismic velocity in the shallow ground caused by strong ground motion shock of the 2000 Western-Tottori earthquake, Japan, as revealed from coda deconvolution analysis. *Bulletin of the Seismological Society of America*, *99*(1), 352–366.

Schaff, D. P., and Beroza, G. C. (2004). Coseismic and postseismic velocity changes measured by repeating earthquakes. *Journal of Geophysical Research: Solid Earth*, *109*(B10).

Shokouhi, P., Rivière, J., Guyer, R. A., and Johnson, P. A. (2017). Slow dynamics of consolidated granular systems: Multi-scale relaxation. *Applied Physics Letters*, *111*(25), 251604.

Smith, D. L., and Evans, B. (1984). Diffusional crack healing in quartz. *Journal of Geophysical Research: Solid Earth*, *89*(B6), 4125–4135.

Taira, T., Brenguier, F., and Kong, Q. (2015). Ambient noise-based monitoring of seismic velocity changes associated with the 2014 Mw 6.0 South Napa earthquake. *Geophysical Research Letters*, *42*(17), 6997–7004.

TenCate, J. A. (2011). Slow dynamics of earth materials: An experimental overview. *Pure and Applied Geophysics*, *168*(12), 2211–2219.

Tenthorey, E., and Gerald, J. D. F. (2006). Feedbacks between deformation, hydrothermal reaction and permeability evolution in the crust: Experimental insights. *Earth and Planetary Science Letters*, *247*(1–2), 117–129.

Tenthorey, E., Scholz, C. H., Aharonov, E., and Léger, A. (1998). Precipitation sealing and diagenesis: 1. Experimental results. *Journal of Geophysical Research: Solid Earth*, *103*(B10), 23951–23967.

Teufel, L. W. (1983). Determination of in-situ stress from anelastic strain recovery measurements of oriented core. In *SPE/DOE Low Permeability Gas Reservoirs Symposium*.

Tremblay, N., Larose, É., and Rossetto, V. (2010). Probing slow dynamics of consolidated granular multicomposite materials by diffuse acoustic wave spectroscopy. *The Journal of the Acoustical Society of America*, *127*(3), 1239–1243.

Utsu, T., Ogata, Y., and others. (1995). The centenary of the Omori formula for a decay law of aftershock activity. *Journal of Physics of the Earth*, *43*(1), 1–33.

Vidale, J. E., and Li, Y.-G. (2003). Damage to the shallow Landers fault from the nearby Hector Mine earthquake. *Nature*, *421*(6922), 524–526.

Walsh, J. B., and Brace, W. F. (1966). Elasticity of rock: a review of some recent theoretical studies. *Rock Mechanics and Engineering Geology*, *4*(4), 283–297.

Wang, C. Y., and Manga, M. (2015). New streams and springs after the 2014 Mw6. 0 South Napa earthquake. Nat Commun 6: 7597.

Wu, C., Peng, Z., and Ben-Zion, Y. (2009). Non-linearity and temporal changes of fault zone site response associated with strong ground motion. *Geophysical Journal International*, *176*(1), 265–278.

Wu, C., Peng, Z., and Ben-Zion, Y. (2010). Refined thresholds for non-linear ground motion and temporal changes of site response associated with medium-size earthquakes. *Geophysical Journal International*, *182*(3), 1567–1576.

Xue, L., Li, H.-B., Brodsky, E. E., Xu, Z.-Q., Kano, Y., Wang, H., et al. (2013). Continuous permeability measurements record healing inside the Wenchuan earthquake fault zone. *Science*, *340*(6140), 1555–1559.

5.6 Appendix

5.6.1 Static vs Dynamic elastic properties

Dynamic and static moduli of rocks are derived from stress-strain relations and wave-velocity measurements, respectively. For a homogeneous material, the static and dynamic modulus are identical but for a heterogeneous rock, the presence of pores leads to large differences in static and dynamic modulus of rocks, especially at low stress magnitudes. Larger pore volume has been attributed to larger differences in static and dynamic modulus of rocks. For the same reason, presence of cracks leads to large differences in static and dynamic modulus of rocks (Jizba and Nur, 1990; Walsh and Brace, 1966). Frequency and strain amplitude vary significantly due to the presence of cracks; therefore, cracks control the discrepancy between static and dynamic modulus.

Our experimental results show that static and dynamic modulus is dependent on the degree of damage, stress magnitude and the pre-consolidation stress of the material. We show

results for the stress steps during which the first-time axial differential stress was applied and during reloading/ unloading of the sample.

For the first time loading, we observe that most data points fall above the 1-1 ratio line. The damaged samples show lower static modulus because static modulus is influenced by the frictional sliding along cracks at high strain magnitudes (Fjær, 2009); whereas the dynamic modulus is not affected because of the low strain amplitude involved in dynamic measurements. The intact samples have similar dynamic modulus but higher static modulus than damaged rocks because there is less frictional sliding.

We observe that that during reloading and unloading, the ratio of static to dynamic measurements is close to 1. When stress reversal occurs during reloading and unloading of the sample, static friction prevents sliding at the frictional interfaces (Fjær, 2009); therefore, static and dynamic measurements are almost equal.

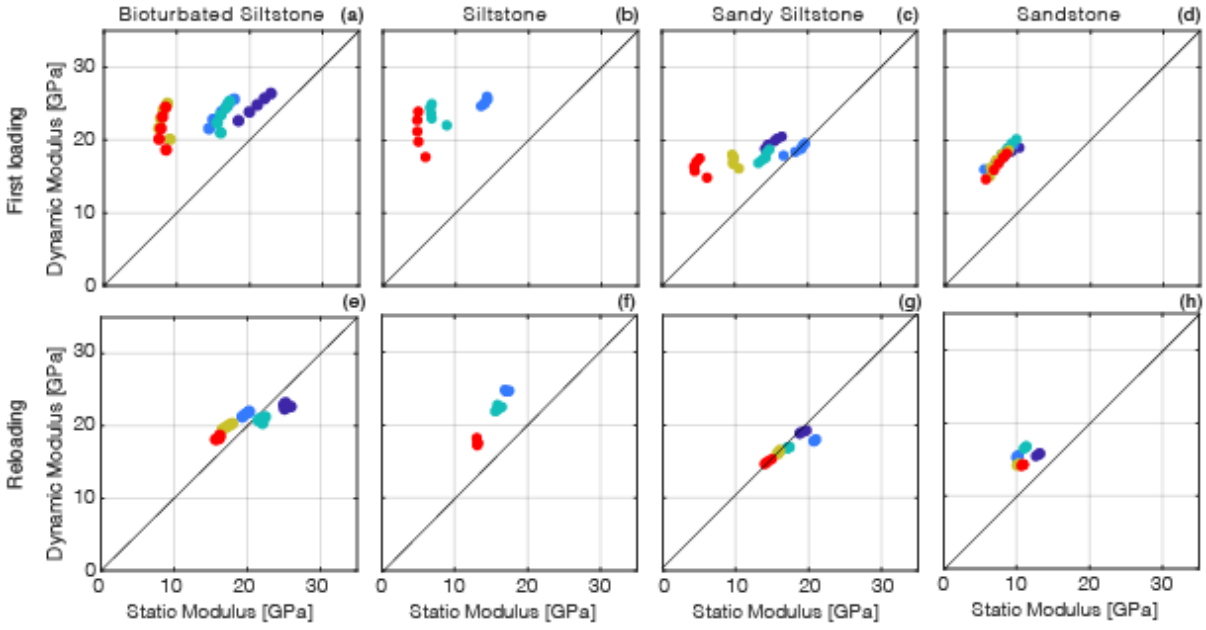

Figure 5.S1. Static vs dynamic modulus during first loading for (a) bioturbated siltstone, (b) siltstone, (c) sandy siltstone and (d) sandstone. Static vs dynamic loading during reloading for (a) bioturbated siltstone, (b) siltstone, (c) sandy siltstone and (d) sandstone.